January 2018

A Global Investigation Of Cloud-Radiative Properties Through An Integrative Analysis Of Observations And Model Simulations

Erica Kay Dolinar

A GLOBAL INVESTIGATION OF CLOUD-RADIATIVE PROPERTIES THROUGH AN INTEGRATIVE ANALYSIS OF OBSEVRATIONS AND MODEL SIMULATIONS

by

Erica Kay Dolinar
Bachelor of Science, Millersville University, 2011
Master of Science, University of North Dakota, 2014

A Dissertation

Submitted to the Graduate Faculty

of the

University of North Dakota

in partial fulfillment of the requirements

for the degree of

Doctor of Philosophy

Grand Forks, North Dakota

August
2018

This dissertation, submitted by Erica Dolinar in partial fulfillment of the requirements for the Doctor of Philosophy from the University of North Dakota, has been read by the Faculty Advisory Committee under whom the work has been done and is hereby approved.

Aaron Kennedy

Baike Xi

Jianglong Zhang

Jonathan Jiang

Norman Loeb

Jeffrey VanLooy

This dissertation is being submitted by the appointed advisory committee as having met all of the requirements of the School of Graduate Studies at the University of North Dakota and is hereby approved.

Wayne Swisher
Dean of the School of Graduate Studies

Date

PERMISSION

Title A Global Investigation of Cloud-Radiative Properties through an Integrative Analysis of Observations and Model Simulations

Department Atmospheric Sciences

Degree Doctor of Philosophy

In presenting this dissertation in partial fulfillment of the requirements for a graduate degree from the University of North Dakota, I agree that the library of this University shall make it freely available for inspection. I further agree that permission for extensive copying for scholarly purposes may be granted by the professor who supervised my dissertation work or, in her absence, by the Chairperson of the department or the dean of the School of Graduate Studies. It is understood that any copying or publication or other use of this dissertation or part thereof for financial gain shall not be allowed without my written permission. It is also understood that due recognition shall be given to me and to the University of North Dakota in any scholarly use which may be made of any material in my dissertation.

Erica Dolinar
24 July 2018

TABLE OF CONTENTS

LIST OF FIGURES

Figure Page

LIST OF TABLES

Table Page

ACKNOWLEDGEMENTS

First and foremost, I must acknowledge and thank my advisors, Drs. Xiquan Dong and Baike Xi, for hiring me as a Graduate Research Assistant in 2012. Over the last six years, your advisement has supported me through Master's and Ph.D. level degrees, and I feel well-prepared for the next chapter of my career as an atmospheric scientist. I am so thankful for the opportunities you have given me, whether I was traveling to conferences and workshops or internships. Providing these experiences is a reflection the commitment you have for your students and, as a result, has made our research group feel familial.

Secondly, I would like to thank Drs. Jonathan Jiang and Hui Su at the Jet Propulsion Laboratory (JPL) in Pasadena, CA. On two separate occasions (seven months in total), Jonathan hosted me as an intern at JPL. Jonathan also added useful feedback which ultimately lead to my selection for the NASA Earth and Science Fellowship Program, a $90,000 award to support my Ph.D. (I am also very thankful for the NASA ESSFP and acknowledge its support). Since both Jonathan and Hui have co-authored several of my papers, I must also acknowledge their support in guiding me through graduate school and preparing me for a career in atmospheric science.

Third, Dr Norman Loeb from the NASA Langley Research Center in Hampton, VA. As a summer internship host, co-author on two papers, and committee member, your efforts are certainly not overlooked. I feel compelled to also acknowledge James Campbell at the U.S. Naval Research Laboratory (NRL). While this collaboration still in its infancy, I appreciate his input related to my study on ice cloud properties and their radiative effects.

I look forward to continuing this collaboration as I begin my post-Doc appointment at NRL this Fall.

Last, but certainly not least, my friends and family. The unrelenting support from my friends, fellow graduate students, and faculty at the University of North Dakota do not go unnoticed. You made the day-to-day struggles bearable and the good times that much better. The encouragement from my family continually provided the confidence I needed to make it through graduate school, and I am happy to make them so proud. Now you may call me “Dr. Sissy”.

ABSTRACT

The cloud and radiative properties simulated in an assortment of global climate models (GCMs) and reanalyses are examined to identify and assess systematic biases based upon comparisons with multiple satellites observations and retrievals. The global mean total column cloud fraction (CF) simulated by the 33-member multimodel mean is 7% and 17% lower than the results from passive (Moderate Resolution Infrared Spectroradiometer, MODIS) and active (CloudSat and Cloud-Aerosol Lidar and Infrared Pathfinder Satellite Observation, CALIPSO) satellite remote sensing platforms. The simulated cloud water path (CWP), which is used as a proxy for optical depth, on global average, has a negative bias of ~17 g m^{-2}. Despite these errors in simulated cloud properties, the simulated top-of-atmosphere (TOA) radiation budgets match relatively well with Clouds and the Earth Radiant Energy System (CERES) measurements. The biases in multimodel mean global TOA reflected shortwave (SW) and outgoing longwave (LW) fluxes and cloud radiative effects (CREs) are less than 2.5 W m^{-2}. Nevertheless, when assessing models individually, some physically inconsistent results are evident. For example, in the ACCESS1.0 model, the simulated TOA SW and LW fluxes are within 2 W m^{-2} of the observed global means, however, the global mean CF and CWP are underpredicted by ~10% and ~25 g m^{-2}, respectively. These unphysical model biases suggest tuning of the modeled radiation budgets.

Two dynamically-driven regimes, based on the atmospheric vertical motion at 500 hPa (ω500), are identified to provide a more quantitative measure of error in the radiation

fields determined separately by biases in CF and CWP. These error types include the regime-averaged biases, biases in the sensitivity of TOA CREs to CF/CWP, and their co-variations. Overall, the biases in simulated CF and CWP are larger in the descent regime ($\omega500 > 25$ hPa day^{-1}) than in the ascent regime ($\omega500 < -25$ hPa day^{-1}), but are better correlated with observations. According to CERES observations, the sensitivity of LW CRE to CF is stronger in the ascent regime than in the decent regime (0.82 vs. 0.23 W m^{-2} %$^{-1}$) and the multimodel mean overestimates this value by ~40%. The difference in sensitivity of SW CRE to CF between the two regimes is less drastic (–1.34 vs. –1.12 W m^{-2} %$^{-1}$). TOA CREs rely independently on CWP in regions of large scale ascent and decent, as their sensitivities are similar between these two regimes (e.g., SW CRE/CWP = –0.28 W g^{-1} for both regimes). In general, the total TOA CRE errors are heavily weighted by their biases in simulated sensitivity and biases in the simulated CF.

A new observationally-constrained, data product is generated that can be used as a process-oriented diagnostic tool to further identify errors in simulated cloud and radiation fields. Based on the CloudSat and CALIPSO Ice Cloud Property Product (2C-ICE), and through one-dimensional radiative transfer modeling, a global database of radiative heating rate profiles is produced for non-precipitating single-layered ice clouds. Non-precipitating single-layered ice clouds have a global occurrence frequency of ~18% with considerable frequency in the tropical upper troposphere (13–16 km). A variety of ice cloud types exist in the sample of single-layered ice clouds developed here, which is determined by the distribution on cloud-top temperatures (CTT). For example, a peak in the distribution near

190 K (260 K) suggests the existence of cirrus (glaciated ice) clouds. The ice cloud microphysical properties responsible for having the largest impact on radiation (e.g., ice water content [IWC] and effective radius [R_e]) are largest in the tropics and mid-latitudes according to 2C-ICE. Accordingly, this is where the strongest TOA SW absorption, and subsequently, the strongest upper tropospheric net radiative heating (> 1.5 K day^{-1}) occurs. This newly generated product will provide the data for which new ice cloud parameterizations can be developed in global models.

CHAPTER I

INTRODUCTION

The radiation budget is a point of interest when assessing changes in the Earth climate system (i.e., *Wielicki et al.* 1996; *Loeb et al.* 2007; *L'Ecuyer et al.* 2015; *Kato et al.* 2015). Clouds are one of the primary modulators of the Earth radiation budget, as they can act to warm or cool the atmosphere/surface based upon their horizontal and vertical extent, microphysical and optical properties, surface properties, and prevalence during the day and night (*Stephens and Webster* 1981; *Fu and Liou* 1993; *Campbell et al.* 2016). For example, Fig. 1 depicts the basic interaction of radiation with two types of clouds. High-level cirrus clouds are rather transparent (i.e., optically thin) to shortwave (SW, wavelength $\lambda < 5$ μm) radiation and thus have little-to-no impact on the amount of SW radiation that is transmitted to the Earth's surface. At the same time, since high-level cirrus have relatively cold cloud-top temperatures (CTT < ~220 K; *Dong et al.* 2008b), their longwave (LW $\lambda =$ 5–100 μm) emission is small. As a result, high-level cirrus-type clouds are commonly regarded as atmospheric warmers (relative to when clouds are not present). In contrast, low-level clouds, such as those found in the marine boundary layer (MBL), have a strong albedo effect, meaning they are efficient at reflecting SW radiation, thereby reducing the amount of SW radiation that reaches the surface. Low-level clouds also have warmer cloud-tops (~280 K, *Dong et al.* 2014; *Xi et al.* 2014), similar to that of the underlying surface. As such, low-level clouds are notorious for having a strong cooling effect.

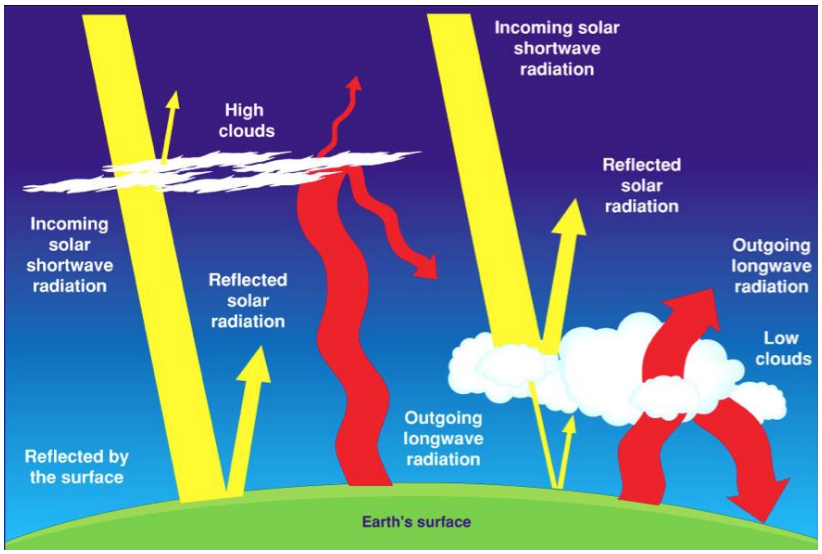

Figure 1: A simple diagram depicting the interaction of shortwave (SW, yellow arrows) and longwave (LW, red arrows) radiation with clouds in the atmosphere and at the surface.

With clouds being a primary modulator of the Earth radiation budget (*Ramanathan et al.* 1989; *Hartmann et al.* 1992; *Randall et al.* 2007), properly observing and modeling their properties on the global scale has become an extensive undertaking over the last several decades. Historically (late 1970s to early 2000s), global cloud datasets developed from satellite measurements were based primarily on passive sensors and imagers including the Geostationary Operational Environmental Satellite (GOES), the Advanced Very High Resolution Radiometer (AVHRR), the Moderate Resolution Infrared Spectroradiometer (MODIS), and the International Satellite Cloud Climatology Project (ISCCP; Rossow and Schiffer 1999). Passive sensors detect and provide retrieved cloud microphysical properties (effective Radius [R_e] and optical depth [τ]) based on measured radiances near the cloud-top, meaning the vertical distribution of clouds is not fully resolved (*Painemal and Zuidema* 2011). Furthermore, passive sensors are only sensitive to

clouds with an optical depth of greater than ~0.4 and have routinely exhibited error in detecting clouds during polar night (*Ackerman et al.* 2008).

Satellite estimates of the Earth radiation budget began in the mid-1980s with the launch of the Earth Radiation Budget Experiment (ERBE; *Barkstrom et al.* 1989) instrument on the National Oceanic and Atmospheric Administration (NOAA) 9 satellite. The derived measurements of top-of-atmosphere (TOA) broadband fluxes from three channels are commonly used for a variety of studies related to the exchange of energy between the Sun, Earth, and space. As a successor to ERBE, the Clouds and Earth Radiant Energy System (CERES; *Wielicki et al.* 1996) instrument was launched on the Tropical Rainfall Measurement Mission (TRMM) satellite in 1997 and was designed to extend the record of global estimates of TOA and surface radiation budgets. CERES channels cover the wavelengths from 0–5 μm (SW), 5–100 μm (LW), and 8–12 μm (window). Currently, there are four CERES instruments in space on the Terra, Aqua, Suomi National Polar-orbiting Partnership (NPP), and Joint Polar Satellite System (JPSS-1) satellites. Together with measured cloud properties from MODIS, the CERES datasets are one of the most reliable sources for estimating global TOA and surface radiation budgets, especially in a climate frame of reference (*Wielicki et al.* 1996).

As active remote sensing platforms, such as CloudSat and the Cloud-Aerosol Lidar and Infrared Pathfinder Satellite Observation (CALIPSO) began measuring the vertical structure of clouds from space in 2006, radiative transfer modeling of their radiative flux profiles became more prolific on the global scale (e.g., *L'Ecuyer et al.* 2008; *Su et al.* 2009).

The inclusion of Cloud Aerosol Lidar with Orthogonal Polarization (CALIOP) on board CALIPSO allowed for improved detection of optically-thin ice clouds ($\tau < 0.3$; *Sassen and Cho* 1992) which have a measurable impact on the radiation budget (*Chiriaco et al.* 2007; *Minnis et al.* 2008; *Kox et al.* 2014). In fact, cirrus clouds are now estimated to be the most common type of cloud found on Earth, with an estimated instantaneous global occurrence frequency of 40% (*Steubenrauch et al.* 2013), which has been upgraded from 20% based on passive estimates (*Rossow and Schiffer* 1999). CloudSat and CALISPO are members of the A-Train satellite constellation (*L'Ecuyer and Jiang 2010*) orbiting the Earth ~15 times a day on a sun-synchronous orbit at ~700 km above the surface. Kato et al. (2011) described the impacts that the CloudSat cloud profiling radar (CPR) and CALIOP data have on irradiance computations. For one year of instantaneous TOA fluxes, the computed fluxes based on CloudSat and CALIPSO cloud properties match better with CERES-measured fluxes, to within 0.5 and 2.6 W m^{-2} for SW and LW, respectively, compared with the fluxes estimated from MODIS-only cloud properties. Similarly, at the surface, their calculated global mean instantaneous downward SW and LW fluxes change by –8.6 and +3.4 W m^{-2}, respectively, due to larger cloud fractions and lower cloud-base heights compared with MODIS.

While the redistribution of radiation (i.e., energy) in the atmosphere, modified by the presence clouds, has important implications on large-scale circulation patterns, the hydrological cycle (*Larson and Hartmann* 2003; *Wild et al.* 2004), and their feedbacks (*Zelinka et al.* 2016; *Zhou et al.* 2017), understanding the role of clouds in this context, and

how it changes over time, is crucial for climate change analytics. Modeling studies indicate that in a changing climate, forced by any number of scenarios (e.g., double CO_2), the distribution of clouds will be modified. To what extent is still a topic for debate, as clouds are one of the primary sources of uncertainty in assessing future climate change (*IPCC AR5* 2013). This uncertainty is related to the vertical and horizontal distribution of clouds, cloud phase, and cloud optical properties - all of which can be tied back to their radiative effects. Ceppi et al. (2017) divulged a potential impact that a warming climate could have on the cloud-radiative feedbacks on Earth. In a warming climate, the amount of low clouds would decrease, generating a net radiative feedback of approximately +0.3 W m^{-2} K^{-1}. Since clouds, especially low clouds, generate a strong SW cooling effect (–91 W m^{-2}; *Dong et al.* 2006), this cooling effect would be reduced, thereby supporting the increase in global temperature (i.e., positive feedback).

But how reliable are climate models and the subsequent conclusions drawn from their results, given the fact that future climate cannot be verified, as in weather forecasting? The only opportunity for GCM evaluation arises for models that predict recent-past and current climate states, and satellites offer an invaluable data source for assessing the biases in these global models. Lauer and Hamilton (2012) have revealed that the model simulated cloud radiative effects (CREs) tend to outperform simulated cloud results, suggesting that models are not accurately depicting fundamental cloud processes. Rather, the models are being tuned to provide simulations that converge to observations.

The cloud vertical distribution and overlap are some of the major uncertainties in determining the heating/cooling profile by radiative and precipitable/evaporative processes (e.g., *Stephens and Webster* 1984; *Morcrette and Jakob* 2000; *Stephens et al.* 2002). The spread of climate warming predictions by a multimodel ensemble is, arguably, a result of an over simplification of cloud vertical distributions and their overlap assumptions (*Stephens et al.* 2002). Simulated cloud vertical distributions under the random overlap assumption shows better agreement with observations than those under other assumptions (e.g., maximum, minimum, and maximum-random). Yet still, the maximum-random overlap assumption is used by most GCMs (e.g., *Hogan and Illingworth* 2000; *Collins et al.* 2001).

Here, an independent evaluation of globally simulated clouds and their impact on the Earth radiation budget is performed using instruments on satellites flying in the A-Train (Chapter 3). More importantly, a systematic error analysis of CREs is conducted over atmospheric ascent and descent regions (as in *Wang and Su* 2013) over the tropical and extra-tropical oceans (±45 °N/S) that quantifies errors in simulated CREs based on biases in the simulated CF and CWP properties. This error analysis is valuable because it offers a unique approach for assessing the skill of parameterized convective- and stratiform-type clouds.

Since ice clouds are recognized to have a significant impact on climate, especially when normalized by their relatively large occurrence frequency (*Berry and Mace* 2014), another study is performed on the radiative heating rates of ice clouds that commonly form

in regions of atmospheric ascent (Chapter 4). Since CloudSat and CALIPSO can, together, resolve the vertical structure of optically thin and thick ice clouds, we can more confidently estimate their vertical distribution of radiative heating in the atmosphere. By presenting the radiative heating rate profiles as a function of cloud and environmental parameters, such as the ice water path (IWP) and water vapor, we effectively demonstrate how radiative heating rates can be used to evaluate global models and diagnose how imposed changes to cloud parameterizations (e.g., entrainment rates) can impact the simulation of clouds and their impacts on the radiation budget.

CHAPTER II

DATA AND TOOLS

Models

Global climate, or general circulation, models (GCMs) are useful for assessing changes in the Earth climate system over periods ranging from decades to centuries. In fact, the IPCC routinely diagnoses future climate change using an ensemble of GCMs. This section introduces the global models that are subject to evaluation in Chapter 3.

Coupled Model Intercomparison Project – Phase 5 (CMIP5)

CMIP5 brings together climate simulations developed by modeling centers from across the globe, with an ultimate goal of reducing the discrepancies and uncertainties in contemporary GCMs (*Taylor et al.* 2012). The main objectives proposed for CMIP5 include:

1) "assessing the mechanisms responsible for model differences in poorly understood feedbacks associated with the carbon cycle and with clouds;
2) examining climate "predictability" and exploring the predictive capabilities of forecast systems on decadal time scales; and, more generally,
3) determining why similarly forced models produce a range of responses."

CMIP5 experiments range from long-term (century time scale), decadal, to short-term time scales. Herein, Atmospheric Model Intercomparison Project (AMIP) type simulations are evaluated, which fall within the category of decadal time-scale predictions (1979–2008). The AMIP models are atmosphere-only models, meaning there is no coupling with ocean or sea-ice models. Sea surface temperature (SST) and sea-ice variations in the models are

climatologically prescribed. A more comprehensive summary about the CMIP5 project and the framework for other prediction experiments can be found in Taylor et al. (2012).

The simulated cloud and TOA radiation budgets from 28 models submitted to the AMIP in CMIP5, which are available from the Earth System Grid Federation (ESGF) through the Program for Climate Model Diagnosis and Intercomparison (PCMDI), are evaluated in Chapter 3. A list of these models, their associated modeling center (or group) name, horizontal and vertical grid spacing, and number of ensemble members is provided in Table 1. In the study by Li et al. (2012), the simulated ice cloud properties in an assortment of GCMs are also evaluated. As such, they provide a detailed description (their Table 1b) of the CMIP5 model microphysical parameterizations and the reader should refer to that paper for more detail. The next installment of model intercomparison projects, CMIP6, is scheduled to be released to the public soon (as of June 2018).

Table 1: A list of the 28 CMIP5 AMIP GCMs and five reanalyses evaluated in this study. The horizontal grid spacings and number of vertical levels are provided along with the number of ensemble members for each GCM generated by the modeling centers.

Modeling Center (or Group)	**Model Name**	**Grid Spacing (lon × lat) Vertical Levels**	**Ensemble Members**
Commonwealth Scientific and Industrial Research Organization (CSIRO) and Bureau of Meteorology (BOM), Australia	ACCESS1.0	1.875° × 1.25°, L38	1
Beijing Climate Center, China Meteorological Administration	BCC-CSM1.1 BCC-CSM1.1(m)	1.25° × 1.25°, L26 2.8125° × 2.815°, L26	3 3

Modeling Center (or Group)	Model Name	Grid Spacing (lon × lat) Vertical Levels	Ensemble Members
College of Global Change and Earth System Science, Beijing Normal University, China	BNU-ESM	2.8125° × 2.8125°, L26	1
Canada Centre for Climate Modeling and Analysis	CanAM4	2.8125° × 2.8125°, L35	4
National Center for Atmospheric Research (NCAR), USA	CCSM4	1.25° × 0.9375°, L26	6
Community Earth System Model Contributors (NSF-DOE-NCAR), USA	CESM1(CAM5)	1.25° × 0.9375°, L30	2
Centro-Euro-Mediterraneo per I Cambiamenti Climatici, Italy	CMCC-CM	0.75° × 0.75°, L31	3
Centre National de Recherches Meteorologiques/Centre Europeen de Recherche et Formation Avancees en Calcul Scientifique, France	CNRM-CM5	1.4° × 1.4°, L31	1
Commonwealth Scientific and Industrial Research Organization in collaboration with Queensland Climate Change Centre of Excellence, Australia	CSIRO-Mk3.6.0	1.875° × 1.875°, L18	10
LASG, Institute of Atmospheric Physics, Chinese Academy of Sciences CESS, Tsinghua University	FGOALS-g2 FGOALS-s2	2.8125° × 1.666°, L26 2.8125° × 3.0°, L26	1 3
National Oceanic and Atmospheric Administration (NOAA) - Geophysical Fluid Dynamics Laboratory, USA	GFDL-CM3 GFDL-HIRAM-C180 GFDL-HIRAM-C360	2.5° × 2.0°, L48 0.625° × 0.5°, L32 0.3125° × 0.25°, L32	5 3 2
National Auronautics and Space Administration (NASA) - Goddard Institute for Space Studies	GISS-E2-R	2.5° × 2.0°, L29	10
Met Office Hadley Centre, United Kingdom	HadGEM2-A	1.875° × 1.25°, L38	6
Institute for Numerical Mathematics, Russia	INM-CM4	2.0° × 1.5°, L21	1

Modeling Center (or Group)	Model Name	Grid Spacing (lon × lat) Vertical Levels	Ensemble Members
Inststut Pierre-Simon Laplace, France	IPSL-CM5A-LR IPSL-CM5A-MR IPSL-CM5B-LR	3.75° × 1.875°, L39 2.5° × 1.25°, L39 3.75° × 1.875°, L39	6 3 1
Atmosphere and Ocean Research Institute (The University of Tokyo), National Institute for Environmental Studies, and Japan Agency for Marine-Earth Science and Technology	MIROC5	1.4° × 1.4°, L40	2
Max Planck Institute for Meteorology, Germany	MPI-ESM-LR MPI-ESM-MR	1.875° × 1.875°, L47 1.875° × 1.875°, L95	3 3
Meteorological Research Institute, Japan	MRI-AGCM3.2H MRI-AGCM3.2S MRI-CGCM3	0.5625° × 0.5625° 0.1875° × 0.1875° 1.125° × 1.125°, L35	3 1 3
Norwegian Climate Centre	NorESM1-M	2.5° × 1.875°, L26	3
NOAA Cooperative Institute for Research and Environmental Science (CIRES)	20CR v2	1.9° × 1.875°, L28	---
National Center for Environmental Prediction (NCEP)	CFSR	0.31° × 0.31°, L64	---
European Centre for Medium-Range Weather Forecasts (ECMWF)	Era-Interim	0.75° × 0.75°, L60	---
Japan Meteorological Agency and the Central Research Institute for Electric Power Industry	JRA-25	1.13° × 1.13°, L40	---
NASA Global Modeling and Assimilation Office (GMAO)	MERRA	0.5° × 0.67°, L72	---

For cloud simulations, the AMIP models are comparable with their coupled counterparts, which are linked to fully dynamic ocean models, although both versions have their own biases (*Lauer and Hamilton* 2012). Therefore, the biases in simulated cloud and radiation do not originate from discrepancies in the representation of SST fields, but rather

from the cloud simulations themselves, such as in convective and boundary layer cloud parameterizations.

Reanalyses

Five contemporary reanalyses are chosen to further populate the multimodel mean statistics generated for this evaluation study. Reanalyses can be used for a variety of applications, such as providing forcing data for single-column and cloud resolving models (*Xie et al.* 2004; *Kennedy et al.* 2011), investigating extreme/severe weather (*King and Kennedy* 2018) and climate (*Dong et al.* 2014), and examining forecast skill. Reanalyses also provide the data necessary for performing studies in data-sparse regions where ground-based observations are often difficult to obtain (*Dong et al.* 2014, *Zib et al.* 2012). While reanalyses offer a resource for investigating climate processes and predictability, and extreme events, the errors in the reanalyzed variables should be addressed (*Rienecker et al.* 2011). Twelve years of reanalysis data from 03/2000 – 02/2012 are collected and compared with GCMs, satellite, and ground-based observations. Here, a quick overview of the global reanalysis products is provided. The reanalyses highlighted here are also listed in Table 1.

Twentieth Century Reanalysis (20CRv2). The National Oceanic and Atmospheric Administration (NOAA) Cooperative Institute for Research in Environmental Sciences (CIRES) Twentieth century reanalysis (20CR) data set implements the ensemble Kalman filtering (*Whitaker and Hamill* 2002) technique with a background field supplied by an ensemble of forecasts from a global numerical weather prediction (NWP) model

(*Compo et al.* 2011). Only synoptic scale surface pressure, and prescribed monthly mean sea surface temperatures and sea ice distributions are ingested into the assimilation cycle. Compo et al. (2011) and Zib et al. (2012) provided a summary of updates to this experimental version of the coupled atmosphere-land model from the NCEP Global Forecast System (GFS). Updates include changes to the prognostic cloud condensate scheme (*Moorthi et al*. 2001), revisions to the solar radiative transfer model (*Hou et al*. 2002), and a Rapid Radiative Transfer Model (RRTM) for LW radiative transfer (*Mlawer et al*. 1997). Cloud liquid water is a prognostic quantity from which CF is diagnosed. Clouds are also assumed to be maximum–random overlapped. Atmospheric state conditions are computed every six hours for more than 140 years (1871 through 2012), providing the longest reanalysis data set on record. This product is an invaluable one, provided its own uncertainties, essential for understanding the long-term climate variability and useful for validation studies and model evaluation.

Climate Forecast System Reanalysis (CFSR). The National Center for Environmental Prediction (NCEP) has developed a fully coupled ocean–land–atmosphere model using NWP techniques to assimilate (i.e., 3D-VAR) and predict atmospheric states. Although the ocean–atmosphere coupling is only valid at latitudes between 64°N and 74°S, it is still an improvement from previous versions of the model where only the tropical Pacific Ocean was coupled. Also, the ocean model has been upgraded (Modular Ocean Model version 4, MOM4) and the new atmosphere model (GFS) has allowed for increased vertical resolution from 28 to 64 sigma levels (*Saha et al*. 2006). Radiation calculations are

diagnostically determined from the prognostic cloud condensate microphysics parameterization (*Zhao and Carr* 1997; *Sundqvist et al.* 1989; *Moorthi et al.* 2001), while cloud macrophysics assumes a maximum-random cloud overlap (*Saha et al*. 2006).

Era-Interim. Developed at the European Centre for Medium-Range Weather Forecasts (ECMWF), Era-Interim has been created in response to several data assimilation problems encountered in its preceding version, Era-40. Some of these problems are within the hydrological cycle, stratospheric circulation, and time consistency in the reanalyzed geophysical fields (*Dee et al*. 2011). Many changes have been implemented to convective and boundary layer cloud schemes. One of the main impacts of the modified convective cloud scheme is that it can be triggered at night, which increases the atmospheric stability and produces less precipitation (*Dee et al*. 2011). The new moist boundary layer scheme has resulted in producing more stratocumulus clouds in areas where they had previously been underpredicted (e.g., west coast of North America, South America, and Africa) because of updates in the inversion strength and height (*Köhler et al.* 2011). The fully prognostic cloud scheme links cloud generation to physical processes such as convection, vertical motion, radiative heating and turbulence (*Jakob* 1998). Radiation is computed based on the RRTM (*Mlawer et al*. 1997).

Japanese 25-year Reanalysis (JRA-25). The Japan Meteorological Agency (JMA) and the Central Research Institute for Electric Power Industry (CRIEPI) have produced the JRA-25 for seasonal prediction and climate research studies. Assimilations

are produced every six hours during the analysis period. JRA-25 utilizes assimilation data that are unused (by other reanalyses) in their analysis, especially those in Eastern Asian and in the tropics (*Onogi et al.* 2007). The Arakawa-Schubert prognostic mass-flux scheme (*Arakawa and Schubert* 1974) is applied for cumulus parameterizations (*Onogi et al*. 2007), where the vertical profile of upward mass flux is assumed to be linear with height (*Moorthi and Suarez* 1992) and the mass flux at the cloud base is calculated using a prognostic equation (*Randall and Pan* 1993). However, for stratocumulus clouds, CF is determined by a function of inversion strength (*Kawai and Inoue* 2006), and thus improves the simulated marine stratocumulus clouds on the west coast of continents. The radiation fields are also improved where LW emissions are calculated based on Sugi et al. (1990) while the SW scattering and absorption are simulated based upon *Joseph et al.* (1976) and *Coakely et al.* (1983).

Modern Era Retrospective Analysis for Research and Applications (MERRA and MERRA version 2). MERRA is a product of the NASA Goddard Earth Observing System version 5 (GEOS-5) and data assimilation system (DAS). The atmospheric general circulation model (AGCM) includes a prognostic cloud parameterization scheme (*Bacmeister et al.* 2006) to which a maximum-random overlap is assumed, a SW radiation scheme from Chou and Suarez (1999), and a LW radiation scheme from Chou et al. (2001). To constrain the atmospheric model with observations, GEOS-5 uses an Incremental Analysis Update (IAU) (*Bloom et al.* 1996) to slowly adjust the model states toward the observed state, which is unique to the MERRA assimilation process. To resolve boundary

layer clouds, two turbulent mixing schemes are implemented for (1) no boundary layer clouds in stable conditions (*Louis et al*. 1982) and for (2) unstable or cloud-toped boundary layers (*Lock et al*. 2000). The first version of MERRA is used in Chapter 3. However, a newer version, MERRA-2, was released and used in Chapter 4.

MERRA-2 is horizontally discretized on a cubed sphere grid, which is superior to the latitude-longitude methods used in earlier versions (*Bosilovich et al*. 2015). For MERRA-2 the number of assimilated observations per 6-hour increment has increased from three million in 2010 to five million in 2015; however, capabilities of assimilating future satellite observations are also developed. This is in contrast to the one and a half million observations assimilated in MERRA from 2002 to the present. MERRA-2 is available on a 0.5° × 0.625° grid with 72 hybrid-eta levels from the surface to 0.01 hPa as instantaneous and time-averaged products at synoptic (0, 6, 12, and 18 UTC) and mid-synoptic times (3, 9, 15, and 21 UTC).

One of the major improvements in MERRA-2 includes the minimization of abrupt variations in global inter-annual states (e.g., temperature) due to changes in observing system. This is accomplished by constraining the global dry mass balance, which permits the global changes in water by the analysis increment to be near zero (*Takacs et al*. 2016). Also, land-surface hydrology is improved by forcing precipitation through an observation-corrected field rather than a model-corrected field (*Reichle and Liu* 2014). In terms of the zonal temperature, MERRA-2 is within 1 K of its previous version. In the middle to upper troposphere, differences of up to 0.6 K are seen in the tropics with MERRA-2 being slightly

warmer (*Bosilovich et al*. 2015). Differences in the tropical tropospheric temperature are consistent with the additional radiative heating related to excess tropical cloud cover. An increase in tropospheric humidity is achieved in MERRA-2, likely a result of increased re-evaporation rates of frozen precipitation (*Molod et al*. 2015).

Satellite and Ground-based Observations

This section details the numerous satellite and ground-based data products used to complete the studies outlined in this dissertation. The satellite products are almost exclusively developed using instruments in the A-Train, a constellation of seven satellites flying in a sun-synchronous orbit at ~705 km above the Earth. The A-Train has a cross-equatorial orbit at ~1:30 pm local time with ~15 overpasses a day. A list of the satellite-based observation products examined here for the evaluation of clouds, precipitation, and radiation budgets is provided in Table 2 along with their data availability range and estimated uncertainties.

Clouds and the Earth Radiant Energy System (CERES) and Moderate Resolution Imaging Spectroradiometer (MODIS)

SYN1deg Edition 3A. Chapter 3 Section 1 applies eight years (02/2000–02/2008) of monthly mean combined Terra/Aqua MODIS retrievals (supplemented by geostationary satellite cloud properties) for the evaluation of total column CF and CWP (liquid and ice water). The data used for this study are from the Level-3 SYN1deg product, Edition 3A which is offered on a 1.0 ° × 1.0 ° (latitude × longitude) grid. For the remainder of this

document, this product will be referred to as CERES-MODIS, which is different from the MODIS-only cloud product. MODIS has 36 spectral channels ranging from visible to thermal infrared (IR) wavelengths (0.4–14.4 μm). The swath width is 2330 km across track with a 10 km along track at nadir. MODIS pixels are spatially resolved at 250, 500, and 1000 m for certain spectral bands. Cloud properties are generally derived from channels in the near- to thermal-IR bands (~3.6–14.4 μm).

Due to the large uncertainties in the nighttime CWP retrievals (> 50 gm^{-2}), daytime-only estimates of CF and CWP are used (as in *Stanfield et al.* 2014 and *Dolinar et al.* 2015) for the evaluation in Chapter 3. The CERES-MODIS cloud properties have been extensively validated with other space-borne satellites (*Minnis et al.* 1999, 2002, 2011) and ground-based measurements (*Dong et al.* 2008a; *Xi et al*. 2010, 2014). For example, Dong et al. (2008a) compared the CERES-MODIS retrieved cloud liquid water path (LWP) with the Department of Energy (DOE) Atmospheric Measurement (ARM) program ground-based microwave radiometer retrieved LWPs at the Southern Great Plains (SGP) Central Facility site. Based on their analysis, the mean LWP differed by 0.6±49.9 gm^{-2}. Minnis et al. (2011) found that the CERES-MODIS derived LWP over the ocean was, on average, 0.2±53.6 gm^{-2} less than the LWP from matched overcast Advanced Microwave Scanning Radiometer – Earth Observing System (AMSR-E) footprints. The CERES-MODIS ice water path (IWP) retrievals show an average negative bias of 3.3±16.2 gm^{-2} when compared with ground-based radar measurements (*Mace et al.* 2005). A more detailed survey of the CERES-MODIS cloud microphysical property retrievals and uncertainties

can be found in Minnis et al. (2011). A summary of the satellite data products used in Chapter 3 for evaluating GCMs and reanalyses is available in Table 2.

Table 2: A list of the level-3 monthly gridded satellite data products relevant to the evaluation of simulated cloud, precipitation, and radiation properties (Chapter 3) along with their uncertainties.

	Product Grid Spacing	**Product Availability**	**Error/ Uncertainty**
CERES MODIS	1.0° × 1.0°	03/2000 - 02/2017	
CF			7%
CWP			15%
ISCCP	2.5° × 2.5°	07/1983 - 12/2009	
CF			10%
CloudSat/CALIPSO		07/2006 - 12/2010	
CF			5%
CERES EBAF	1.0° × 1.0°	03/2000 - 02/2017	
TOA SW [all]			4.0 W m^{-2}
TOA SW [clear]			2.6 W m^{-2}
TOA LW [all]			2.0 W m^{-2}
TOA LW [clear]			3.6 W m^{-2}
SFC SW [all]			5.0 W m^{-2}
SFC LW [all]			7.0 W m^{-2}
TRMM	0.25° × 0.25°	01/1998 - 04/2015	
PR			20–120%

CERES Aqua Single Scan Footprint (SSF) Edition 4A. Satellite top-of-atmosphere (TOA) radiative fluxes are estimated from the CERES Aqua Single Scan Footprint (SSF) edition 4A product since the launch of Aqua in 2002 (*Geier et al*. 2001; *Loeb et al.* 2003). Satellite-measured radiances are from a SW channel (0.3–5 μm), a window channel (8–12 μm), and a total channel (0.3–100 μm) (*Wielicki et al.* 1996). TOA SW radiances are then converted to fluxes using angular distribution models (ADMs; *Su et*

al. 2015a), which consider the solar zenith, viewing zenith, and relative azimuth angles. The MODIS imager supplements CERES to provide better detail regarding the distribution of clouds and aerosols. The collocation of clouds, aerosols, and radiation is a major benefit to the SSF product. Included in the SSF product are estimates of clear-sky fraction, which is used for cloud screening purposes, as described in Chapter 4 Section 1. TOA SW and LW flux root-mean-square errors (RMSE) are estimated to be less than 6% for a variety of scene types (*Loeb et al.* 2006; *Su et al*. 2015b). Instantaneous footprints of TOA radiances are used as a constraint to the calculated fluxes presented in Chapter 4 Section 1.

CERES Energy Balanced and Filled (EBAF) – TOA and Surface Edition 2.8. CERES energy balanced and filled (EBAF) radiative fluxes at the TOA are a standard source for evaluating simulations of global TOA radiation budgets. As an extension of the CERES SYN1deg product, CERES EBAF is also a monthly mean 1.0° × 1.0° gridded dataset supplemented by TOA fluxes derived from five geostationary satellites (*Doelling et al.* 2013). Edition 2.8 is consistent with previous EBAF versions, in that the CERES SW and LW fluxes are adjusted so that the global net TOA flux and the earth-atmosphere heat storage are consistent with each other, as determined by the ocean heat content anomaly data (*Loeb et al.* 2009). Edition 2.8 fluxes are nearly identical to Edition 2.7; however, the incoming solar irradiances are from the solar radiation and climate experiment (SORCE) total irradiance monitor (TIM) total solar irradiance (TSI) V-15 for March 2000 through June 2013, and from the Royal Meteorological Institute of Belgium (RMIB) from July to the present. The CERES EBAF-TOA RMSEs for the all-sky reflected SW radiation, clear-

sky reflected SW radiation, all-sky outgoing LW radiation, and clear-sky outgoing LW radiation are 4.0, 2.6, 2.0, and 3.6 W m^{-2}, respectively (*CERES EBAF_Ed2.8 Data Quality Summary* 2014; *Loeb et al.* 2012).

The CERES EBAF-Surface product is derived using the CERES SYN1deg-lite product, adjusted within its uncertainty to be consistent with the net planetary imbalance derived from ocean heating rates from Argo in situ ocean temperature measurements (*Loeb et al.* 2012), as well as input from CERES EBAF–TOA. CERES radiances are observed using CERES FM1-4 instruments onboard Terra and Aqua satellites. The global surface radiation budget is determined through radiative transfer model (RTM) calculations, which are constrained by satellite-based cloud and aerosol retrievals and meteorological and aerosol assimilation data from reanalysis to characterize the atmospheric state. To minimize the error in surface fluxes due to uncertainties in the input data sources, the EBAF-Surface data product introduces several additional constraints based upon information from other independent data sources, such as CERES TOA fluxes, AIRS-derived temperature/humidity profiles, and CALIPSO/CloudSat-derived vertical profiles of clouds. On global average, the errors/uncertainties of EBAF-Surface fluxes are 7.0 and 3.0 W m^{-2} for downward and upward LW fluxes, respectively. The downward and upward SW flux uncertainties are 5.0 and 3.0 W m^{-2}, respectively (*Kato et al.* 2013).

International Satellite Cloud Climatology Project (ISCCP) - D2

The ISCCP estimated CF is also briefly referenced in Chapter 3. ISCCP combines cloud information routinely derived from operational weather satellites. While no comprehensive analysis is performed with these data, they provide a consistency check for the CERES-MODIS CF (global average within 0.1 %, Pearson correlation coefficient squared, $R^2 = 0.84$) and a global satellite data record for assessing clouds dating back to the early 1980's.

CloudSat and Cloud-Aerosol Lidar and Infrared Pathfinder Satellite Observation (CALIPSO)

When CloudSat and CALIPSO were launched into orbit in 2006, the ability to detect optically thin ($\tau < 0.3$) and multi-layered cloud systems across the entire globe was achieved. Furthermore, when the active sensors on these satellites are integrated with sensors on other satellites within the A-Train (e.g., Aqua), a more complete picture of complex cloud systems (e.g., deep convection and mixed-phase clouds), especially during nighttime, can be painted. With the combination of the CloudSat 94 GHz cloud profiling radar (CPR; *Stephens et al.* 2002) and the Cloud-Aerosol Lidar with Orthogonal Polarization (CALIOP; 532 and 1064 nm; *Winker et al*. 2009) coincident measurements of vertically-resolved aerosols, subvisible and thin cirrus, and optically-thick clouds are attainable on the global scale (*Deng et al.* 2010 and 2015). The CPR measures backscattered power every 240 m vertically on a footprint of 1.4 km × 1.8 km (across × along track) with a sensitivity of –30 dBZ_e (*Deng et al.* 2010). CALIOP, on the other hand,

measures the attenuated backscatter every 30 – 70 m vertically on a footprint of 0.075 km × 0.3 – 1.0 km (across × along track) (*Deng et al.* 2010).

CloudSat/CALIPSO/CERES/MODIS (CCCM) RelB1v2. The integrated CloudSat, CALIPSO, CERES, and MODIS (CCCM) merged lidar/radar product provides instantaneous retrieved cloud property vertical profiles in the CloudSat/CALIPSO ground track (*Kato et al*. 2010). In Chapter 3, the estimated CF from CloudSat/CALIPSO is compared with the other satellite observations and model simulations since no statistical difference is determined from the MODIS-in-CloudSat/CALIPSO swath and Single Scanner Footprint (SSF) products (*Xi et al.* 2014).

In Chapter 4 Section 2, we introduce the instantaneous TOA irradiances derived by CERES from the single scanner footprint (SSF) Edition3-Beta2 product reported in CCCM. TOA fluxes are obtained by applying empirical ADMs to CERES-observed SW and LW radiances (*Loeb et al.* 2005). CCCM also offers calculated irradiance profiles from the surface to the TOA (138 levels) with MODIS-derived cloud properties from an enhanced CERES algorithm, integrated with measured cloud information from and along the CloudSat and CALIPSO ground track (*Kato et al.* 2011). The CCCM-calculated irradiances from this dataset will be referred to as CCCM_CC. Kato et al. (2010 and 2011) provided more extensive assessments of how CloudSat, CALIPSO, and MODIS cloud scenes are integrated to produce a coherent cloud signal and how the irradiance profiles are calculated in CCCM_CC.

CloudSat and CALIPSO Ice Cloud Property Product (2C-ICE, P1_R04). In Chapter 4 Section 2, the retrieved ice cloud properties (i.e., IWC and R_e) come from the merged CloudSat and CALIPSO Ice cloud property product (2C-ICE P1_R04; *Deng et al.* 2010 and 2015). Ice cloud boundaries are defined from the 2B-GEOPROF-LIDAR (*Mace et al*. 2009) and 2B-CLDCLASS-LIDAR products (*Sassen et al.* 2008). The 2C-ICE algorithm defines three separate regions within a profile: the lidar-only, radar-only, and the lidar-radar overlap regions. These zones are defined based upon sensor sensitivity/attenuation, which allows for respective data processing methodologies in each region (e.g., parameterizations or measurement error assignment; *Deng et al.* 2010).

The largest sources of uncertainty in 2C-ICE result from the retrieval algorithm assumptions related to ice particle size distributions (PSD; a modified gamma distribution in this algorithm; *Deng et al.* 2010) and particle habit oversimplification, multiple scattering assumptions related to the lidar signal, and the radar reflectivity parameterizations in the lidar-only region (*Deng et al.* 2015). Errors in the assumptions based on multiple scattering can lead to an uncertainty of ~15% in optical depth and ~30% in IWC. The cloud ice particle effective radii (R_e), available in the 2C-ICE product, were computed from the best estimate of PSD. Since there are no global direct measurements of R_e to date (*Jiang et al*. 2017), large uncertainty may exist in the R_e used for the radiative transfer modeling.

ECMWF-AUX (P_R05). Meteorological profiles (i.e., temperature, water vapor, and ozone) are available from the European Centre for Medium-range Weather Forecasting

(ECMWF) auxiliary product, which are interpolated to the CloudSat radar bins from the surface to ~25 hPa. These data are commonly used for the development of other CloudSat-based products (e.g., 2B-GEOPROF-LIDAR, 2B-FLXHR-LIDAR, 2B-TAU) when atmospheric state variables are required.

2C-PRECIP-COLUMN (P_R05). The 2C-PRECIP-COLUMN product provides estimates of detectable precipitation based on CloudSat CPR observations *(Haynes et al.* 2009). For the purposes of the studies completed here in Chapter 4 Section 2, precipitation detection is sufficient. However, the rate of precipitation and probability of precipitation types (e.g., possible, probable, and certain, rain, snow, or mix) is given.

2B-FLXHR-LIDAR (P2_R04). The 2B-FLXHR-LIDAR (*L'Ecuyer et al*. 2008; *Henderson et al*. 2013) product provides estimates of broadband radiative flux profiles from the surface to the lower stratosphere at the observed CloudSat CPR range gates (125 levels). Liquid and ice cloud properties and precipitation are derived from observed CPR, CALIOP, and MODIS properties. Henderson et al. (2013) provided a detailed description of how liquid and ice clouds are represented in 2B-FLXHR-LIDAR, including sensor limitations and how these limitations are minimized. These data are used in Chapter 4 Section 2 for comparisons of TOA radiative fluxes and heating rate profiles.

Microwave Limb Sounder (MLS) version 4 Level 2

Launched in 2004, the Aura satellite became the second member of the A-Train (*L'Ecuyer and Jiang* 2010). Aura is equipped with the Microwave Limb Sounder (MLS)

instrument (*Waters et al.* 2006), which was designed to obtain high-quality measurements of upper atmospheric temperature, water vapor, ozone, and an assortment of other climate sensitive atmospheric constituents. The acceptable range of the retrieved temperature is 261–0.001 hPa with an estimated uncertainty of ~1 K when compared with other observations (*Schwartz et al*. 2008). Stratospheric ozone from MLS is retrieved at a frequency of 240 GHz, which offers the best precision for a wide vertical range (*Froidevaux et al*. 2008). Intercomparison studies suggest that the ozone values from MLS match well with multi-instrument means and Stratospheric Aerosol and Gas Experiment II values (*Tegtmeier et al*. 2013). The recommended range of the MLS ozone product is from 261 to 0.02 hPa with an estimated uncertainty of ~5–10%. MLS water vapor is retrieved at a frequency of 190 GHz with acceptable range of 316–0.002 hPa. The estimated uncertainty of MLS water vapor in the stratosphere is ~10% (*Read et al*. 2007). In the upper troposphere, the estimated MLS water vapor uncertainty is 20% in the tropics and midlatitudes and ~50% at high latitudes (>60 °N/S) (*Read et al.* 2007; *Jiang et al*. 2012).

Atmospheric Infrared Sounder (AIRS)

The Aqua satellite also houses the AIRS sensor, which is a cross-track scanning hyper-spectral (2378 bands) spectrometer covering the infrared wavelengths from 3.7–15.4 μm. In the following studies, the level-3, version 6 daily 1.0° × 1.0° gridded product is used for tropospheric ozone estimates at standard pressure levels (*Tian et al.* 2014). Biases in the AIRS-retrieved ozone are estimated to be less than 5% when compared with collocated

ozonesonde profiles and World Ozone and Ultraviolet Radiation Data Center data sets (*Divakarla et al.* 2008).

Tropical Rainfall Measurement Mission (TRMM) 3B43 Version 7

Precipitation is another commonly investigated component of the Earth-climate system due to its potential agricultural, societal, and economic impacts. Herein, we only perform a brief investigation of the simulated precipitation rates in five reanalysis data sets using TRMM as a reference in Chapter 3 Section 1. The NASA Goddard Earth Sciences Data and Information Services Center (GES DISC) has released the seventh version of the TRMM monthly gridded (0.25° × 0.25°) rainfall product of near-global (50 °N/S) precipitation estimates beginning in 1998. This data product is derived based upon retrievals from an active 13.8 GHz microwave precipitation radar and is supplemented by several other sensors in the TRMM multi-satellite precipitation analysis (TMPA) (*Huffman et al.* 2007). The 3-hour precipitation rate uncertainty is estimated to be 90–120% for light rain (< 0.25 mm day^{-1}) and 20–40% for heavy rain (*Habib and Krajewski* 2002; *AghaKouchak et al.* 2009). However, many of these errors are random and will be reduced when spatially and temporally averaged. Huffman et al. (2007) reported that the monthly mean precipitation rates agree well with the Global Precipitation Climatology Project (GPCP; *Adler et al.* 2003), however, larger errors are common at smaller time scales over the oceans where low precipitation rates frequently occur. Estimated errors in the gridded product are sampling-induced uncertainties (i.e., the true precipitation field and of the

measurement-algorithm) of each field and a linear combination of the field errors, weighted by the inverse of its error variance (*Huffman* 1997).

Atmospheric Radiation Measurement (ARM) Program

The Department of Energy (DOE) has spearheaded an effort to study the interaction of clouds, radiation, aerosols, and precipitation at several climatologically unique locations across the globe. Figure 2 shows the locations of five different ground-based sites with instruments that have been operational since the mid-to-late 1990's. These instruments include millimeter wavelength cloud radar (MMCR), micropulse lidar (MPL), radiometers, wind profilers, rain gauges, laser disdrometers, ceilometers, sun photometers, and surface meteorology sensors. Aircraft measurements associated with carefully designed field campaigns are also available close in proximity to several of these sites.

Data from the five sites highlighted in Fig. 2 have been collected and processed in Chapter 3 Section 2 and Chapter 4 Sections 1 and 2. The Active Remote Sensing of Clouds (ARSCL) value-added product (VAP) (*Clothiaux et al.* 2000) contains derived cloud properties from a combination of MMCR, MPL, and laser ceilometer. The MMCR is a vertically pointing radar that operates at 8.6 mm and provides a continuous time series of cloud hydrometeors passing through the radar FOV, making it relatively easy to identify clear and cloudy scenes (*Moran et al.* 1998). Furthermore, the MMCRs can detect all cloud-types up to 16 km with a radar reflectivity ranging from –50 to +20 dBZ. Since a

combination of lidar and ceilometer measurements can offer the best estimate of cloud base height, they are also included in the algorithm (*Clothiaux et al.* 2000).

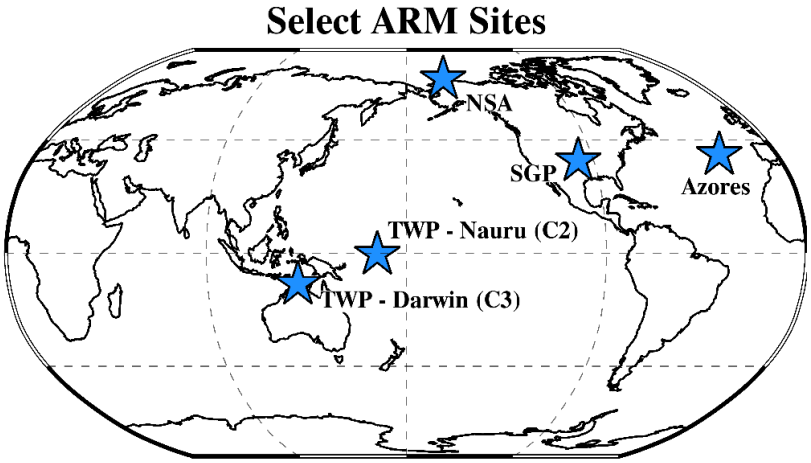

Figure 2: A global map showing the select ARM sites where data were collected and processed for the studies described in this document. Southern Great Plains (SGP; 36° 36'18" N, 97° 29'6" W), North Slope of Alaska (NSA; 71° 19'22.8" N, 156° 36'32.4" W), Azores (39° 5' 29.68" N, 28° 1' 32.34" W), Tropical Western Pacific (TWP) Nauru (C2; 0° 31'15.6" S, 166° 54'57.6" E), and Darwin (C3; 12° 25' 28.56" S, 130° 53' 29.75" E).

High-resolution vertical profiles of temperature and water vapor are available from the ARM-merged sounding VAP. The merged soundings are a combination of observations from radiosondes, microwave radiometers, surface-based meteorological instruments, and ECMWF model output (*Troyan* 2012). Using a sophisticated scaling/interpolation/smoothing algorithm, thermodynamic variables are available at 1-min intervals with a total of 266 levels from the surface to ~50 hPa.

Upward and downward looking standard Eppley precision spectral pyranometers (PSPs) and precision infrared pyrgeometers provide measurements of the surface

downward/upward SW (0.3–3 μm) and LW (4 –50 μm) radiative fluxes, as well as albedo, at 1-min intervals (*Long and Shi* 2008). Uncertainty estimates in the downward SW and LW radiative fluxes are 10 and 4 W m^{-2}, respectively (*Long and Shi* 2008). The observed surface downward SW and LW fluxes are used to constrain the calculated fluxes in Chapter 4 Section 1 and are simply compared with calculated fluxes in Chapter 3 Section 2 and Chapter 4 Section 2. Measurements of the surface skin temperature at the ARM SGP and NSA sites are also needed for Chapter 4 Section 2; skin temperature is not available at the ARM TWP-C3 for the study period. Therefore, we used the lowest level in the merged sounding as an approximation. The equivalent blackbody temperature is measured by a downward looking infrared thermometer (9.6–11.5 μm) and is accurate to within ±0.5 K (*Morris* 2006).

Radiative Transfer Model (RTM)

In Chapter 4, Sections 1 and 2, radiative fluxes are calculated using a one-dimensional radiative transfer model (RTM) with inputs from satellite and ground-based observations. In Chapter 4 Section 1, broadband clear-sky SW and LW radiative fluxes are calculated using the NASA Langley modified Fu-Liou RTM (*Fu and Liou* 1993; *Fu et al.* 1997; *Kato et al.* 1999) (https://www-cave.larc.nasa.gov/cgi-bin/lflcode/accesslfl.cgi). The FLux model for CERES with k-distribution and correlated-k for Radiation (FLCKKR) RTM is used in Chapter 4 Section 2, which is an altered version of the NASA Langley modified Fu-Liou RTM, to calculate the TOA, surface, vertical profiles of radiative fluxes.

FLCKKR is used because it can read in profiles of IWC and R_e instead of the layer mean cloud R_e. We are interested in the vertical profiles of fluxes and their corresponding heating rates; therefore, it is desirable to resolve the cloud vertical structure in the RTM.

Infrared and solar radiative fluxes are calculated with several options: a δ-four- or δ-two/four-stream solver and a δ-two, δ-four, or gamma-weighted δ-two-stream solver, respectively (*Kato et al.* 2005). We use the two-stream solver for SW calculations, while the two/four-stream solver is used for the LW. For the SW and LW fluxes, a total of 18 and 14 bands are computed, respectively, and are sensitive to specific gaseous species. A total of 25 different aerosol types are featured in this model and are characterized by their own spectral normalized extinction, scattering, and absorption properties. Single-scattering ice particle properties (e.g., phase function, single-scattering albedo, and extinction coefficient) are parameterized through exploitation of in-situ aircraft data and based on the following assumptions: ice crystals are randomly oriented, ice crystal absorption is small, and ice crystals are non-spherical (assumed to be hexagonal here) (*Fu and Liou* 1993). The errors related to parameterized single-scattering properties of ice clouds are less than 1%.

CHAPTER III

AN EVALUATION OF SIMULATED CLOUDS, PRECIPITATION, AND TOA RADIATION BUDGETS IN GCMS AND REANALYSES USING NASA SATELLITE AND ARM GROUND-BASED OBSERVATIONS (Dolinar et al. 2015 and 2016a)

Globally observed and simulated clouds, precipitation, and TOA radiation budgets from 28 CMIP5 GCMs and five reanalyses

To assess the biases in the simulated cloud and radiation fields, the global mean properties are compared with consistent satellite observations for multiple years of data. Global means are calculated from grid-box averaged values and are weighted by cosine of latitude to compensate for the longitudinal convergence near the poles. All models, reanalysis, and satellite observations are linearly interpolated to a common grid (2.5° × 2.0°; longitude × latitude) to facilitate the comparison.

Cloud fraction (CF), cloud water path (CWP), and precipitation rate (PR)

Figure 3 provides the global means of total column cloud fraction (CF) and cloud water path (CWP) for each model or reanalysis (vertical bars, when available) and satellite product (horizontal dashed colored lines). On average, the multimodel mean CF (blue line) is underpredicted by ~7% and ~16% when compared with passive (i.e., CERES-MODIS or ISCCP; red and green lines) and active (i.e., CloudSat/CALISPO; black line) satellite retrieved CFs, respectively. The CloudSat/CALISPO global mean CF is larger than CERES-MODIS due to its higher sensitivity to optically thin clouds ($\tau < 0.3$; *Sassen and Cho* 1992). Only five models (CSIRO-Mk3.6.0, GFDL-HIRAM-C180, -C360, -CM3, and

20CR) fall within the range of observed CFs. The global mean CWP is also underpredicted by the multimodel mean by ~17 g m^{-2} when compared with the CERES-MODIS result. It is also worth noting the large degree of inter-model spread in the simulated global mean results. Based on the range of global means from the ensemble of models considered here, the standard deviations (σ) are ~10% and ~37% for CF and CWP, respectively.

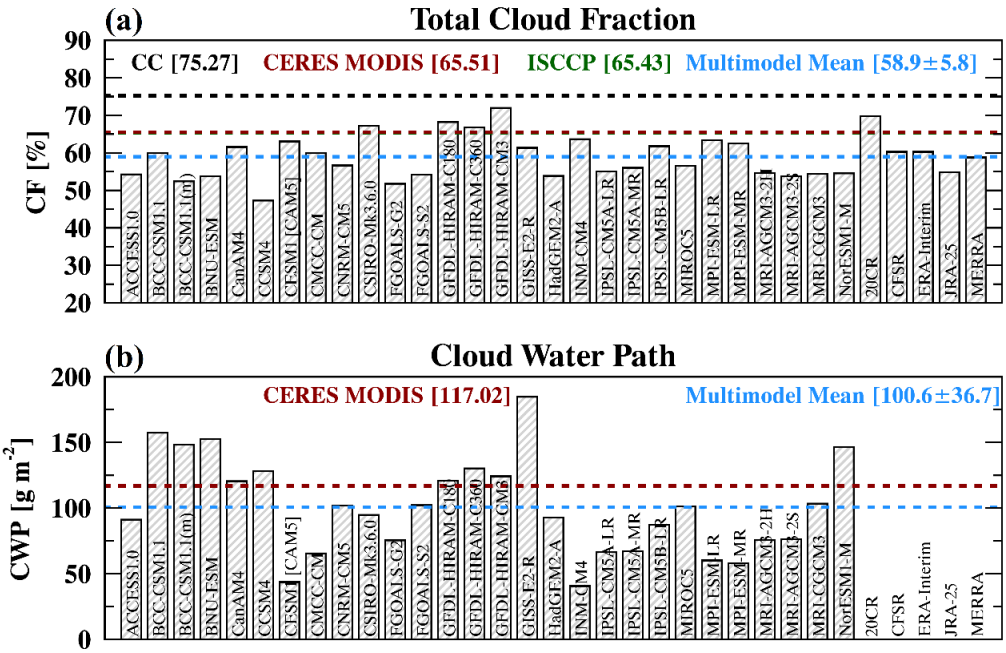

Figure 3: Bar plots of the globally averaged (a) total column cloud fraction (CF, %) and (b) cloud water path (CWP, g m^{-2}) from the 28 CMIP5 GCMs during 03/2000-02/2008 and five reanalyses during 03/2000-02/2012 overlaid with the multimodel mean (blue) and observed means from CERES-MODIS (red), ISCCP (green), and CloudSat/CALIPSO (black). Mean values are listed in parentheses along with the standard deviation for the multimodel mean.

Jiang et al. (2012) developed a grading scale to rate each model based upon spatial mean, standard deviation, and correlation of combined clouds and water vapor fields. They highlighted that there exists large model spread and a high degree of discrepancy from

observations, particularly in the upper troposphere. In many instances, when evaluating a multimodel ensemble, absolute model error is rather small. However, when evaluating models independently, the spread of the model results can be large because most GCMs use different cloud parameterization and radiation schemes, offering more complexity to these types of validation studies.

Figure 4 shows the zonal means of simulated and observed CF and CWP. The negative bias in simulated global mean CF occurs predominately in the extra-tropics and mid-latitudes when compared with CERES-MODIS, while the multimodel mean CF is overpredicted at the equator and poleward of 70° in both hemispheres. On average, the model simulated CF is underpredicted at all latitudes compared to CloudSat/CALIPSO. The model spread is considerably large in the high-latitudes (~50–60%, see shaded area) and tropics (~30%), indicating a significant amount of uncertainty regarding Arctic/Antarctic and ice clouds, respectively. The zonal mean CWP in Fig. 4b reveals a similar bias. On average, the CWP is overpredicted in the tropics and underpredicted poleward of ~25° in both hemispheres. The negative bias in the mid- to high-latitudes (~60–90 g m^{-2}) is accompanied by a large range of simulated results in this area (200-300 g m^{-2}, grey shaded region).

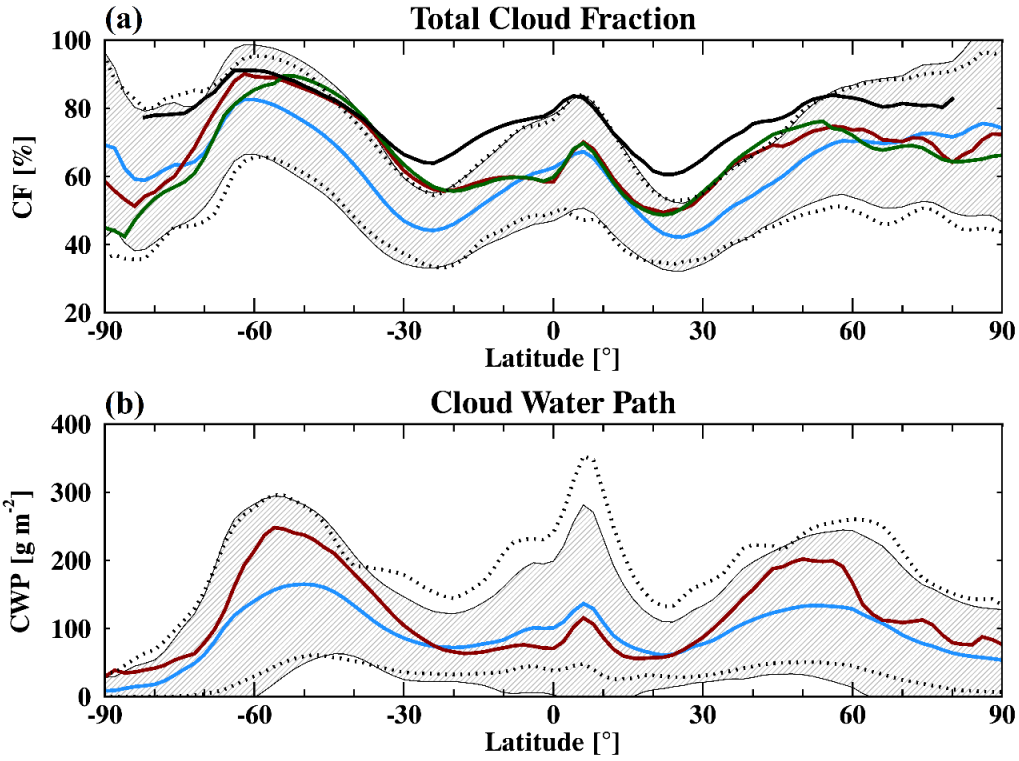

Figure 4: Zonal means of the globally simulated and observed (a) total column CF (%) and (b) CWP (g m^{-2}). The multimodel mean is in blue while the observed zonal means are in red, green, and black from CERES-MODIS, ISCCP, and CloudSat/CALIPSO, respectively. The grey shaded region is the ±2σ of the model results while the dotted lines are the maximum and minimum simulated values.

Global maps of the observed and modeled CFs are provided in Fig. 5. According to observations (Figs. 5a and 5b), CFs of more than ~80% occur in the Southern Ocean and Northern Pacific and Atlantic Oceans. CloudSat/CALIPSO detects a much higher CF in the tropical warm pool, compared with CERES-MODIS, due to the relatively large frequency of optically thin clouds in this region. The multimodel mean simulated CF is too low everywhere across the globe when compared with CloudSat/CALIPSO (Fig. 5d). When compared with CERES-MODIS, the simulated CF is too low over the global oceans

outside of the tropics and over much of the continents. However, the CF is most notably overpredicted in the tropical Pacific, Indian Ocean, Antarctica, and the Arctic Ocean.

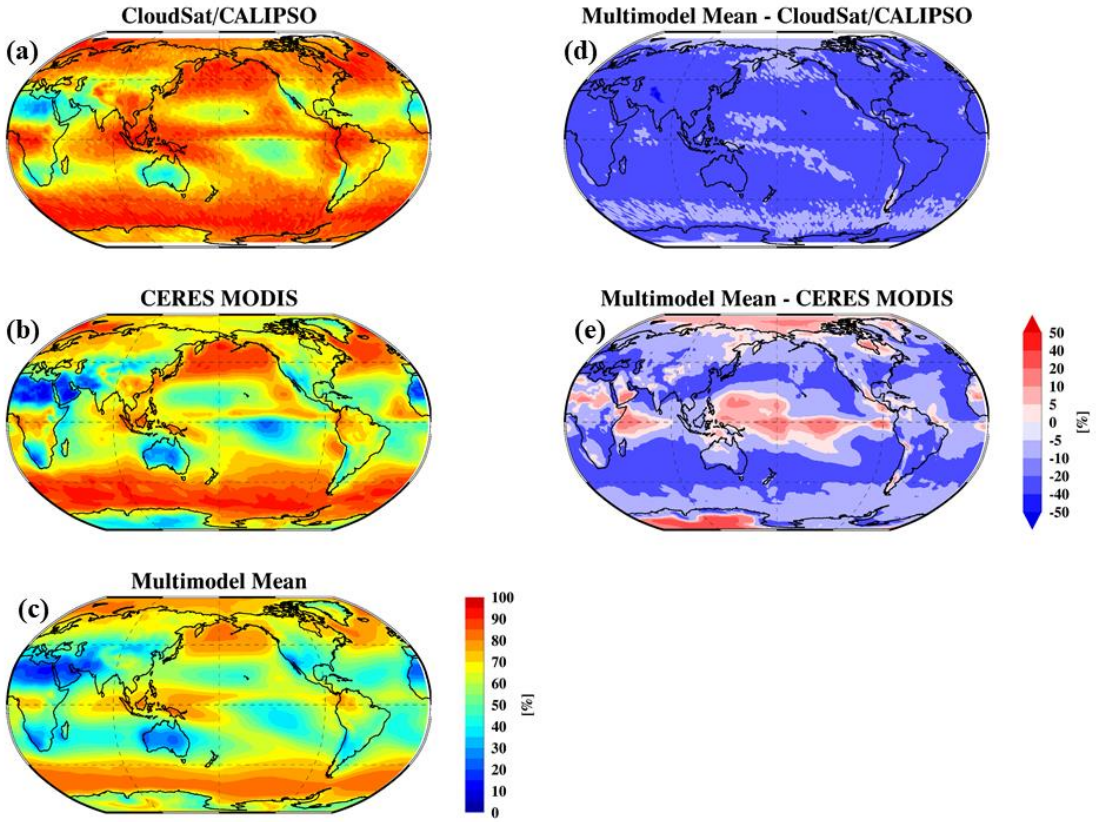

Figure 5: Global maps of the mean total column CF (%) from (a) CloudSat/CALIPSO, (b) CERES-MODIS, and (c) the multimodel mean from 28 CMIP5 GCMs and five reanalyses. Differences (model minus observation) are also shown between the multimodel mean and (d) CloudSat/CALIPSO and (e) CERES-MODIS.

Global maps of the CERES-MODIS observed and the multimodel mean simulated CWPs are depicted in Fig. 6. According to CERES-MODIS, the largest CWPs occur in the Southern Ocean and northern Pacific and Atlantic Oceans (CWP = 250–400 g m^{-2}) the

multimodel mean largely underpredicts CWP (biases of –60 to –120 g m^{-2}; see Fig. 6c). A small positive bias in the multimodel mean occurs in the tropical oceans while significantly large positive biases are determined over tropical land areas such as the Melanesian Islands, Northern South America, Central America, and Central African.

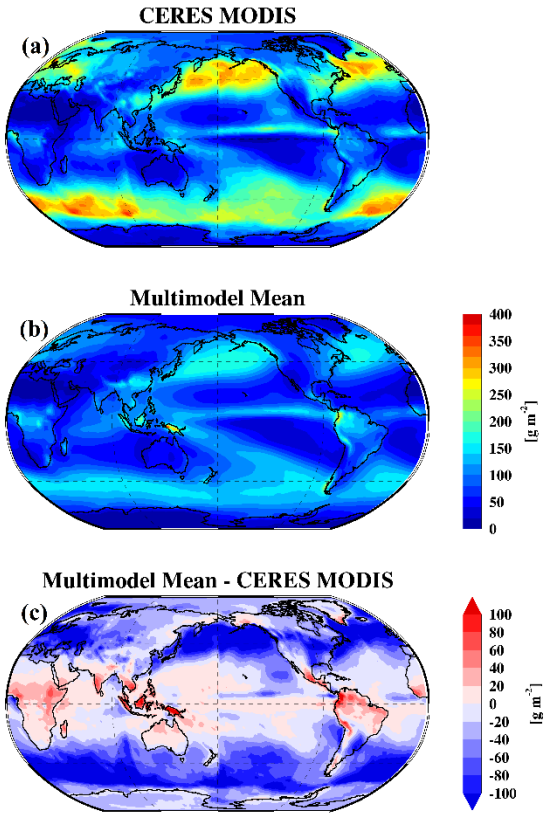

Figure 6: Same as Fig. 5 but for the global maps of CWP (g m^{-2}) from (a) CERES-MODIS, (b) the multimodel mean, and (c) their difference.

While this analysis does not differentiate between ice and liquid clouds in the multimodel means and observations, Stanfield et al. (2014) elaborates on the distinction between ice and liquid water paths (I/LWP) simulated in the GISS-E2-R model, and how they compare with CloudSat observations. Their analysis suggests that IWP (LWP) is generally over (under) predicted in the tropics while the opposite holds true in the mid- and high-latitudes. Li et al. (2012) investigated the simulated ice cloud properties in 15 CMIP5 GCMs and 14 from CMIP3. They concluded that the models can capture the global distribution of ice clouds but the magnitude is too high, especially in the tropics above 400 hPa.

The simulated precipitation rates (PR) from the five reanalyses are also investigated. We do not include the 28 GCMs for this analysis because precipitation is not a focus of this study. However, it is still important to understand how well global models predict precipitation, as it is commonly regarded as an important component of the Earth-climate system (*Stanfield et al.* 2016). Figure 7 depicts the global maps of TRMM-observed and model simulated PRs.

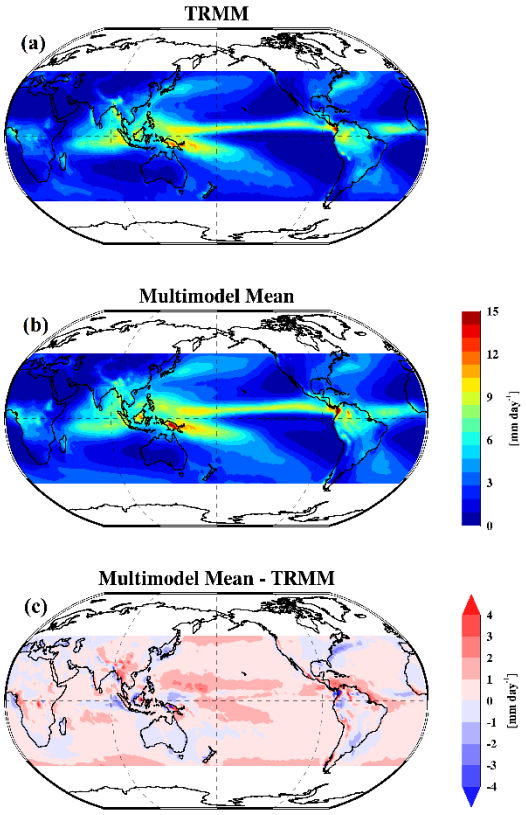

Figure 7: Near-global (±50°) maps of the precipitation rates (PR, mm day^{-1}) from (a) TRMM, (b) multimodel mean (reanalyses only), and (c) their difference.

As expected, the highest grid-average PRs (10–15 mm day^{-1}) from TRMM occur in the tropics along the Intertropical Convergence Zone (ITCZ) with moderate PRs occurring along mid-latitude storm tracks. Weaker PRs (< 1.0 mm day^{-1}) are found in areas of large-scale subsidence over the oceans (e.g., descending branch of the Hadley Cell) and over large desert regions (e.g., Sahara, Taklimakan, and Gobi, and Mojave Deserts). The near-global (50 °S – 50 °N) mean PR from TRMM is 2.91 mm day^{-1}. The multi-reanalysis mean captures this distribution very well (Fig. 4b), however, the near-

global mean is overpredicted by ~0.42 mm day^{-1} and the differences in Fig. 4c reveal biases of more than 2.0 mm day^{-1} in the western Pacific, along the Gulf Stream, and over tropical land masses.

TOA fluxes and cloud radiative effects (CRE)

The effects of clouds on the TOA radiation budget will be presented below in terms of the cloud radiative effect (CRE; *Ramanathan et al.* 1989). However, it is necessary to understand both components of the TOA CREs: the all-sky and clear-sky radiations budgets.

TOA clear-sky fluxes. The clear-sky radiation budgets are needed for calculating TOA CREs. It is the clear-sky conditions that hold reference to the all-sky conditions when investigating how clouds affect the radiation budget (TOA or surface). When evaluating the TOA clear-sky radiative fluxes, we assume the results are an indication of how well the surface properties are represented in the model (with some influence from the emissive and absorptive properties of the atmosphere). For example, the TOA clear-sky reflected SW flux depends greatly on the surface albedo while the outgoing LW flux depends heavily on the surface temperature. The observed global mean clear-sky TOA reflected SW and outgoing LW radiation fluxes from CERES EBAF are 52.6 and 266.0 Wm^{-2}, respectively (see Fig. 8). The multimodel (from available models) mean clear-sky SW and LW fluxes are 52.9±3.8 and 264.2±3.2 Wm^{-2}, respectively.

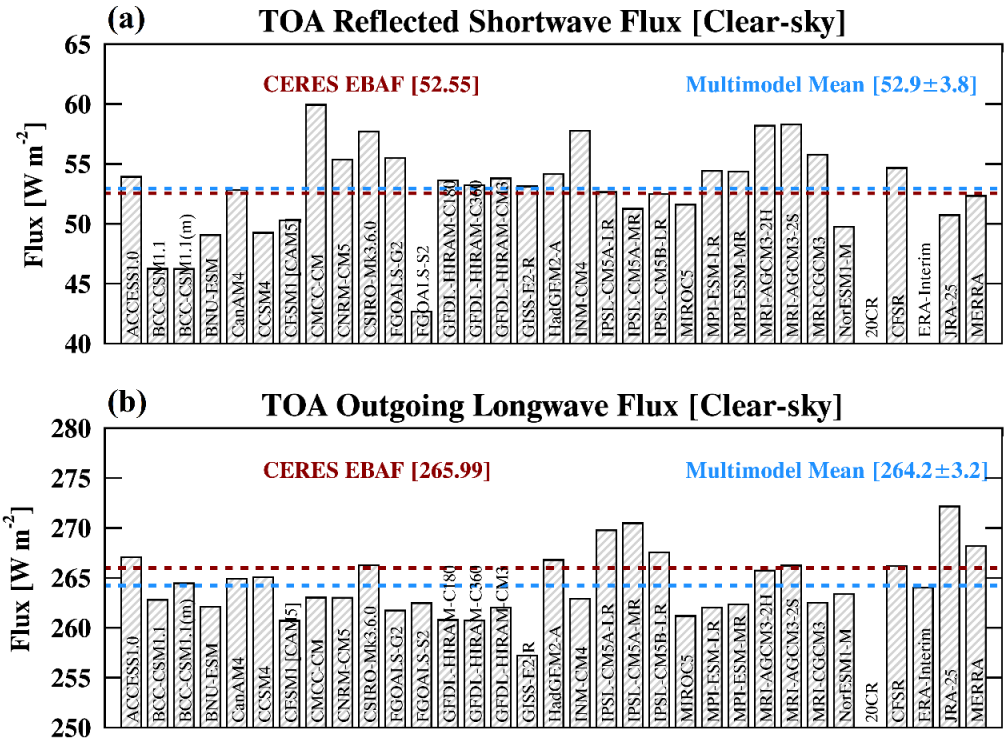

Figure 8: Same as Fig. 3 but for the clear-sky top-of-atmosphere (TOA) (a) reflected shortwave (SW) and (b) outgoing longwave (LW) fluxes (W m^{-2}). The observed clear-sky TOA radiative fluxes (red) come from CERES EBAF.

Figure 9 presents the zonal distributions of the clear-sky TOA fluxes. The SW flux does not vary much between 60 °N/S but increases significantly at the southern and northern poles. This increase is due to the continual snow and ice cover from year to year, increasing the surface albedo. The oceans maintain the surface albedo well, which explains the small variation between 60 °N/S. There is a slight increase in the clear-sky SW flux in the northern hemisphere due to the larger percentage of land area (and increase in surface albedo). The model simulations depict these conditions with accuracy; however, there is relatively large multimodel spread (~30 W m^{-2}) in the Arctic.

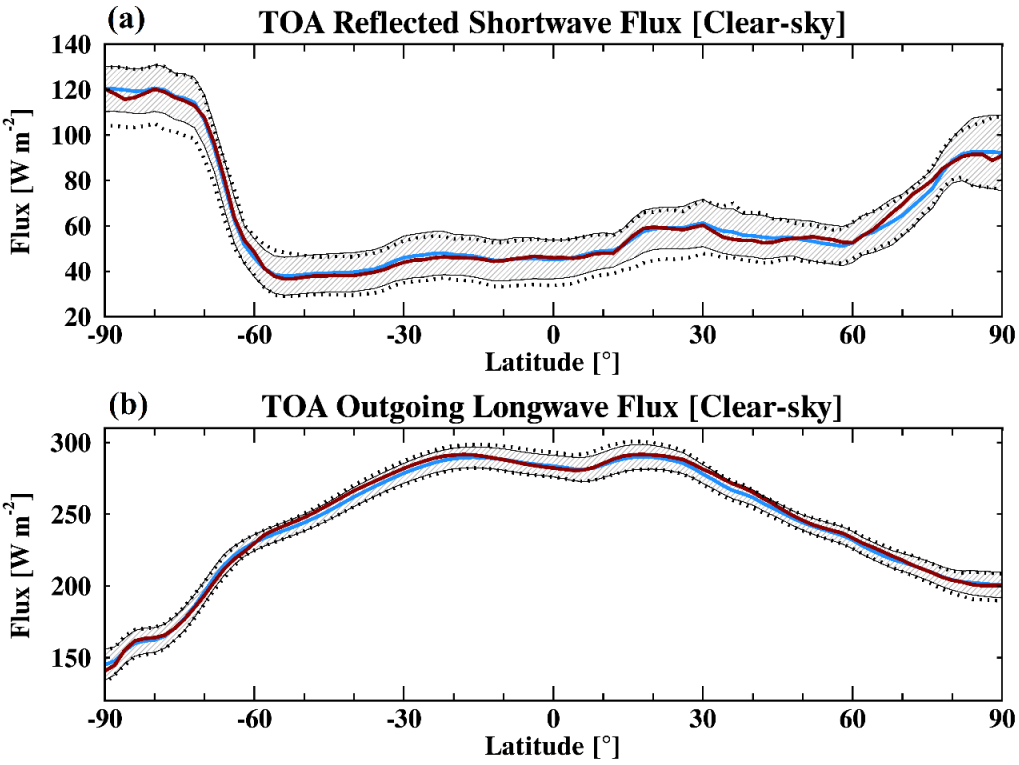

Figure 9: Same as Fig. 4 but for the zonal means of clear-sky TOA (a) reflected SW and (b) outgoing LW flux (W m^{-2}). The observed clear-sky TOA radiative fluxes (red) are from CERES EBAF.

The observed and multimodel mean clear-sky LW fluxes follow the same zonal pattern and are primarily controlled by the surface emitted temperature. The TOA outgoing LW flux is largest in the tropics and smallest near the poles, with the southern pole flux being less than the northern pole by about 50 Wm^{-2}.

Global maps of the observed and multimodel mean simulated TOA clear-sky fluxes are presented in Fig. 10. The SW clear-sky flux (left panels) is governed by the land-sea contrast, with higher flux values over land due to the higher surface albedos. The overall distribution is simulated well by the multimodel mean over the ocean (bias $\leq$ 4.0 Wm^{-2}),

yet still, there are a few regions where the GCMs and reanalyses tend to show difficulties in simulating the TOA clear-sky SW radiation flux, especially over land. The Sahara Desert, the Arabian Peninsula, the East Indies, and parts of Northern North America have a relatively large negative bias in the clear-sky SW flux at the TOA (bias up to −16 Wm^{-2}). Conversely, areas such as the Tibetan Plateau and Australia are even more over predicted (bias ≥ 20 Wm^{-2}).

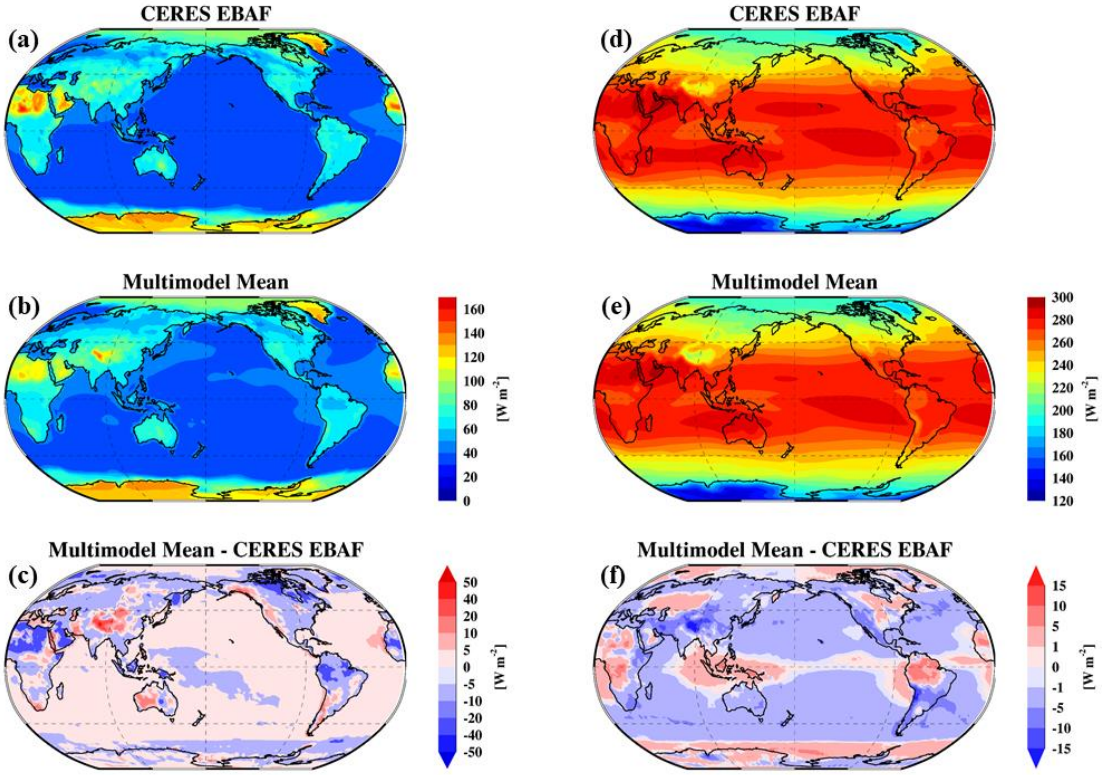

Figure 10: Global maps of the (a,d) CERES EBAF observed and (b,e) multimodel mean simulated clear-sky TOA (left) reflected SW and (right) outgoing LW fluxes (W m^{-2}). (c,f) Global maps of their differences (model minus CERES EBAF) are also depicted.

A stratification of the clear-sky LW flux is apparent from CERES EBAF (Fig. 10d) and in the multimodel mean, with larger fluxes in the tropics and decreases toward the

poles. Again, the TOA clear-sky LW is mainly a result of surface emitted temperatures (and water vapor), so we can expect this result. Oceanic regions are consistently under predicted, with an exception in the Southern Ocean around Antarctica where the LW flux is over estimated. There is a dipole in the bias over South America; the clear-sky LW flux is overpredicted in the north and underpredicted in the south, presumably due to different land surfaces and land-uses (i.e. rainforest in the North and primarily agriculture and farming in the South). The clear-sky LW flux is overpredicted in the East Indies and surrounding oceans while an underpredition is determined in the Tibetan Plateau area. These regions with large biases in clear-sky TOA fluxes could be a result of the climatologically prescribed SST and sea-ice observations used in the GCMs. However, large biases in the reanalyzed clear-sky fluxes should be of interest to model developers (e.g., LW flux in JRA-25) and effort should be made to better represent surface characteristics in their models.

TOA all-sky fluxes. Figures 11a and 11b show the model simulated and CERES EBAF observed global mean TOA all-sky SW and LW fluxes, with averaged differences of 1.6 ± 3.0 and -0.9 ± 2.9 Wm^{-2}, respectively. Although the differences between the ensemble means and observations are small, a few model results are not physically consistent. The TOA radiative fluxes, in particular the reflected SW flux, depend primarily on CF and CWP. A good agreement in the TOA reflected SW flux should be consistent with good agreements in CF and CWP (e.g. CanAM4), or complementary between CF and CWP, such as lower (higher) CF and larger (smaller) CWP (e.g. BCC-CSM1.1(m), BNU-

ESM, GISS-E2-R, or NorESM1-M), to achieve radiative balance. However, it does not make sense, physically, if the good agreement in reflected SW flux follows the same bias in both CF and CWP, as illustrated in the simulations of ACCESS1.0, GFDL-HIRAM-CM3, IPSL-CM5A-MR, and MPI-ESM-MR. The simulated all-sky reflected SW flux has a negative correlation with OLR, which is self-consistent.

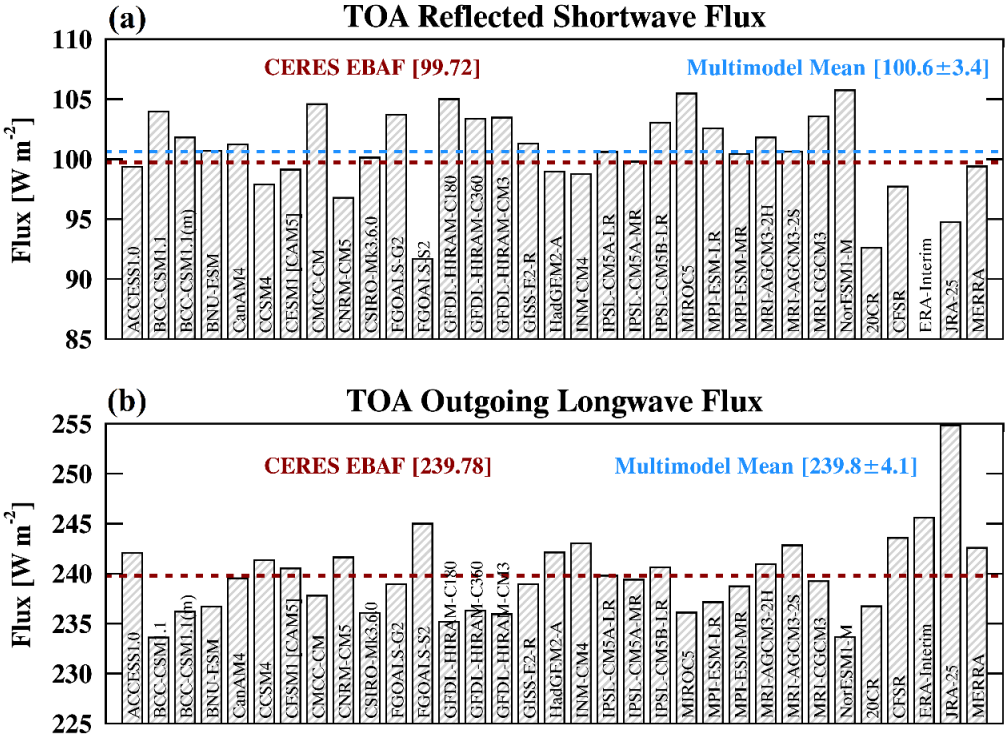

Figure 11: Same as Fig. 3 but for the all-sky top-of-atmosphere (TOA) (a) reflected shortwave (SW) and (b) outgoing longwave (LW) fluxes (W m^{-2}). The observed all-sky TOA radiative fluxes (red) come from CERES EBAF.

The zonal mean TOA all-sky radiation flux comparisons in Fig. 12 are much better than their CF and CWP counterparts (Figure 3). Both the reflected SW and outgoing LW flux multimodel means converge to the CERES EBAF observations through most latitudes;

there is an exception for the SW flux simulations near the tropics (~ 25 °S – 25 °N) and the southern latitudes near 60 °S, where CWP is similarly biased. The zonal variation of both modeled and observed all-sky reflected SW fluxes generally follow the same zonal pattern as CF and CWP with relatively large disparity over the southern mid- latitude ocean. Simulated reflected SW and outgoing LW fluxes and their corresponding ensemble means fluctuate around the observations.

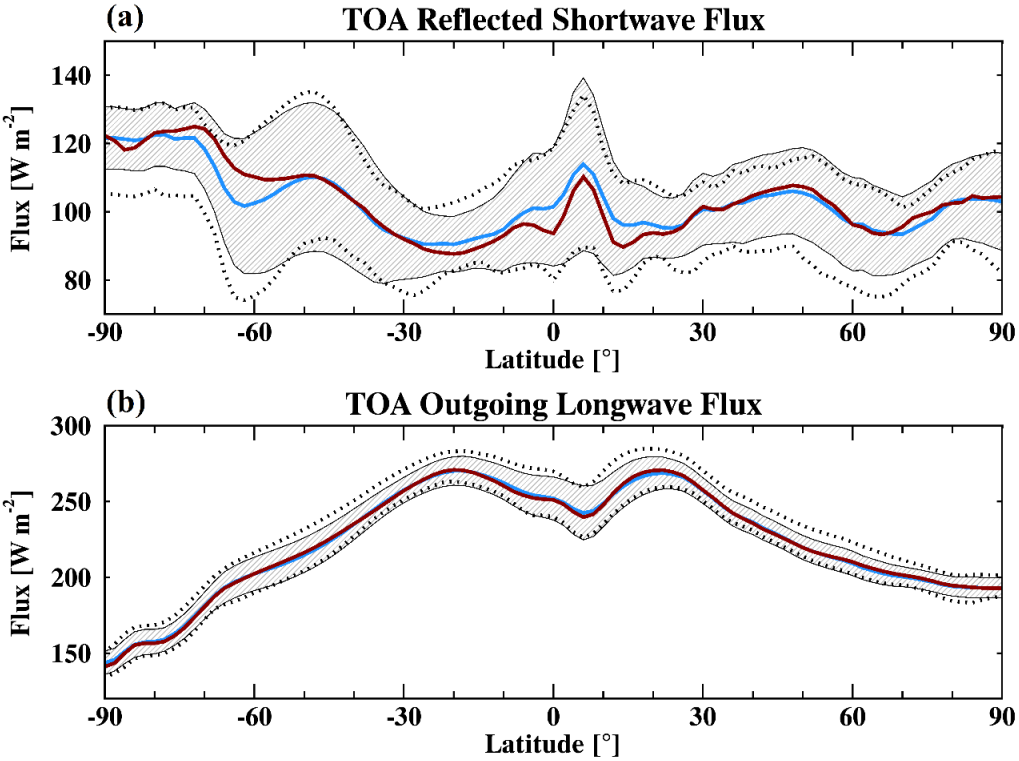

Figure 12: Same as Fig. 4 but for the zonal means of all-sky TOA (a) reflected SW and (b) outgoing LW flux (W m^{-2}). The observed all-sky TOA radiative fluxes (red) are from CERES EBAF.

As expected, the multimodel mean TOA outgoing LW flux agrees better with CERES EBAF than the SW fluxes, as the SW flux is strongly CF and CWP dependent. A

well replicated TOA outgoing LW flux suggests the multimodel mean is adequately simulating cloud-top heights/-temperatures. The peak in TOA reflected SW flux and the corresponding dip in outgoing LW radiation, as well as relatively large variations in the model simulations near 5–10 °N, are expected due to the frequent occurrence of deep convective clouds in that region.

The observed and multimodel mean simulated global distributions of the TOA all-sky SW and LW radiation fluxes are shown in Fig. 13. These global maps support the argument of consistent regional biases apparent in the model simulations. More distinct atmospheric features are evident in these results, when compared to the clear-sky results, such as the ITCZ and large-scale circulations (e.g. Hadley Cell). Consistent with the CWP results, the multimodel mean overpredicts the all-sky SW radiation in the East Indies, as well as, in the Indian Ocean by more than 16 Wm^{-2} (Figure 13c). Relatively large negative biases are less numerous but do appear, such as the South American Pacific Coast where MBL clouds persist and Southeastern China. The TOA SW flux in the Southern Ocean is also slightly under predicted, which is a common feature identified in global models. The all-sky outgoing LW flux (Figure 13d) is greatest in the tropics and in areas of persistent high-pressure (i.e. Northern Africa/Arabian Peninsula and the Eastern Pacific). In terms of the LW flux biases (Figure 13f), the largest biases occur in the tropics, notably in the Central Pacific and the Eastern Indian Ocean while large positive biases occur in the western Indian Ocean, Northern South America, and Central Africa.

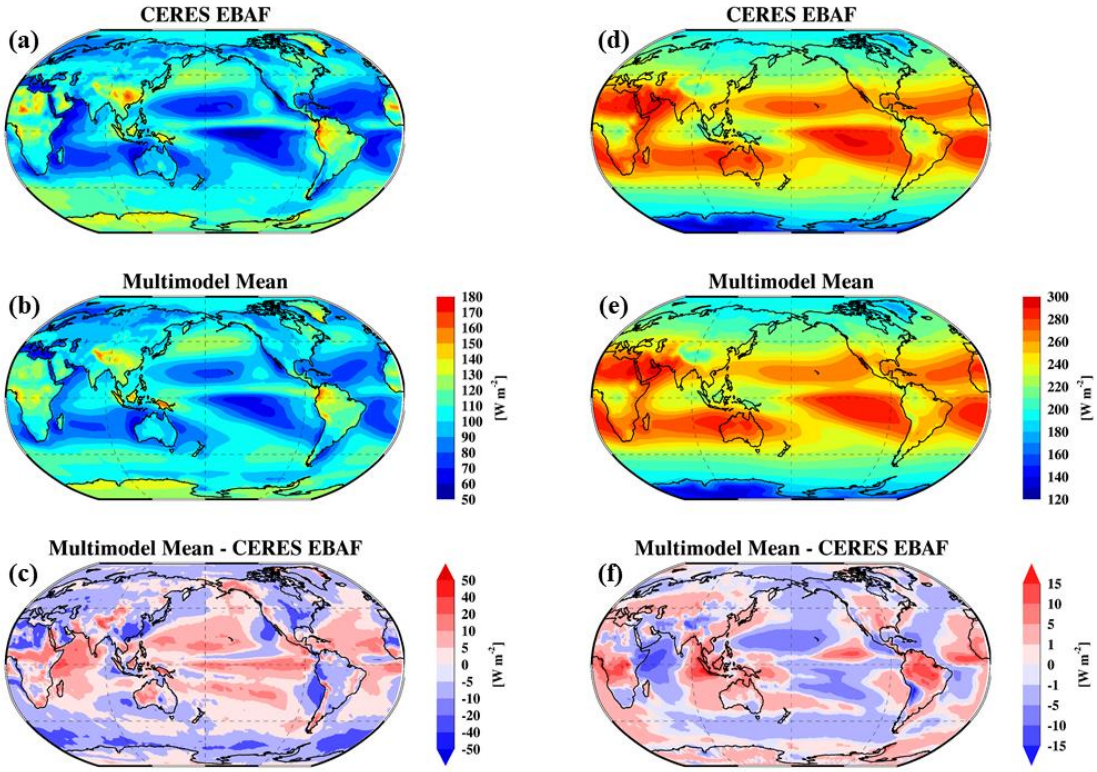

Figure 13: Same as Fig. 10 but for the TOA all-sky fluxes.

TOA Cloud Radiative Effects (CREs). The SW and LW CREs are defined by the difference in the upward and downward radiative fluxes (F) between cloudy and clear-sky conditions (*Ramanathan et al.* 1989):

$$CRE_{SW,LW}\ (Wm^{-2}) = \left[F_{SW,LW}\downarrow - F_{SW,LW}\uparrow\right]_{cloudy} - \left[F_{SW,LW}\downarrow - F_{SW,LW}\uparrow\right]_{clear} \quad (1)$$

$$CRE_{net} = CRE_{SW} + CRE_{LW} \quad (2)$$

Since the TOA $F_{LW}\downarrow$ is zero and $F_{SW}\downarrow$ is the same regardless of cloud cover, the TOA CREs can be simplified as

$$CRE_{SW,LW}\ (Wm^{-2}) = \left[F_{SW,LW}\uparrow\right]_{clear} - \left[F_{SW,LW}\uparrow\right]_{cloudy} \quad (3)$$

As shown in Fig. 14, the globally averaged SW, LW, and net (SW + LW) CREs from CERES EBAF are –47.17, 26.21, and –20.96 W m^{-2}, respectively, indicating a net cooling effect of clouds on the TOA radiation budget. The differences in SW and LW CREs between observations and multimodel means are only 0.73 and –2.01 W m^{-2}, respectively, resulting in a larger net cooling effect of –2.44 Wm^{-2}, which is consistent with Wang and Su (2013). Note that the SW and LW CRE differences include their clear-sky SW and LW (0.35 and –1.79 Wm^{-2}, respectively) biases. However, the CRE biases in some models can amount to 10 Wm^{-2}. Such biases are apparent in the simulated SW CREs in BCCCSM1.1 and NorESM1-M, the LW CRF in FGOALS-S1, GISS-E2-R, Era-Interim, and JRA-25, and the net CREs in CSIRO-Mk3.6.0 and FGOALS-S2. Therefore, a further investigation of these individual models is warranted.

The zonal variations of SW and LW CREs in Figs. 15a and 15b seemingly mimic their corresponding all-sky SW and LW flux variations in Figs. 12a and 12b. The strong SW cooling and LW warming effects between 5 °N and 10 °N are primarily contributed by deep convective clouds where the cloud albedo is nearly 0.7 and cloud-top height and temperature are ~10 km and ~220 K, respectively (*Dong et al*. 2008b). Over the southern mid-latitude ocean, MBL clouds are dominant (*Stanfield et al.* 2014), which can attribute to strong SW cooling and moderate LW warming effects. With the magnitude of SW cooling dominating over the LW warming, the zonal variation of the net CRE more closely resembles that of the SW CRE with an overall cooling effect, but to a lesser degree. The strong SW cooling and LW warming effects over these two regions motivated a further

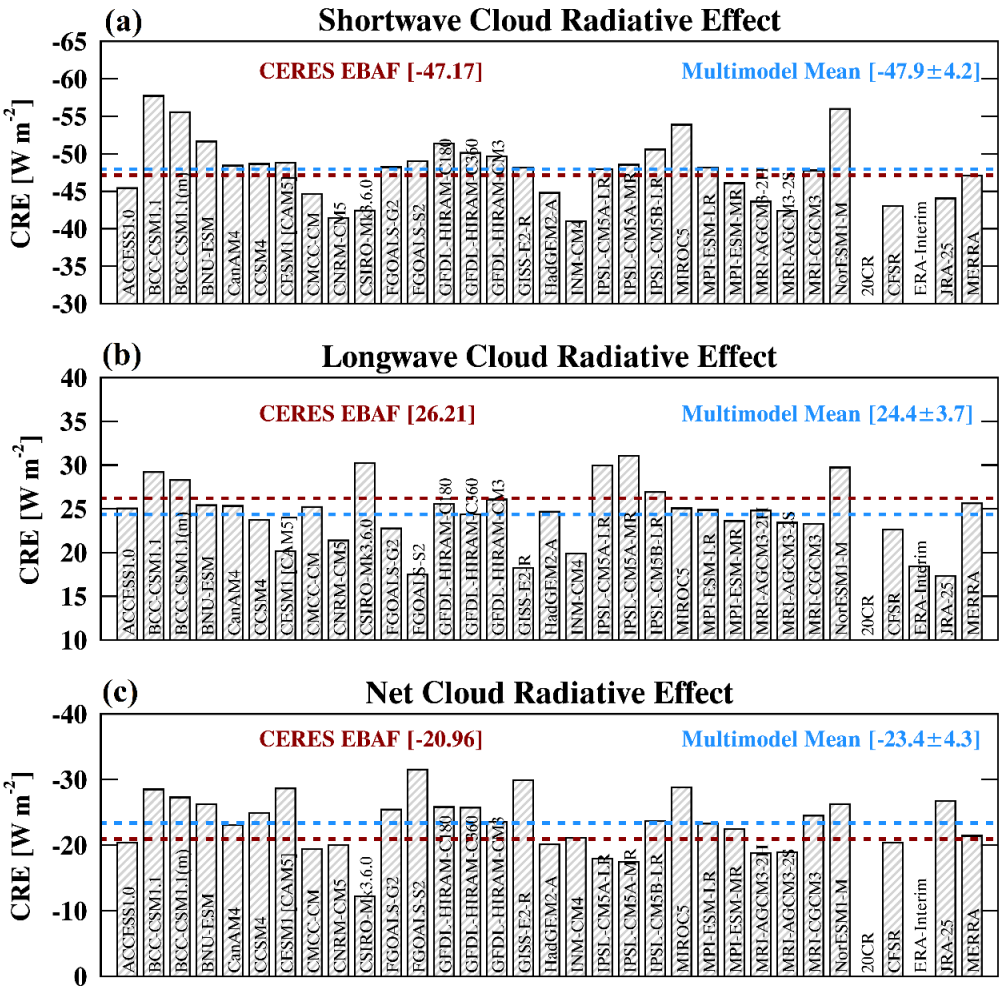

Figure 14: Same as Fig. 8 but for the TOA (a) SW, (b) LW, and (c) net cloud radiative effects (CREs; W m^{-2}).

investigation into whether clouds and CREs associate well with atmospheric vertical motions. Note than deep convective clouds are associated with upward motion, while MBL clouds are common in areas of strong sinking motion.

The global horizontal distribution of TOA CREs can be found in Fig. 16. The largest SW (LW) cooling (warming) occurs in the Western Pacific near the East Indies and

Northern South America (Figure 16a and 16d). The net cloud radiative cooling is maximized in the Eastern and Northern Pacific and in the Southern Ocean (Figure 16g).

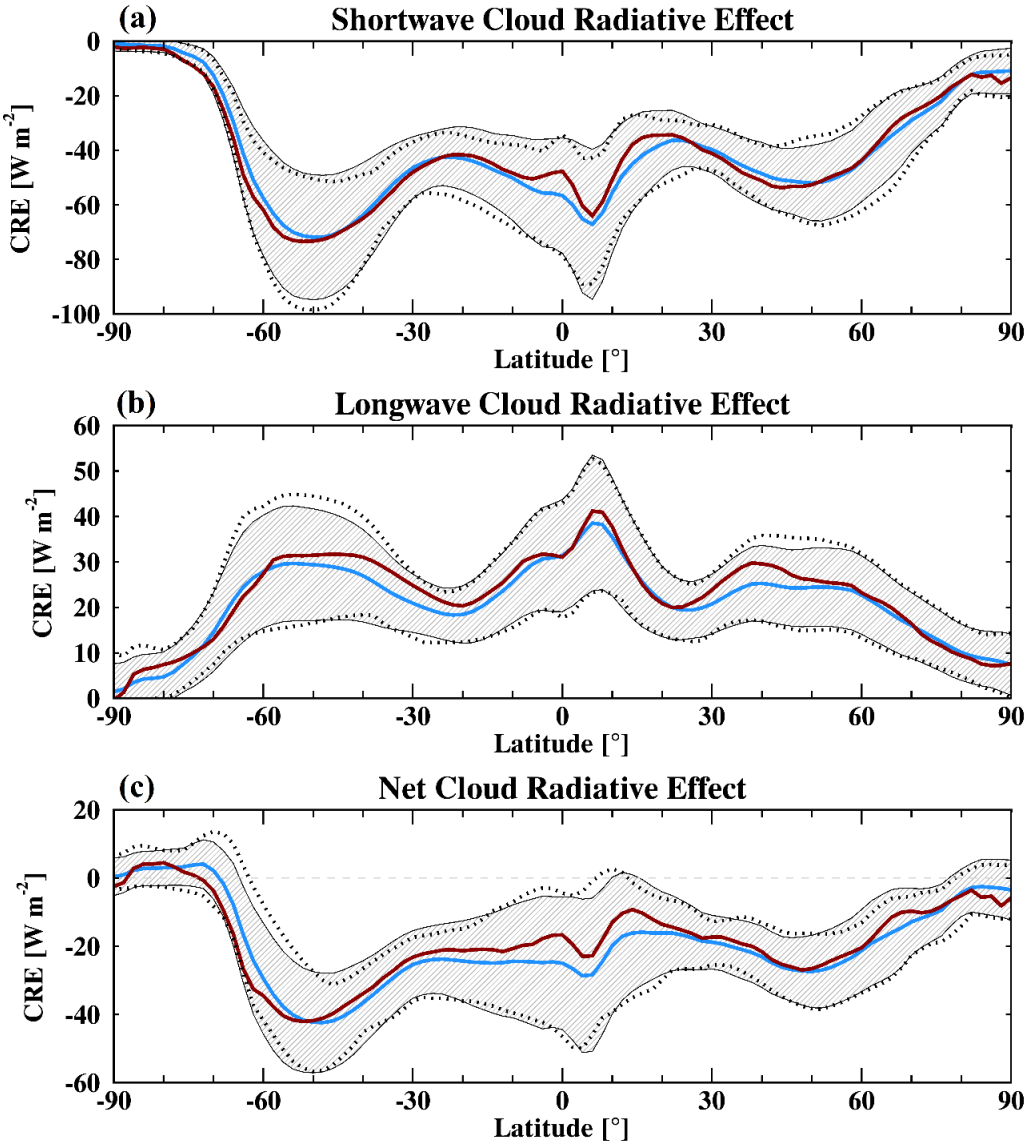

Figure 15: Same as Fig. 9 but for the TOA (a) SW, (b) LW, and (c) net CREs (W m^{-2}).

The biases in the net CRE are interpreted in terms of the magnitude of cooling or warming; positive values indicate a weaker cooling effect while negative values represent

stronger cooling effect in the multimodel mean. Again, we identify areas of persistent model deficiencies in simulating the appropriate impact of clouds on the TOA radiation budget. The multimodel mean net CRE cooling is larger than the observations by more than 10 Wm^{-2} in the East Indies, Central Africa, and in Northern South America. On the other hand, the net CRE cooling is weaker in the multimodel mean in the Southern Ocean, Southeastern China, and the Western Coast of South America and Southern California where MBL clouds frequently occur.

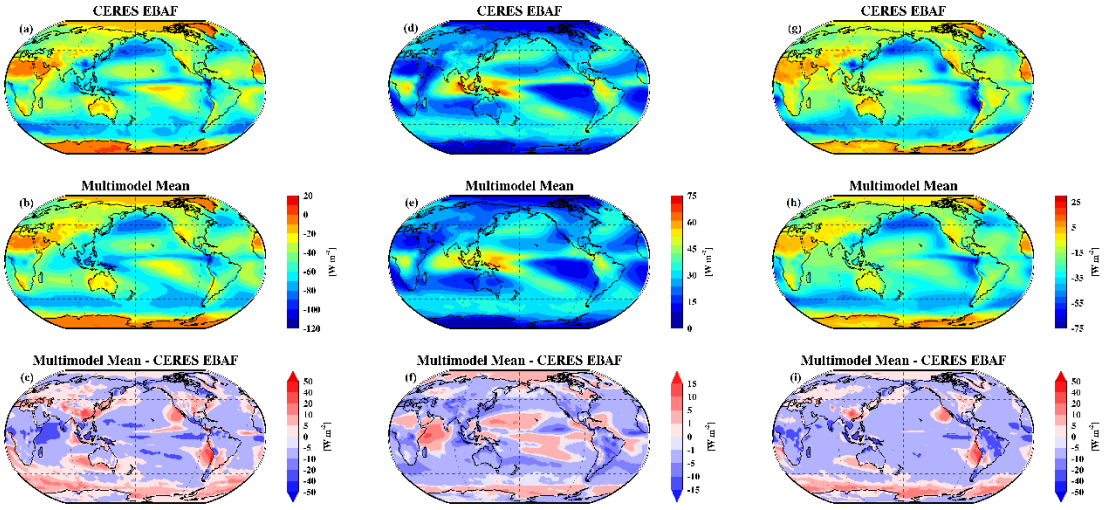

Figure 16: Same as Fig. 10 but for the TOA (a-c) SW, (d-f) LW, and (g-i) net CREs (W m^{-2}).

Table 3 offers a summary of the globally averaged observed and simulated cloud, precipitation, and TOA radiation results. Several regions have been identified to show persistent model deficiencies and should be paid close attention by modelers and special interest groups. The next step is to interrelate these biases and to develop a systematic

approach for correlating and quantifying the biases in CRE in specific regions tied to large-scale atmospheric vertical motions.

Table 3: A summary of the global means in CF (%), CWP (g m^{-2}), TOA radiation budgets and CREs (W m^{-2}), and PR (mm day^{-1}, 50 °S – 50 °N) from the multimodel mean and satellite-derived products. Values in parentheses are the standard deviations of the multimodel mean.

	Multimodel	**CERES/ MODIS/ EBAF**	**ISCCP**	**CloudSat/ CALIPSO**	**TRMM**
CF	58.9 (5.8)	65.5	65.4	75.3	-----
CWP	100.6 (36.7)	117.0	-----	-----	-----
SW [all]	100.6 (3.4)	99.7	-----	-----	-----
LW [all]	239.8 (4.1)	239.8	-----	-----	-----
SW [clear]	52.9 (3.8)	52.6	-----	-----	-----
LW [clear]	264.2 (3.2)	266.0	-----	-----	-----
SW CRE	–47.9 (4.2)	–47.2	-----	-----	-----
LW CRE	24.4 (3.7)	26.2	-----	-----	-----
Net CRE	–23.4 (4.3)	–21.0	-----	-----	-----
PR	3.34 (0.19)	-----	-----	-----	2.91

Dynamically driven regime-based analysis of clouds, precipitation, and TOA radiation budgets

Definition of atmospheric vertical motion regimes

Our analysis transitions to one developed on the premise that analyzing modeled cloud and radiation fields based on different regimes provides insight into how large-scale dynamics influences cloud-radiative properties, but also facilitates an evaluation tied to separating dynamical errors and parameterizations errors (*McFarlane et al.* 2016). Two dynamically-driven regimes are defined based on the monthly mean pressure velocity (i.e.,

vertical motion, ω) at 500 hPa (ω500) from MERRA. Areas of moderate-to-strong ascent at 500 hPa (ω500 < –25 hPa day^{-1}) over the global oceans, which are associated with the ascending branch of the Hadley Cell/Walker Circulation, are outlined in dashed lines in Fig. 17. Conversely, the areas of moderate-to-strong descending motion (ω500 > 25 hPa day^{-1}) are highlighted in dark red and outlined in solid black lines. While the areas of ascent and descent have minor, geographic changes depending on which reanalysis data are used to define them, the statistics and underlying conclusions do not change significantly.

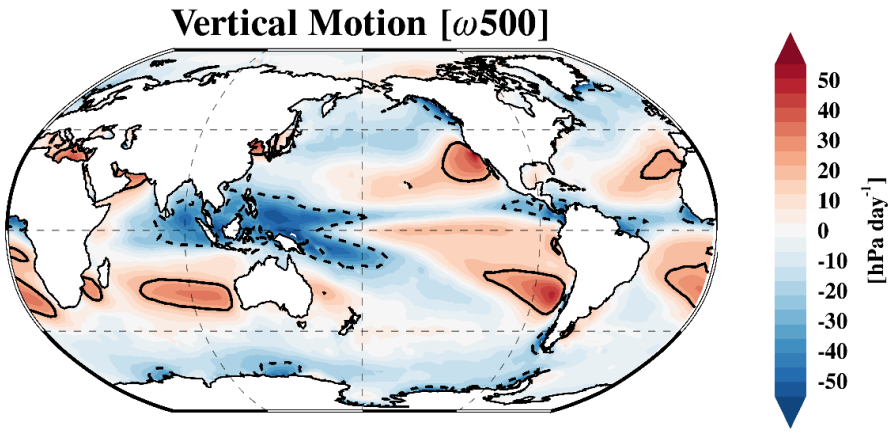

Figure 17: The global distribution of vertical motion at 500 hPa (ω500, hPa day^{-1}) over the oceans from MERRA reanalysis. Negative (positive) values represent upward (downward) motion. Solid and dashed lines highlight the areas with vertical motions greater than 25 hPa day^{-1} and less than –25 hPa day^{-1}, respectively. These outlined areas in the tropics and extra-tropics (|latitude| ≤ 45°) correspond to the ascent and descent regimes.

Convective-type clouds (e.g., cumulus, deep convection, anvil/cirrus) typically form and reside within the ascent regime while marine boundary layer stratocumulus clouds dominate areas of large-scale subsidence/descent. Therefore, the triggering of cloud parameterization schemes used to predict clouds in these areas will be different, and any

differences in the cloud-radiative biases will reflect potential shortcomings of these parameterizations. First, the observed cloud, precipitation, and radiative properties in the ascent and descent regimes will be investigated to understand the dynamical impacts.

Satellite-observed cloud, precipitation, and TOA radiation budget properties in the two regimes

The observed CFs from CERES-MODIS over the two regimes are similar (68.9% vs. 65.6%) while the CWP and TRMM PRs are larger in the ascent regime by nearly 30 g m^{-2} and 7.0 mm day^{-1}, respectively. This is not a surprising result given that deep convective clouds form in areas of moderate to strong ascent. It is also not surprising that the mean clear-sky TOA SW and LW fluxes in the two regimes are similar (SW = 39.4 vs. 38.0 W m^{-2} and LW = 280.0 vs. 283.0 W m^{-2}) as they are defined over the tropical and extra-tropical (45 °S – 45 °N) oceans where minor gradients in the surface albedo and SSTs occur; standard deviations of the regime-averaged clear-sky fluxes are less than ~5%. The all-sky TOA reflected SW flux and SW CRE are also larger (i.e., more cooling) in the ascent regime due to the relatively large CWP, while the all-sky TOA outgoing LW flux is smaller in the ascent regime (and hence stronger TOA LW warming) due to the colder cloud-top temperatures (CTT) associated with deep convection. The net TOA CRE is stronger in the descent regime, mainly due to the relatively weak LW warming that stratocumulus clouds exert. See Table 4 for a list of the observed regime-averaged cloud, precipitation, and TOA radiation properties.

Table 4: The observed regime-averaged (standard deviation, σ) cloud properties, TOA radiative fluxes and CREs, and precipitation rates. (Units: CF – %; CWP – g m^{-2}; TOA fluxes and CREs – W m^{-2}; PR – mm day^{-1}).

	Ascent	**Descent**
CF	68.9 (6.4)	65.6 (8.0)
CWP	112.7 (27.7)	83.0 (30.2)
SW [all]	104.9 (10.0)	86.8 (11.6)
LW [all]	232.6 (11.0)	267.4 (10.8)
SW [clear]	39.4 (1.6)	38.0 (1.9)
LW [clear]	280.0 (3.8)	283.8 (7.1)
SW CRE	–65.5 (10.1)	–48.8 (11.9)
LW CRE	47.4 (8.7)	16.4 (4.4)
Net CRE	–18.1 (6.8)	–32.4 (11.6)
PR	7.6 (1.9)	0.6 (0.5)

Again, while no extensive analysis is performed on the modeled PR from GCMs and reanalyses, we are still curious as to how global models perform in areas where different cloud parameterizations schemes are often triggered. Figure 18 shows the PDFs of PR from the ascent and descent regimes. Based on the TRMM result (black lines), the grid-box averaged PRs range from 0–15 (0–4) mm day^{-1} in the ascent (descent) regime. The observed PR has a roughly normal distribution centered at ~8 mm day^{-1} in the ascent regime, while the PRs in the descent regime have either a lognormal or gamma distribution with a peak near 0.15 and 0.75 mm day^{-1}. According to the mean from the five reanalyses (bars), the ascent regime PRs are also normally distributed, but the frequency of PRs at ~4–6 (~7 and ~8.5) mm day^{-1} are too few (much). The mean simulated distribution of PR in

the descent regime does not compare well with TRMM, as the frequency of PR < 0.5 mm day^{-1} is too low and too high at PR > 1.0 mm day^{-1}. On average, the PRs in the ascent (descent) regime are overpredicted in the reanalyses by 0.3±1.2 (0.4±0.3) mm day^{-1}.

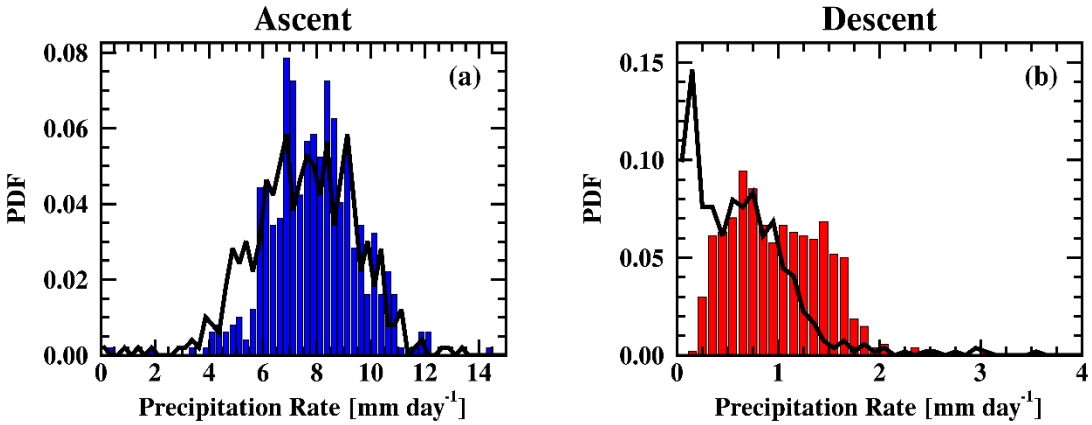

Figure 18: PDFs of the precipitation rates (PR, mm day^{-1}) averaged from four reanalyses (bars) and TRMM observations (black line) in the (a) ascent and (b) descent regimes. PRs are based on grid-box averaged values. Ascent and descent bin sizes are 0.25 and 0.10 mm day^{-1}, respectively.

Modeled regime-averaged biases in clouds and TOA radiation budgets

Global maps of the simulated multimodel mean biases in CF and CWP are once again depicted in Fig. 19 along with the ascent and descent regime-averaged biases. The multimodel mean CF and CWP are overpredicted (underpredicted) in the ascent (descent) regime by 1.1% and 14.1 g m^{-2} (17.4% and 26.2 g m^{-2}), respectively, on average. The standard deviation of this bias is larger than the actual bias in the ascent regime due to the range of positive and negative biases in this region. A summary of regime-averaged biases is available in Table 5.

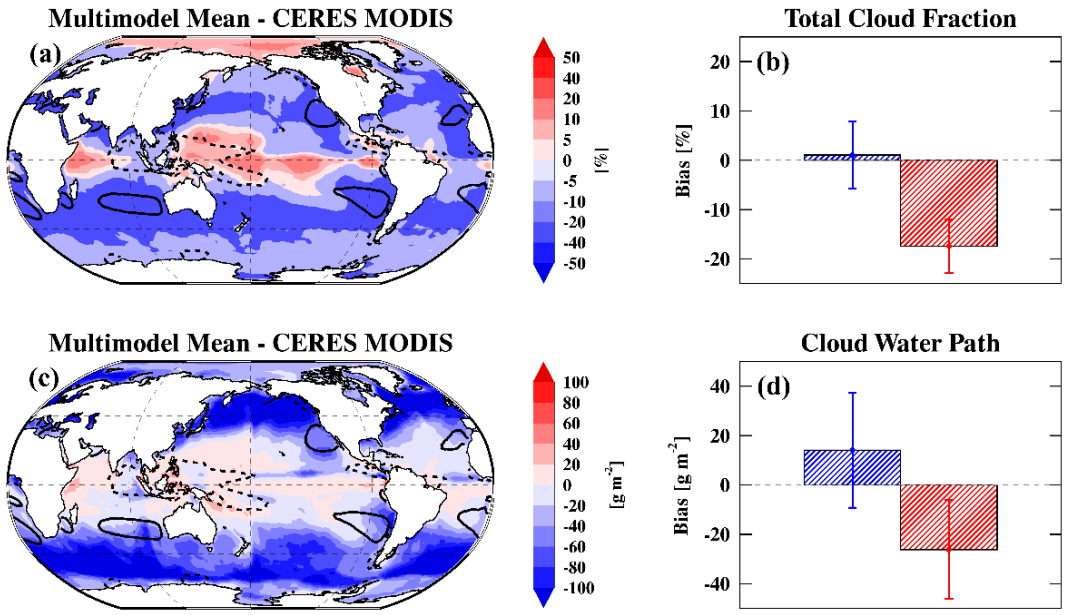

Figure 19: Global maps of the mean (model minus observation) simulated biases in (a) CF and (c) CWP compared with CERES-MODIS over the oceans. The ascent and descent regimes, defined in Fig. 17, are overlaid in dashed and solid lines, respectively. Tropical and extratropical (|latitude| < 45°) regime-averaged biases and standard deviations of (b) CF and (d) CWP are also presented in blue and red for the ascent and descent regimes, respectively.

The good agreement in CF in the ascent regime is expected because parameterized convective clouds are strongly associated with upward vertical velocity. The relatively large negative bias in CF for the descent regime suggests that a more robust parameterization for clouds in these atmospheric conditions is warranted, although a simple statistic such as this is not a perfect measure of determining which scheme requires more improvement. Kennedy et al. (2010) compared the NASA GISS single column model (SCM) simulated CF with ARM SGP radar-lidar observations from 1999–2001. They found that the SCM simulated most of the high clouds for cases with upward motion because of their strong vertical velocities and positive relative humidity (RH) bias.

However, the SCM missed some low clouds during periods of descent due to a negative RH bias associated with subsidence.

Table 5: Same as Table 4 but showing the regime-averaged multimodel mean biases and standard deviations.

	Ascent	**Descent**
CF	+1.1 (6.8)	–17.4 (5.5)
CWP	+14.1 (23.3)	–26.2 (20.0)
SW [all]	+2.0 (5.8)	–2.9 (6.4)
LW [all]	+2.3 (4.8)	+0.9 (2.0)
SW [clear]	+1.0 (1.9)	+2.3 (1.7)
LW [clear]	+0.7 (1.9)	–1.4 (1.6)
SW CRE	–1.6 (6.3)	+5.1 (6.1)
LW CRE	–1.7 (3.8)	–2.4 (1.8)
Net CRE	–3.7 (4.7)	2.8 (6.0)
PR	+0.3 (1.2)	+0.4 (0.3)

Taylor diagrams have been generated using the 1-σ spatial standard deviations and correlations to compare the 28 GCMs and five reanalyses model simulations with the CERES-MODIS/EBAF data products. Taylor diagrams are an excellent tool for displaying many simulated fields together to effectively demonstrate how well they compare to a reference value (in this case, CERES-MODIS and EBAF; *Taylor* 2001). Figure 20 shows the Taylor diagrams comparing the simulated and observed CF and CWP in the ascent and descent regimes. The simulated CF and CWP in the ascent regime (Fig. 20a and 20c) have relatively low correlations with CERES-MODIS observations ($r < \sim 0.7$) and their normalized standard deviations (model σ/ observed σ) range from 0.5–2.25, however this

range is smaller for CF (0.9–1.8). CF and CWP correlate slightly better to CERES-MODIS in the descent regime (Fig. 20b and 20d) and the range of normalized standard deviations are better (at least for CWP). Figure 20 offers a contrary conclusion to Fig. 19; based on correlation and standard deviations, the ascent regime clouds are predicted with less accuracy.

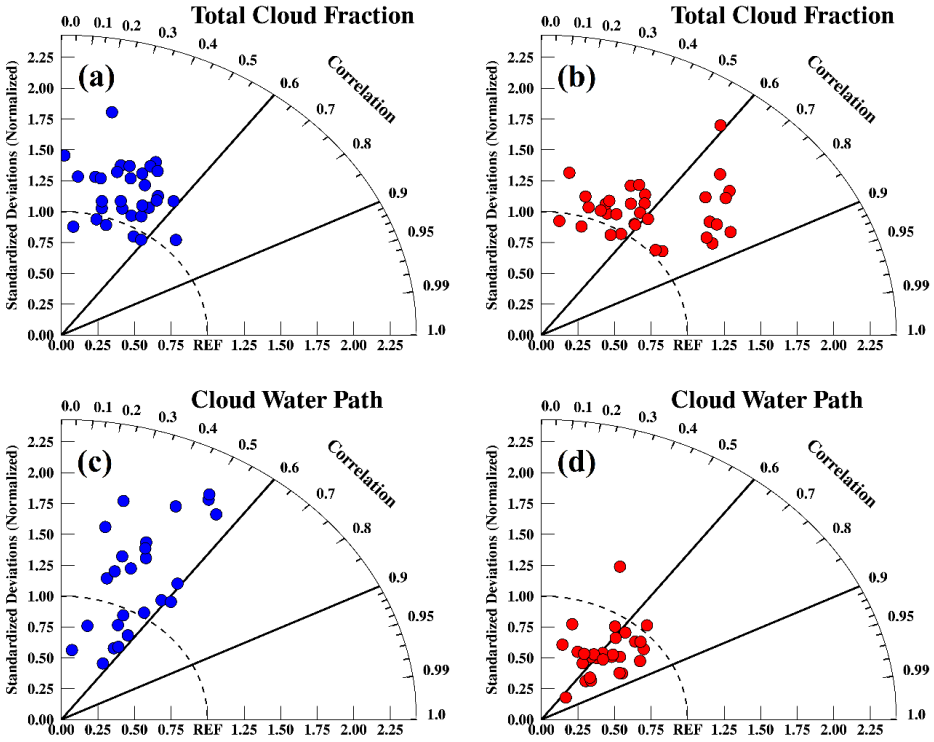

Figure 20: Taylor diagrams of the simulated (a-b) CF (%) and (c-d) CWP (g m^{-2}) within the (blue) ascent and (red) descent regimes. Each symbol represents a different model. The x- and y-axis correspond to the normalized standard deviation (model/observation) while the azimuth axis is the Pearson correlation coefficient (r) between model and CERES MODIS.

Biases in the simulated CREs (Figure 21d – 21f) are representative of their relative magnitude of warming or cooling. For example, a negative bias in the SW/net CRE

corresponds to an over estimate of cooling due to clouds. Conversely, a positive bias in the LW CRE relates to an over estimate in warming due to clouds. The multimodel mean simulated TOA all- and clear-sky fluxes are biased by less than 3.0 W m^{-2} and CREs are within ~5 W m^{-2} in both regimes (see Table 5). Biases in the simulated TOA radiation fields are mostly consistent with their CF and CWP biases. The larger CF and CWP in the ascent regime is accompanied by more SW reflection and a stronger SW CRE (more cooling). Since this analysis does not offer an investigation of the vertical distribution of clouds, we assume that the overprediction of clouds in the ascent regime is for low-level, relatively warm-topped clouds, which explains the increase in TOA outgoing LW radiation and reduction of the LW CRE. The resulting biases in the descent regime are straightforward and consistent with their biases in cloud properties. The reduction of cloud amount and CWP in the descent regime effectively reduces the reflection of SW radiation at the TOA, the outgoing LW radiation increases, and the SW/LW CREs are weaker (i.e., less SW cooling and LW warming).

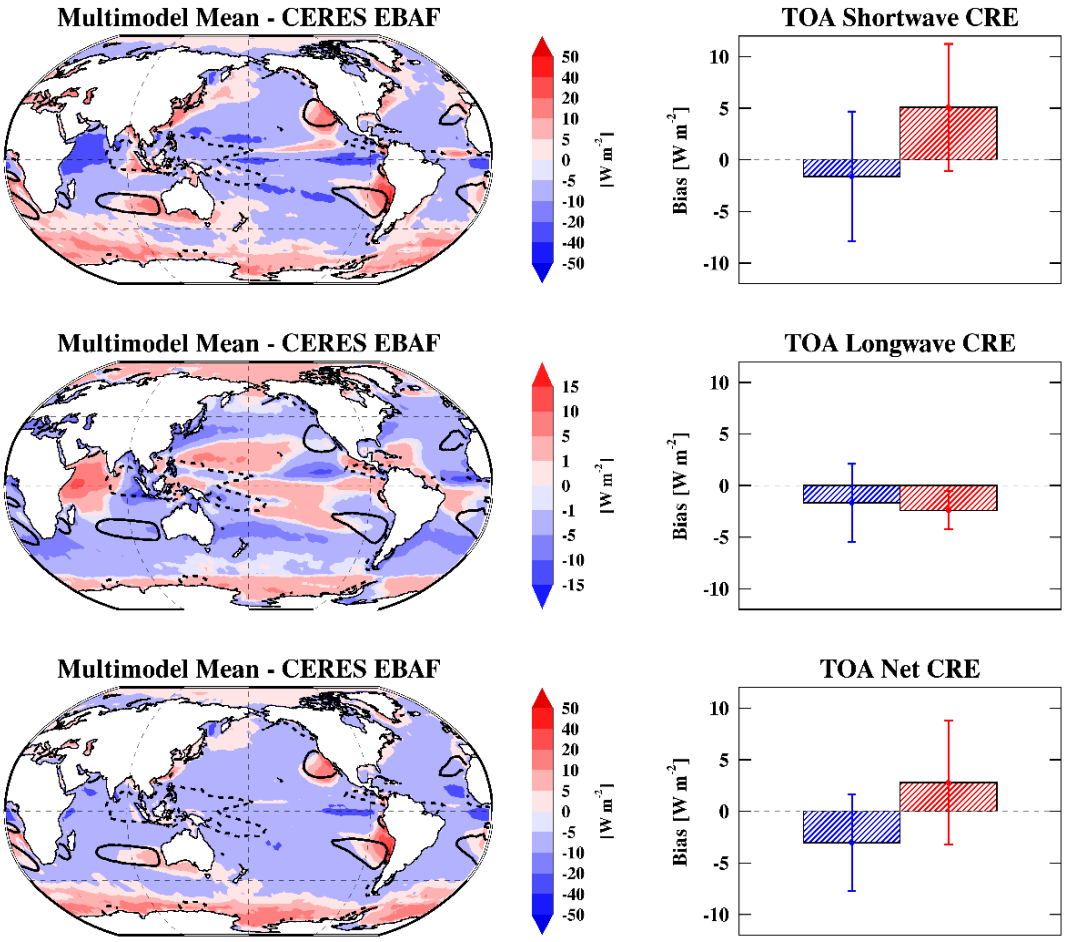

Figure 21: Same as Fig. 19 but for the simulated biases in TOA (a-b) SW, (c-d) LW, and (e-f) net CREs compared with CERES EBAF.

The results from Fig. 21 translate well to the overall score of simulated CREs (Fig. 22). In general, the correlations of modeled CREs to CERES EBAF are higher and the normalized standard deviations are better constrained than those for CF and CWP. Again, the correlations and standard deviations over the descent regime are better than those over the ascent regime. For example, most of the CRE correlations fall between 0.6 and 0.9, some even exceed 0.9, and standard deviations are near the reference point in the descent

regime. Due to the large variations in CF and CWP in the two regimes, we will investigate the sensitivities of the SW, LW, and net CREs to CF and CWP to further understand their relationships in models and observations.

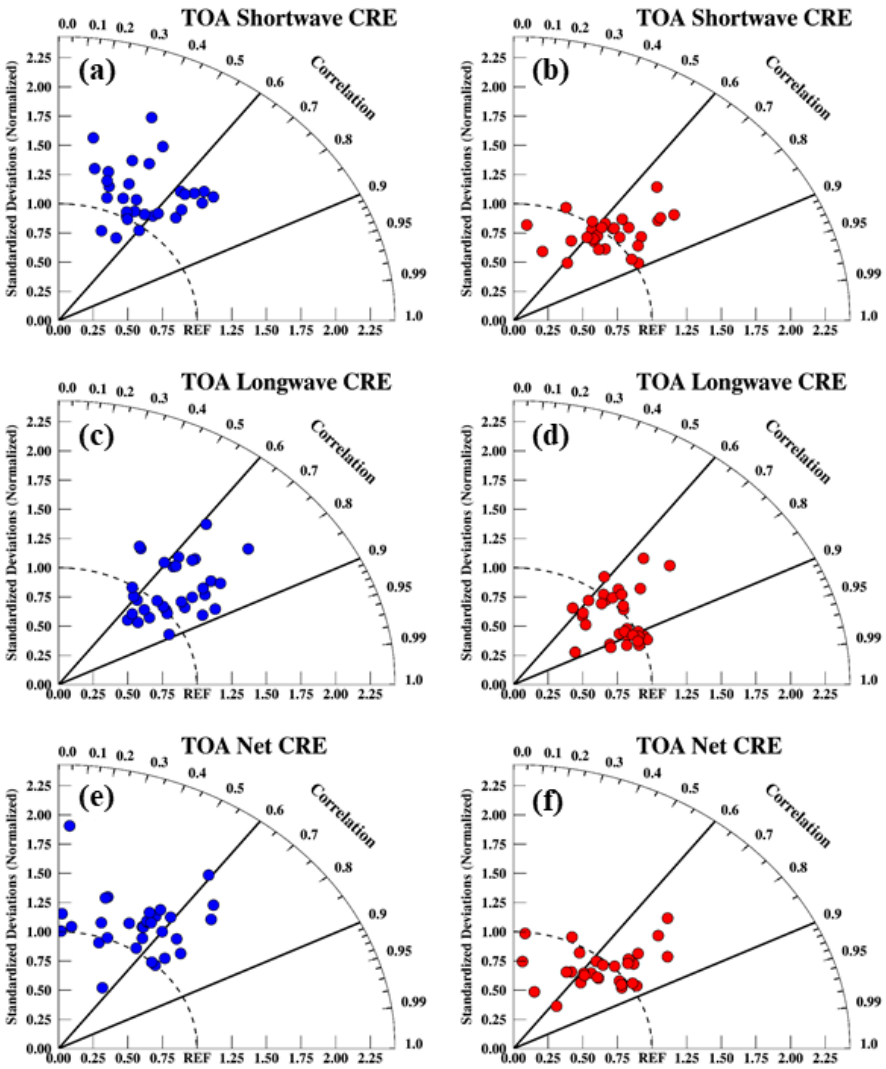

Figure 22: Same as Fig. 20 but displaying the results for the TOA (a-b) SW, (c-d) LW, and (e-f) net CREs (W m^{-2}) in comparison with CERES EBAF.

Note that the results in Fig. 20 and Fig. 22 offer contrasting conclusions as those from Fig. 19 and Fig. 21. The good agreement in the calculated mean values, but low correlation to observations in the ascent regime can be explained. MBL clouds are persistent in the descent regime, while for the ascent regime, there are a variety of cloud types, such as cumulus, anvil, cirrus, and mixed-phase clouds. To sufficiently resolve clouds in global models, different cloud-type parameterizations are implemented based upon ambient atmospheric conditions. When a diverse cloud field exists, cloud parameterizations will show difficulty in generating accurate simulations, especially if that cloud field is inhomogeneous. On the other hand, if a uniform cloud type is present (as in the descent regime), cloud parameterizations should replicate the atmospheric conditions more effectively and accurately.

Comparison of clouds and radiation with ground-based measurements at two ARM sites

While the ascent and descent regimes were defined with the purpose of isolating the impact of moderate-to-strong large-scale dynamical forcing on clouds and their radiative effects, and how they are parameterized in global models, the location of these regimes is quite convenient. The simulated cloud and surface radiation properties can be independently evaluated, along with the satellite-derived quantities, by ground-based sensors at two ARM sites located close in proximity to the areas defined in Fig. 17. The ARM TWP-C2 site, located on Nauru Island in the western Pacific, lies directly in the primary area of ascent, while the ARM site located in the Azores is situated in a region of

atmospheric descent. The modeled (reanalyses only) and satellite observed results are from the nearest grid point to these two sites.

Figure 23a shows the seasonal variations of CF observed from the ARM ground-based radar-lidar, retrieved from CERES MODIS, and the mean from the five reanalyses at the ARM Azores site from June 2009 to December 2010. Both seasonal variations and annual averages of CF from ARM measurements and CERES-MODIS (closest grid point) near the Azores site are nearly identical with annual averages of 70.2 and 69.6%, respectively. CFs gradually decrease through the year from ~80% in January to ~50% in September, and then rebounds (~75–80%) during the winter months. The largest differences between the ARM and CERES MODIS CFs are ~7% in February and May. The multimodel mean CF follows this seasonal variation, however, the multimodel mean CF is consistently low-biased by ~10%. The annual means from observations and the multimodel mean are listed in Table 6.

The monthly means of all-sky downward SW flux (SW_down) at the surface are primarily determined by the annual solar cycle and its associated changes in intensity and duration over the Azores, as well as cloud properties, whereas the solar transmission is mainly determined by cloud properties, such as CF and optical depth (not available for comparison in this study). For instance, the higher solar transmission should correspond to lower CF, and vice versa. Like the CF comparison, the monthly mean SW_down and SW transmission from ARM and CERES EBAF are almost the same, with annual differences

of 6.6 and 0.03 W m^{-2}, which is within the uncertainties of both ARM and CERES EBAF observations.

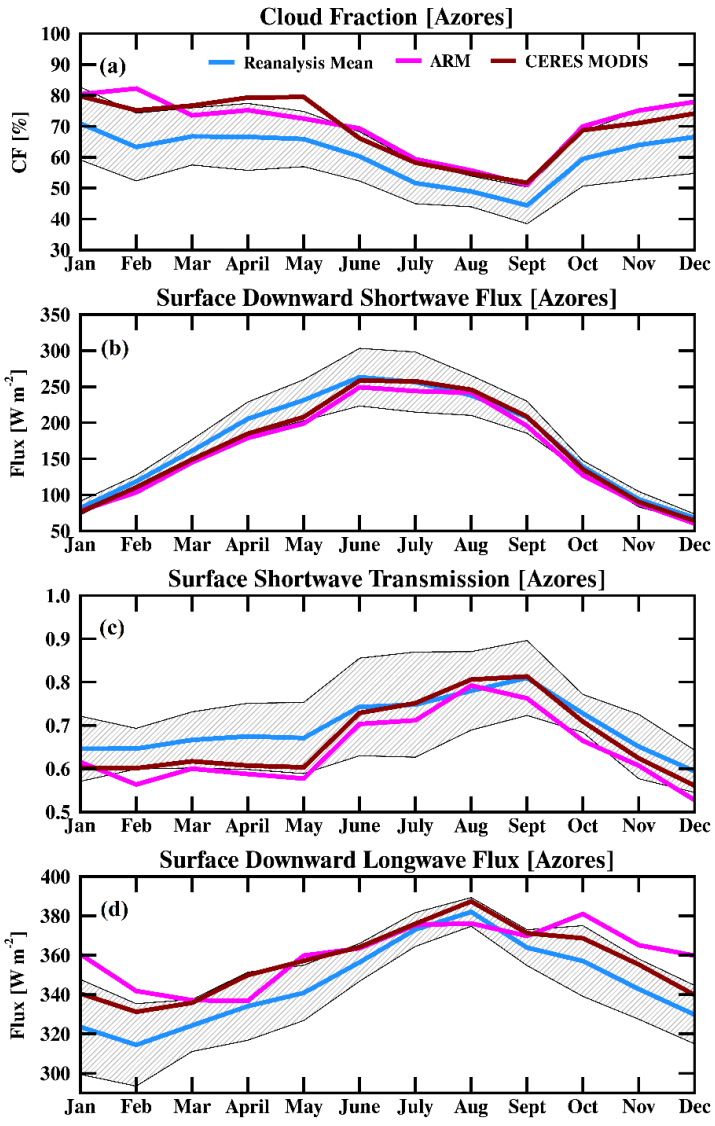

Figure 23: The seasonal variations of (a) CF, the (b) downward SW flux, (c) SW transmission, and (b) downward LW flux at the ARM Azores site from June 2009 to December 2010. Observed variations from CERES-MODIS/EBAF and ARM are in red and pink, respectively, while the modeled mean from five reanalyses are in blue. The grey shaded area is the 1σ of the modeled results.

The mean reanalyzed SW_down and SW transmission follow the seasonal variations from ARM and CERES EBAF observations and their annual mean biases are roughly 7–13 W m^{-2} and 0.3–0.6, respectively. The most significant overpredictions of surface SW_down and SW transmission occur during April and May. Assessing the bias in CF and surface SW

transmission makes physical sense at Azores, on average; the reduction of cloud amount results in an increase in SW transmission in the five reanalyses investigated here.

The downward LW (LW_down) flux at the surface depends on CF, cloud-base temperature, and atmospheric water vapor. Although the annual averages from ARM and CERES EBAF agree within 4.2 W m^{-2}, larger differences in the monthly means are found during December, January and February. Furthermore, the mean LW_down fluxes from reanalyses generally follow this pattern but underpredict the annual mean (bias = 10–15 W m^{-2}), especially during the winter months when the σ is also larger. This is an indication that there are some consistent difficulties in accurately estimating and predicting the LW_down flux from satellites and in models, respectively, during the wintertime.

Table 6: A list of the observed and modeled (reanalysis only) mean CFs (%) and surface downward SW/LW fluxes (W m^{-2}) and SW transmission (all-sky surface SW_dn/clear-sky surface SW_dn from CERES) at the ARM Azores and TWP – Nauru (C2) sites. Values in parentheses are the standard deviations of the reanalysis results.

	Reanalysis Mean	CERES/MODIS /EBAF	ARM
Azores			
CF	60.7 (8.3)	69.6	70.2
SW_dn	172.0 (17.8)	165.7	159.1
SW trans	0.70 (0.08)	0.67	0.64
LW_dn	345.2 (12.9)	356.4	360.6
Nauru			
CF	66.8 (16.4)	57.1	55.2
SW_dn	250.1 (15.3)	245.3	248.6
SW trans	0.85 (0.08)	0.83	0.84
LW_dn	417.0 (6.6)	417.6	421.7

Figure 24 shows the monthly mean CF, SW_down, SW transmission, and LW_down observed from ARM and CERES-MODIS/EBAF, and reanalyzed from the five reanalyses at the ARM Nauru site during the period between 03/2000 and 02/2009. As illustrated in Fig. 24a and listed in Table 6, the annual averages of ARM and CERES-MODIS CFs are 55.2 and 57.1%, respectively. Although the annual average difference is only 1.9%, the CF differences in some months, such as January and February, can be as large as 10%. The mean reanalyzed CF is larger than the ARM and CERES MODIS CFs (~10%), but due to the large standard deviation in the reanalysis results (16.4%), the observations fall within this range, except in January and February. Note that all observed and reanalyzed CFs are relatively constant throughout the year (annual σ = 4.0 and 6.6% in the ARM and CERES-MODIS CFs, respectively).

The seasonal variation of the SW_down flux at the Nauru site (Fig. 24b) is not as strong as at the Azores site, owning to its proximity to the equator. The ARM and CERES EBAF SW_down annual variations are maximized (minimal) in March and October (June and January) and the annual mean difference is 3.3 W m^{-2}. The reanalysis mean is within ~5 W m^{-2} and follows this pattern. The nearly constant CFs in Fig. 24a are also reflected in the surface SW transmission and LW_down annual patterns as shown in Figs. 24c and 24d, respectively. The surface SW transmission mirrors the CF variation, where the SW transmission is slightly larger during the summer and fall months when CF is relatively small.

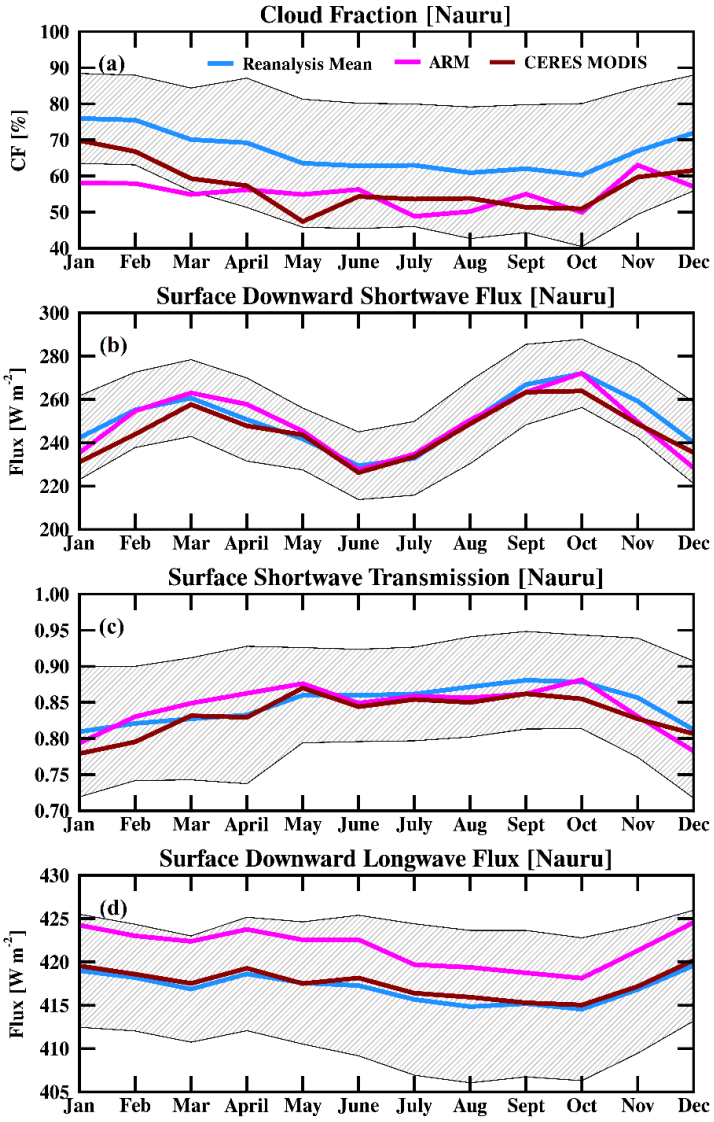

Figure 24: Same as Fig. 23 but at the ARM TWP – Nauru (C2) site for nine years of data.

A small variation in the LW_down flux at the Nauru site from both observations and reanalyses is attributed to small seasonal and diurnal variations in cloud-base temperature, SST, and water vapor at the Nauru site. All reanalyzed surface LW_down fluxes agree with observations within 5 W m^{-2}.

The observed and reanalyzed clouds and surface radiation budgets are analyzed at two ground-based sites located within distinguishable climatological regimes. The clouds that reside in these two regimes generally form by different processes and therefore have unique micro- and macro-physical cloud properties, as well as radiative effects at the surface. Compared to the properties at Nauru, the Azores annual mean CF is ~15 % higher (70.2 vs. 55.2%), less SW radiation (15–20%) is

transmitted the surface, and less LW radiation (~60 W m^{-2}) is emitted back to the surface. In addition, the magnitudes of the seasonal variations in both CF and radiation are much smaller at Nauru than at Azores.

Linear regression analysis of clouds versus TOA CREs in the two regimes

To quantitatively estimate the impacts of CF and CWP on TOA radiation budgets, the observed and multimodel mean SW, LW, and net CREs versus CF and CWP over the atmospheric ascent (blue) and descent (red) regimes are presented in Fig. 25 and Fig. 26, respectively. A best-fit linear regression is employed and used to determine the sensitivity between two variables (e.g., CF and SW CRE) in terms of the slope. To add more certainty to this analysis, the 99.5% confidence of the slope has been determined. The margin of error (M_E) in the slope is defined as

$$M_E = C_V \times S_E, \tag{4}$$

where C_V is the critical value, equal to 2.58 based on the assumption that the sample distribution is normal and large enough to be expressed by a z-score, and S_E is the standard error:

$$S_E = \sqrt{\frac{\frac{1}{n-2}\sum \varepsilon^2}{\sum (x-\bar{x})^2}}, \tag{5}$$

where ε is the linear regression residual (ε = y – mx – b) and n is the sample number. In all relationships but one, the M_E is less than the slope itself, supporting the current method for determining the sensitivity between two variables, and adds value to the analysis. In the

case of the multimodel mean simulated net CRE sensitivity to CF, the M_E (0.11 Wm^{-2} $\%^{-1}$) is greater than the characteristic slope (m = 0.06 Wm^{-2} $\%^{-1}$; see Fig. 25f).

As illustrated in Fig. 25a, the observed sensitivities of the SW CRE to CF are similar in both vertical velocity regimes. The magnitude of the SW CRE increases significantly with increasing CF. The similar sensitivities (−1.12 and −1.34 Wm^{-2} $\%^{-1}$) over these two regimes are understandable from the definition of SW CRE ($SW\uparrow_{clr}$ – $SW\uparrow_{all}$), since the albedos of deep convective and MBL clouds are both much larger than the background ocean albedo (~6 %).

Conversely, the LW CRE increases with increasing CF but is characterized by different sensitivities over the two regimes (Fig. 25b). The observed sensitivities are 0.82 and 0.23 Wm^{-2} $\%^{-1}$ over the ascent and descent regimes, respectively. The different LW CRE sensitivities between these two regions are primarily the result of CTTs of deep convective (ascent) and MBL (descent) clouds. The CTTs of deep convective clouds are rather cold (~ 220 K, *Dong et al.* 2008b), while the MBL CTTs (~280 K, *Dong et al.* 2014; *Xi et al.* 2014) are similar to the underlying SST. Based on the definition of the TOA LW CRE ($LW\uparrow_{clr}$ – $LW\uparrow_{all}$), it is straightforward to explain the higher sensitivity of the LW CRE to CF in the ascent regime. The weak sensitivity of the net CRE to CF in the ascent regime is due to the complementing effects of the SW and LW CREs.

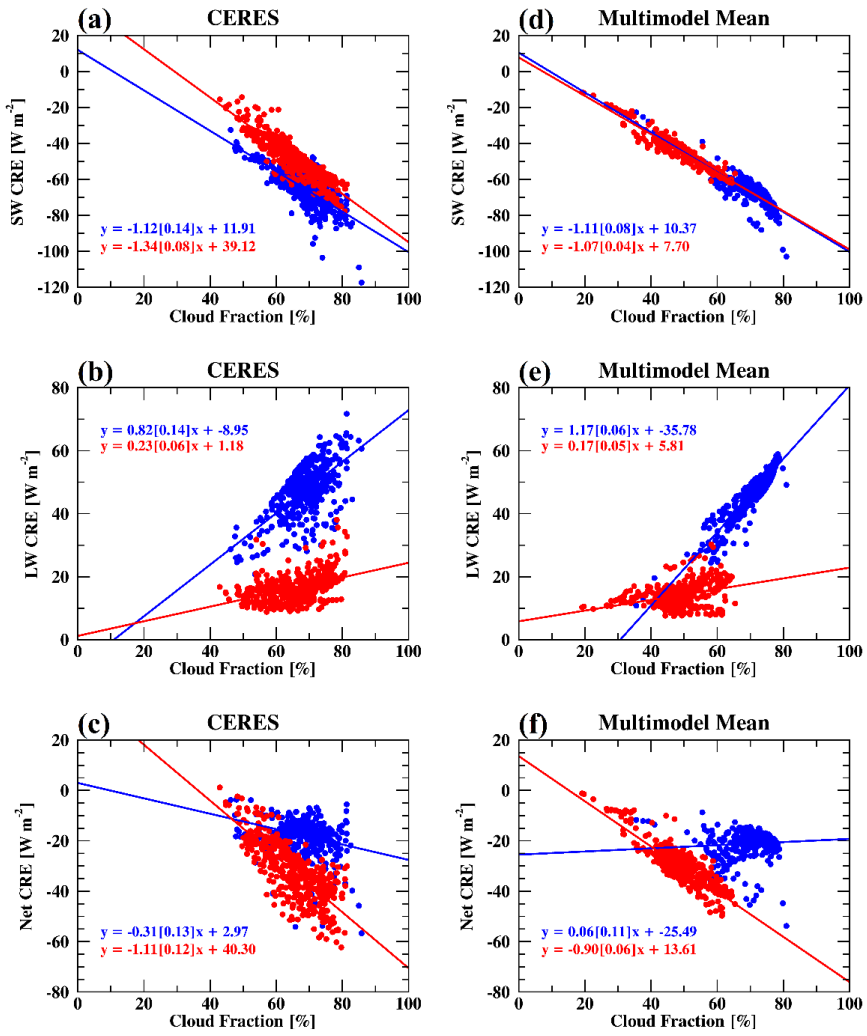

Figure 25: Scatterplots of the (a – c) observed and (d – f) multimodel mean simulated CFs versus TOA (a,d) SW, (b,e) LW, and (c,f) net CREs in the ascent (blue) and descent (red) regimes. Data are sampled from tropical and extra-tropical (|latitude| < 45°) oceans. Characteristic linear regression lines are provided where values in parentheses are the slope uncertainties (99.5% confidence) determined using Eqn. 4.

The sensitivities of the multimodel mean simulated SW, LW, and net CREs to CF (right column, Fig. 25) seemingly mimic their observed counterparts, but not without some discrepancies. For example, the sensitivities of SW CRE to CF over the ascent and descent regimes (−1.11 and −1.07 Wm^{-2} $\%^{-1}$, respectively) are nearly the same as the observed

ones. The simulated descent regime LW CRE sensitivity to CF is also similar to the observed one. However, in the ascent regime, the simulated sensitivity is 0.35 Wm^{-2} $\%^{-1}$ stronger due to the inclusion of excess water (liquid, ice, or both) within the cloud column. The nearly neutral slope of the simulated net CRE to CF in the ascent regime confirms that the model simulations effectively show a near cancelation of the SW cooling and LW warming. The conclusions in Fig. 25 (i.e. the magnitude of SW/LW CRE (cooling/warming) increases with increasing CF) affirm those within Dong et al. (2006) who investigated the DOE ARM SGP ground-based observations. The distinction between ascent and descent regimes suggests that large-scale dynamics greatly influences the cloud-radiation interactions and their predictability. In a later section we will investigate the theoretical effect of the biases in these sensitivities on the simulation of CRE.

The sensitivities of observed SW CREs to CWP in the ascent and descent regimes, shown in Fig. 26a, are identical with a slope of −0.28 Wm^{-2}/gm^{-2}. The magnitude of SW cooling increases with increasing CWP (and CF), and varies in sensitivity between these two variables. Changes in the SW albedo are strongly dependent on both CF and CWP. The multimodel mean simulated sensitivities of SW CRE to CWP are nearly the same over the two regions (–0.26 and –0.28 W m^{-2} g m^{-2}), and are similar to the observed values. The simulated LW sensitivities (Figs. 26b and 26e) are not strongly regime dependent, as in the CF results, and are not significantly different from the observations. The slope of the multimodel mean LW CRE to CWP in the ascent regime (Fig. 26e) is only 0.07 Wm^{-2}/gm^{-2} larger than in the CERES observations (and is within their combined M_E estimates).

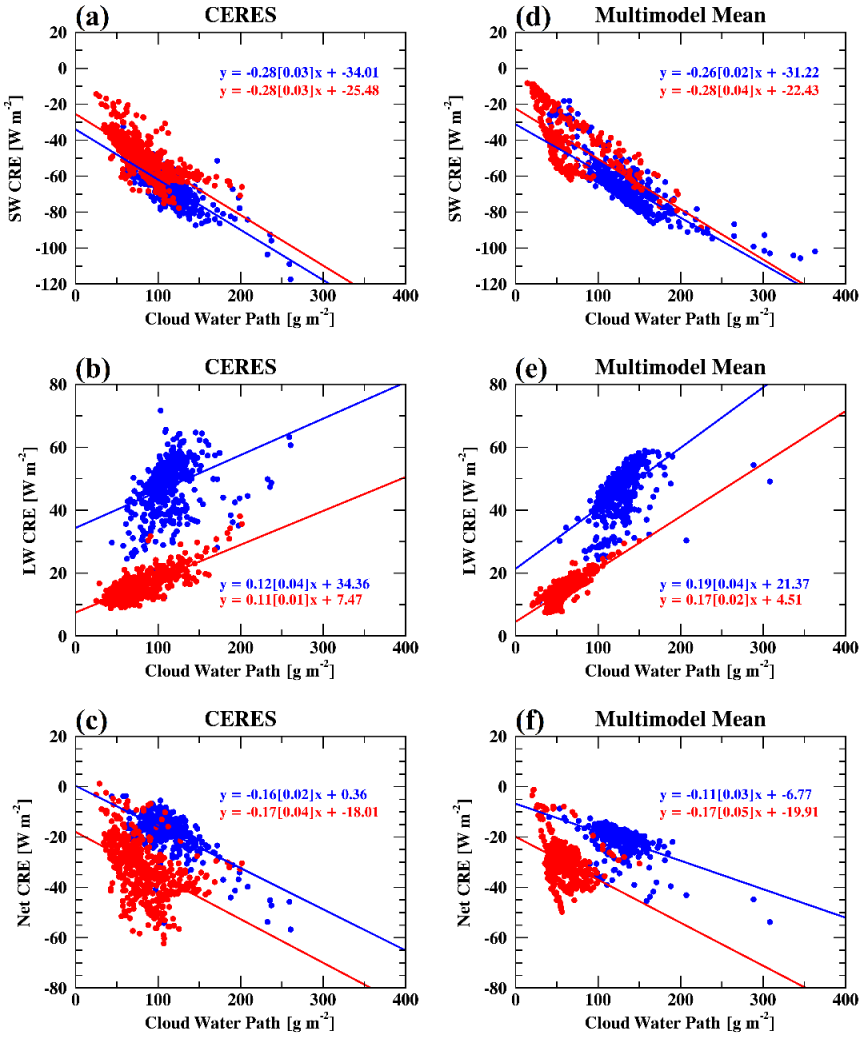

Figure 26: Same as Fig. 25 but the CREs are plotted against CWP.

Error analysis – Quantifying the sources of error

Definition of error types

The modeled CREs are assumed to be a function of CF and CWP based on the following cloud-radiative kernel:

$$CRE_{Y,m} = \left|\left(\frac{\partial CRE_Y}{\partial CF}\right)\right|_m CF_m + \left|\left(\frac{\partial CRE_Y}{\partial CWP}\right)\right|_m CWP_m \quad (6)$$

where Y is the SW, LW, or net CRE. While CREs are dependent on other model variables such as cloud droplet effective radius (R_e), CTT, precipitation, and water vapor, CF and CWP contribute most to its value. Clouds are analyzed based on their radiative properties in the ascent and descent regimes defined in Fig. 17. The sensitivities of TOA CREs to CF and CWP for each regime, as determined by their linear regression, are used as a first order approximation in place of the cloud radiative kernels (*Dolinar et al.* 2015). Therefore, the total regime-averaged error in CRE can be decomposed into the errors associated with the sensitivity of CRE to CF or CWP (i.e., Figs. 25 and 26), the regime averaged bias in CF or CWP (i.e., Fig. 19), and their co-variations,

$$\varepsilon_{total} = \varepsilon_{sens,CF} + \varepsilon_{sens,CWP} + \varepsilon_{CF} + \varepsilon_{CWP} + \varepsilon_{cov,CF} + \varepsilon_{cov,CWP} \quad (7)$$

where

$$\varepsilon_{sens,X} = \left[\left|\left(\frac{\partial CRE_Y}{\partial X}\right)\right|_m - \left|\left(\frac{\partial CRE_Y}{\partial X}\right)\right|_o\right] X_o, \quad (8)$$

$$\varepsilon_X = \left|\left(\frac{\partial CRE_Y}{\partial X}\right)\right|_o [X_m - X_o], \text{ and} \quad (9)$$

$$\varepsilon_{cov,X} = \left[\left|\left(\frac{\partial CRE_Y}{\partial X}\right)\right|_m - \left|\left(\frac{\partial CRE_Y}{\partial X}\right)\right|_o\right] [X_m - X_o] \quad (10)$$

where X = CF or CWP and the subscript o represents the observed value.

Sources of error in model simulations

The sources of error are computed based on Eqns. 8–10 for each model and are averaged in Fig. 27. Errors related to CF (CWP) are provided in the left (right) column. In the ascent regime, the bias in simulated LW CRE sensitivity to CF contributes largely to the total error in LW CRE in terms of the mean and model spread (20.4±19.4 Wm^{-2}), as

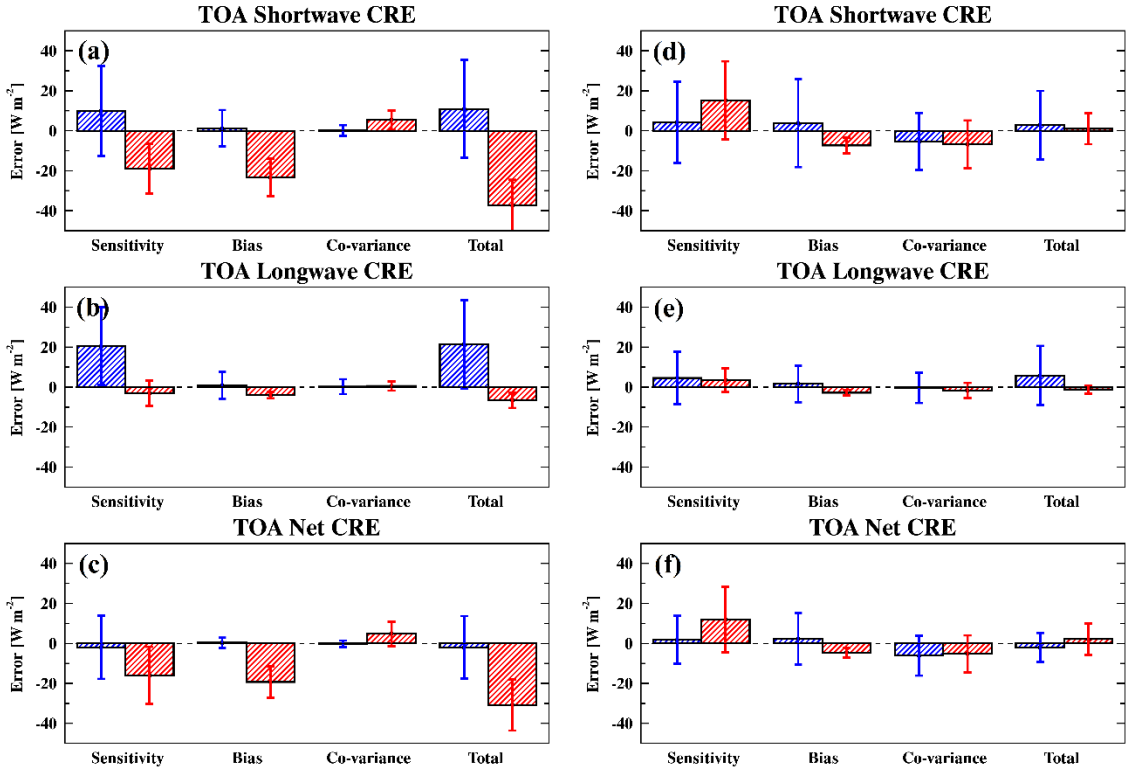

Figure 27: A summary of the (a,d) SW, (b,e) LW, and (c,f) net CRE sources of error (sensitivity, bias, co-variance, and the total; W m^{-2}) in reference to (a-c) CF and (d-f) CWP. Blue (red) bars represent the errors from within the ascent (descent) regime. Error bars are the standard deviations of each error source contributed by the range of results from the 28 CMIP5 GCMs and five reanalyses (when available).

shown in Fig. 27b. The bias in SW CRE sensitivity to CF in the ascent regime (Fig. 27a) is also rather large (9.9±22.6 W m^{-2}), however, these two errors effectively cancel each other out in the net CRE, yielding a mean total error in net CRE of –1.9±15.6 W m^{-2} in the

ascent regime. Individual errors associated with biases in the simulated CWP that contribute to errors in the CREs are all less than ~5 W m^{-2} in the ascent regime.

In the descent regime the dominate source of the error in the simulated CREs are associated with the under prediction of CF. The regime-averaged SW CRE error from the CF bias amounts to −23.3±9.5 Wm^{-2}. In addition, the errors associated with the multimodel mean SW CRE sensitivities to CF and CWP are −18.9±12.5 and 15.2±19.5 Wm^{-2}, respectively. The bias in regime-averaged CWP also contributes about −7.4±3.9 Wm^{-2} to the SW CRE error on average. Again, the biases related to the simulated CWP are generally smaller than those related to CF in the descent regime. Only through detailed error analyses such as the decomposition conducted here, are we be able to better understand the physical processes accountable for model shortcomings.

Summary of total errors

Total errors contributed by biases in the simulated CF, including the errors associated with the CRE sensitivity to CF, CF biases, and the co-variations in both vertical velocity regimes are depicted for each model in Fig. 28. For biases in the SW CRE within the descending branch of the large-scale circulation, the errors associated with CF are negative for every model, indicating a universal model disparity. This is mainly due to the under estimation of both CF and the sensitivity of SW CRE to CF. MRI-AGCM3-2S produces the largest SW CRF error by CF (−63.1 Wm^{-2}) and CFSR has the smallest (−11.6 Wm^{-2}). Conversely in the ascending branch, the SW CRE errors due to CF are positive for

a majority of the 33 models investigated here, with 10 having negative errors. GFDL-HIRAM-CM3 produces the largest error in SW CRE in the ascent regime, −47.6 Wm^{-2}, while MRI-AGCM2-2S has the smallest error of −0.9 Wm^{-2}.

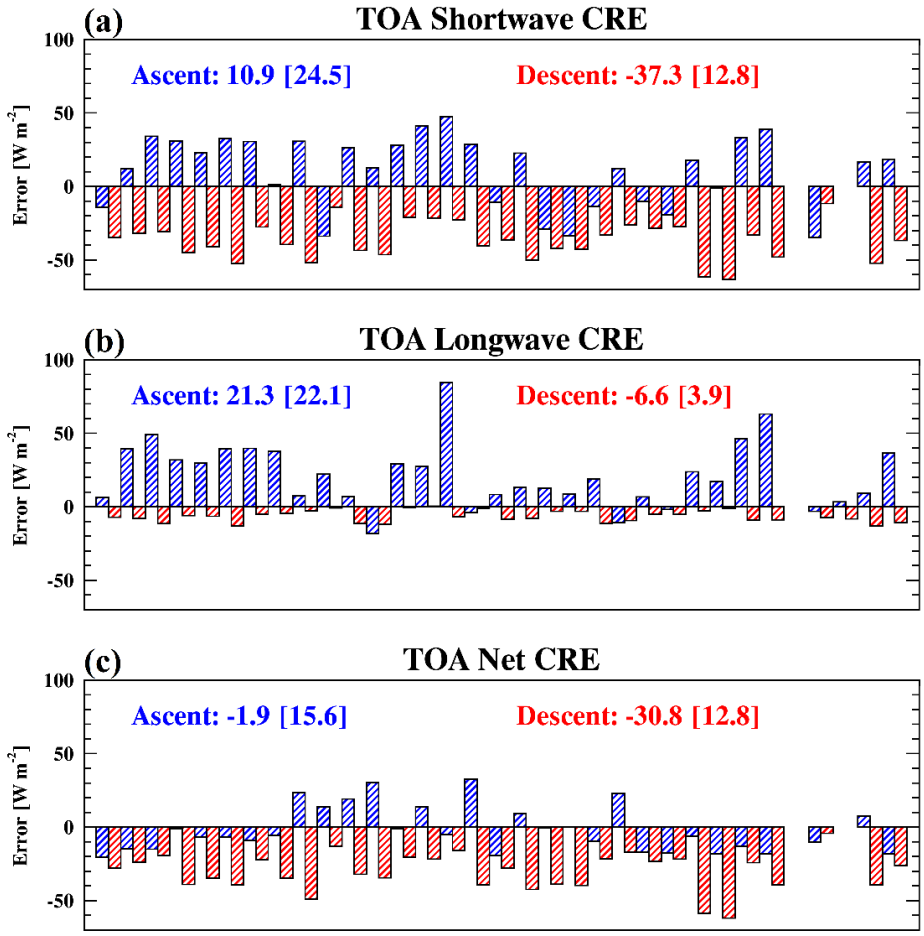

Figure 28: A summary of the total errors (W m^{-2}; using Eqn. 7) in (a) SW, (b) LW, and (c) net CRE for each model (when available) contributed by total column CF. Blue (red) bars represent the total errors within the ascent (descent) regime. The multimodel mean total errors (and standard deviation) are also listed for each regime.

The errors associated with CF in the LW CRE are predominately negative (i.e., under estimation of LW cloud warming) in the descending branch of the large-scale

circulation for all models in the 32-model ensemble (no 20CR data), except GFDL-HIRAM-C360. The largest error is from CCSM4 (−13.2 Wm^{-2}) while GFDL-HIRAM-C360 yields a LW CRE error of +0.44 W m^{-2} in the descent regime. The total ascent regime errors are mostly positive in association with CF, primarily from the over prediction of the LW CRE sensitivity to CF in the models. GFDL-HIRAM-CM3 poses the largest error (84.6 Wm^{-2}) in the estimate of LW CRE, while MPI-ESM-MR has the smallest error (−1.9 Wm^{-2}). On average, the total errors in the net CRE, caused by errors in the simulated CF, is ~16× larger in the descent regime than in the ascent counterpart.

Figure 28 is equivalent to Fig. 27; however, it summarizes the errors associated with CWP for each model. In general, the maximum and minimum errors due to CWP errors are less than those due to CF, and the inter-model spreads are within one order of magnitude of the mean.

The errors discussed above are those quantified from biases in the simulated CF and CWP (sensitivity, co-variation, etc.). However, the simulated CREs are dependent upon other processes and properties of the atmosphere that have not been considered here. Although they have not been evaluated in this study, they will surely make for a better explanation for why biases in the simulated CRE occur. Other variables, which are simulated by the GCMs and observed by satellites, that when considered and can lead to a better understanding of CRE errors include, but are not limited to, relative/specific

humidity, water vapor path, precipitation, cloud-top pressure, cloud-base height/temperature, and effective radius.

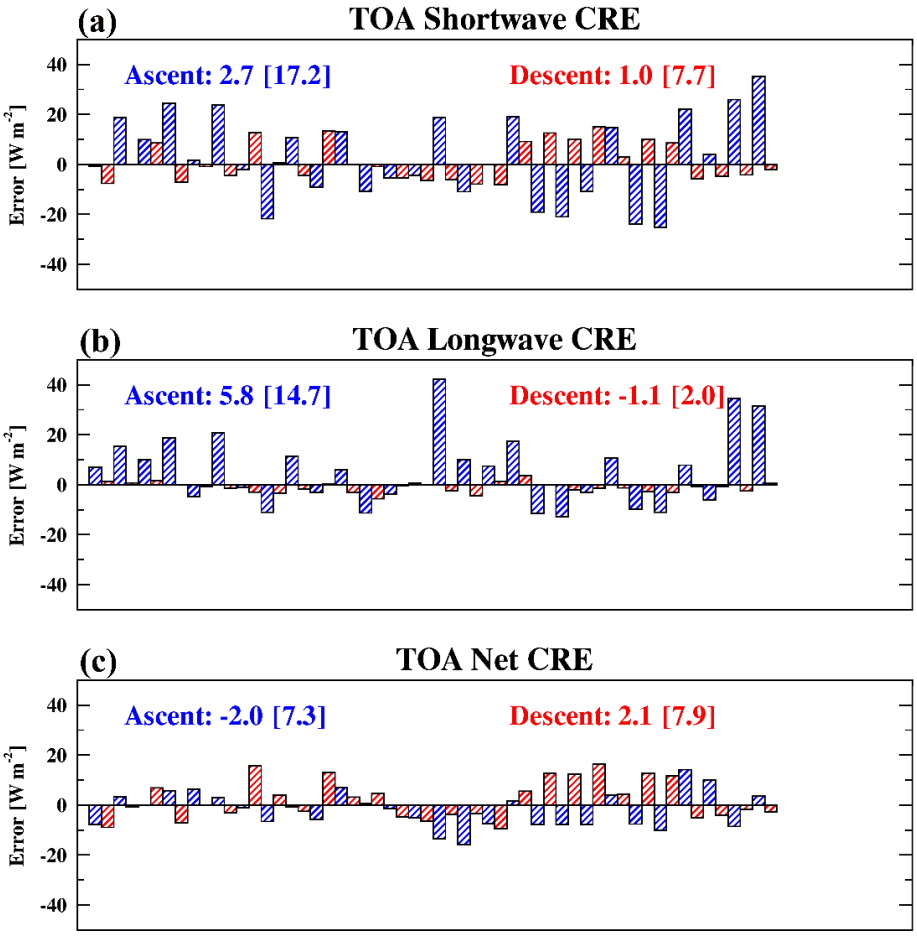

Figure 29: Same as Fig. 28 but for the total errors contributed by CWP.

Summary of Chapter III

The globally simulated CF, CWP, TOA radiation budgets and CREs from 28 CMIP5 models and five contemporary reanalyses are evaluated and compared with satellite observations (CERES/MODIS/ISCCP/CloudSat/CALIPSO) for multiple years of data. The model biases are identified and quantified to encourage model improvement in the future. Based on this analysis, we can make the following conclusions.

1) The modeled CFs are, on average, underestimated by 7% when compared to CERES-MODIS and ISCCP results (passive sensors) with an even larger negative bias (16%) compared to CloudSat and CALIPSO (active sensors). The multimodel mean CF agrees well with the CERES MODIS and ISCCP CFs in the tropics (5 °S – 15 °N), but then diverge poleward, with a large discrepancy in the Southern Ocean. The CWP comparison is similar to the results in CF with a negative bias of 17 gm^{-2} compared to CERES MODIS. The model simulated and CERES EBAF observed TOA reflected SW and outgoing LW fluxes, on average, differ by 0.9 and 0.02 Wm^{-2}, respectively. The simulated clear-sky fluxes match well with CERES EBAF too (biases are < 2.0 W m^{-2}).
2) The nearly global averaged SW, LW, and net CREs from CERES EBAF are –47.2, 26.2, and –21.0 Wm^{-2}, respectively, indicating a net cooling effect of clouds at the TOA. The differences in SW and LW CREs between CERES EBAF and the multimodel mean are –0.7 and –1.8 Wm^{-2}, respectively, resulting in a larger net

cooling effect of ~2.3 Wm^{-2} in the model simulations. The strong SW cooling and maximum LW warming effects from 5–10 °N are primarily contributed by deep convective clouds while the moderate LW warming in the 40–60 °S latitude band is due to persistent MBL clouds.

Further analyses are performed on the simulated biases in two dynamically-driven regimes determined by the vertical motion at 500 hPa (ω500) from MERRA. A regime analysis is instigated to provide analytics for parameterizations of convective- and stratiform-type clouds. Areas of moderate-to-strong upward (downward) motion (ω500 < –25 [> 25] hPa day^{-1}) are assumed to be dominated by convective (stratiform) clouds. Based on the dynamically-driven regime analysis, the follow conclusions can be made

3) While the observed CF in the ascent and descent regimes are similar (69 vs 66%), the CWPs are much larger in the ascent regime (113 vs 83 g m^{-2}) due to the existence of deep convective clouds. As a result, the SW/LW CREs are stronger in the ascent regime, while the net CRE is stronger in the descent regime due to the relatively weak LW warming effect. The multimodel mean over (under) predicts CF and CWP in the ascent (descent) regime. The multimodel mean simulated TOA all- and clear-sky fluxes are biased by less than 3.0 W m^{-2} and CREs are within ~5 W m^{-2} in both regimes. Biases in the simulated TOA radiation fields are mostly consistent with their CF and CWP biases.
4) Surface fluxes are also analyzed from five reanalyses, CERES-MODIS/EBAF, and ARM observations at two sites located close in proximity to the ascent and descent

regimes. In general, the reanalyses can capture the seasonal cycle of CF and surface downward SW and LW fluxes, and the SW transmission, at the ARM Azores and TWP-C2 sites. The CF is underpredicted by ~10% at the Azores site, which translates to too much SW radiation being transmitted to the surface, especially during the winter and spring months. At TWP-C2, CF is over predicted by ~10% but the surface SW transmission is within 0.02 of the observations.

5) Sensitivity studies have shown that the magnitude of SW CRE (cooling) increases significantly with increasing CF with nearly the same sensitivity over both the ascent and descent regimes (–1.12 and –1.34 W m^{-2} $\%^{-1}$, respectively). The model simulations provide similar relationships. The 33-model ensemble underestimates the sensitivity between SW CRE and CF by 0.01 and 0.27 Wm^{-2} $\%^{-1}$ in the strong ascent and subsidence regions, respectively. Conversely, the observed LW CRE increases with increasing CF but with different sensitivities in the two regimes (a strong warming of 0.82 Wm^{-2} $\%^{-1}$ and a moderate warming of 0.23 W m^{-2} $\%^{-1}$ over the ascent and descent regime, respectively). The difference in sensitivity is due to the distinct cloud-top temperature characteristics of deep convective clouds (ascent) and stratiform marine boundary layer clouds (descent). The multimodel ensemble does a fair job in simulating the observed LW sensitivity in the descent regime (bias of 0.05 W m^{-2} $\%^{-1}$), however it provides an overly sensitive LW CRE (0.35 W m^{-2} $\%^{-1}$ bias) in tropical and mid-latitude ascent regions.

6) The dominant sources of error related to the simulations of CRE are identified. The error sources that contribute largely to the regime-averaged CRE errors are: the modeled errors in the LW CRE sensitivity to CF in the ascent regime, the errors in the simulated CF and CWP amounts, and the sensitivities of SW CRE to CF and CWP in the descent regime. Overall, the biases in simulated CF (amount and sensitivity) contribute more to the error in simulated CREs.

CHAPTER IV

RADIATIVE FLUX PROFILES DETERMINED THROUGH ONE-DIMENSIONAL RADIATIVE TRANSFER MODELING USING SATELLITE-DERIVED CLOUD AND ENVIRONMENTAL PROPERTIES

A Clear-sky Radiation Closure Study (*Dolinar et al*. 2016b)

As mentioned in Chapter 3, to understand the true effect of clouds on the radiation budget, the clear-sky radiative properties must be quantified. We revealed that the simulated TOA SW/LW clear-sky fluxes from an assortment of GCMs and reanalyses can be biased by up to ~7 W m^{-2} on global average, with biases of > 40 W m^{-2} in some regions. We claim that surface characteristics have a big impact on the estimation of clear-sky fluxes at the TOA. Clear-sky fluxes are also dependent on the profiles of temperature, ozone, and water vapor. Section 1 of Chapter 4 introduces this concept and demonstrates how the calculated clear-sky fluxes at the TOA and surface can vary based upon the selection of meteorological input profiles in radiative transfer calculations. This section also details a method for achieving radiation closure at the surface and TOA for clear-sky scenes.

Background

Achieving a better understanding of clear-sky radiative transfer is an ongoing effort (i.e., *Chen et al.* 2018). The primary goal of satellite projects such as CERES (*Wielicki et al.* 1996), ISCCP (*Zhang et al*. 2004), and the Global Energy and Water Cycle Experiment (GEWEX) Surface Radiation Budget (SRB) (*Stackhouse et al*. 2011) is to provide a global estimate of the interactions between clouds and radiation. These data sets are frequently used as evaluation tools for climate model simulations of clouds and radiation budgets

(*Wild et al.* 2006; *Pincus et al.* 2009; *Dolinar et al.* 2015; *Stanfield et al*. 2015; *Wild et al*. 2015; *Ruzmaikin et al.* 2015; *Dolinar et al.* 2016). For CERES, surface radiation budgets are computed from coincident spectral imagers on sun-synchronous (e.g., MODIS) and geostationary platforms using a simplified one-dimensional RTM. While inputs to the RTM, and the subsequent computed fluxes, rely on simple parameterizations, they can be tuned and constrained by the CERES-measured TOA fluxes.

In ISCCP and GEWEX SRB, surface radiative fluxes are computed using either a RTM or radiation parameterization. In each project, the derived surface radiative fluxes depend on the input of atmospheric temperature and water vapor profiles. In CERES, pressure, temperature, and water vapor profiles are specified from Goddard Earth Observing System (GEOS) version 5.4.1 (*Bloom et al.* 2005), a gridded reanalysis data product from the Goddard Modeling and Assimilation Office (GMAO). In ISCCP and SRB, temperature and water vapor are retrieved directly from microwave sounders (*Zhang et al.* 2004). In a study by Moy et al. (2010) rapid RTM (RRTM)-computed clear-sky outgoing LW fluxes at the ARM SGP site were compared with observed fluxes from CERES. The RRTM LW fluxes are accurate to 0.2 and 0.8% of CERES when coincident radiosonde and AIRS-retrieved profiles are used, respectively. Additionally, Susskind et al. (2012) found that CERES and AIRS clear-sky outgoing LW estimates correlate well, despite differences in retrieval algorithms, RTMs, and input data. Charlock and Alberta (1996) compared observed surface all-sky and clear-sky SW and LW fluxes to RTM-

calculated fluxes at the ARM SGP site. Two types of input profiles are used to calculate the surface fluxes. Each produces a different result but is biased in the same direction.

Understanding the sensitivity of the calculated surface radiative fluxes to atmospheric input profiles is a necessary prerequisite for developing global radiation data products. The characterization of clouds (e.g., cloud amount, cloud overlap, and microphysical properties) proves to be one of the largest sources of uncertainty in deriving surface fluxes. However, the ambiguity of calculating clear-sky fluxes is also worthwhile to investigate because it offers a foundation for scientists to understand the RTMs calculations without the inherent issues associated with clouds (perhaps related to ice cloud optical property parameterizations). The calculated surface clear-sky LW radiative flux is primarily determined by the atmospheric temperature and water vapor profiles and surface temperature, while the SW flux is mainly a function of the scattering and absorption of atmospheric molecules and aerosols and the surface albedo. In this study, the temperature and water vapor profiles from a newly developed satellite-surface hybrid product and MERRA-2 are used as input to a one-dimensional RTM to calculate clear-sky surface and TOA radiative fluxes.

Methodology

A-Train satellite overpasses within a grid box of 120 × 120 km^2 centered at each ARM site are first determined during the period of August 2004 to December 2013. Once the overpass days are selected, a two-step cloud screening process is performed. First, the ARM ARSCL cloud product is used to screen for clouds within a 3-hour period centered

on the satellite overpass time. A clear-sky case is identified using a combination of the ARM ground-based MMCR, ceilometer, and lidar observations during the 3-hour period. Once clear-sky cases are identified by the ARM ground-based observations, a secondary clear-sky screening is performed through the inspection of the CERES SSF-derived, clear-sky fraction. If the CERES-derived clear-sky fraction in the 120 × 120 km^2 area centered on the ARM site is greater than ~95%, these clear-sky cases can be used in this study.

From August 2004 to December 2013, a total of 51 cases are identified at the ARM SGP site and 13 cases at the ARM TWP-C3 site. Polar-orbiting satellites, such as those in the A-Train, scan the high latitudes more frequently than at lower latitudes. However, the cloud frequency of occurrence at the ARM NSA is rather large (76%; *Dong et al.* 2010), limiting the total number of available clear-sky cases to 17. A list of the clear-sky cases at the three ARM sites is provided in Appendix A.

Once the clear-sky cases are identified, vertical profiles of temperature, water vapor mixing ratio, and ozone mixing ratio are generated from the ARM-merged soundings and satellite (MLS and AIRS) retrievals over three ARM sites, and are used to evaluate the MERRA-2 profiles. Tropospheric profiles of temperature and water vapor are from the ARM-merged soundings (surface to 100 hPa), while ozone is from AIRS (surface to 260 hPa). All upper atmosphere profiles are from MLS. These generated profiles will henceforth be referred to as the hybrid profiles. The hybrid profiles are also used as input to the RTM to calculate clear-sky surface and TOA radiative fluxes for the radiation closure study.

Evaluation of MERRA-2 clear-sky temperature, ozone, and water vapor profiles at three ARM sites

The hybrid profiles are used to evaluate the suitability of using MERRA-2 (or more broadly, GEOS-5) vertical profiles of temperature, ozone mixing ratio, and water vapor mixing ratio for computing surface, TOA, and in-atmosphere radiative fluxes with the Fu-Liou RTM. The fluxes are independently calculated using the hybrid, MERRA-2, and climatological mean profiles, with consistent surface properties to assess uncertainty in flux estimates related to the meteorological profiles themselves. The climatological mean profiles are from the World Meteorological Organization (WMO) and are made available with the RTM source code. While the climatological mean profiles are for all-sky conditions (cloudy and clear), they offer an additional measure for assessing the sensitivity of RTM-calculated fluxes to atmospheric profiles.

Figure 30 presents the clear-sky vertical profiles of temperature, ozone mixing ratio, and water vapor mixing ratio for the 51 selected cases at the ARM SGP site. Despite the inherent unrepresentativeness between the MERRA-2 grid box (0.500° × 0.625°) and the point of the hybrid profile, the temperature profiles match very well (within 2%) through the atmospheric column and their differences are nearly indistinguishable (Fig. 30a). The mid-latitude climatological mean temperature, however, is slightly colder than the hybrid and MERRA-2 temperatures below ~300 hPa and is too warm from ~200 to 15 hPa and above 4 hPa.

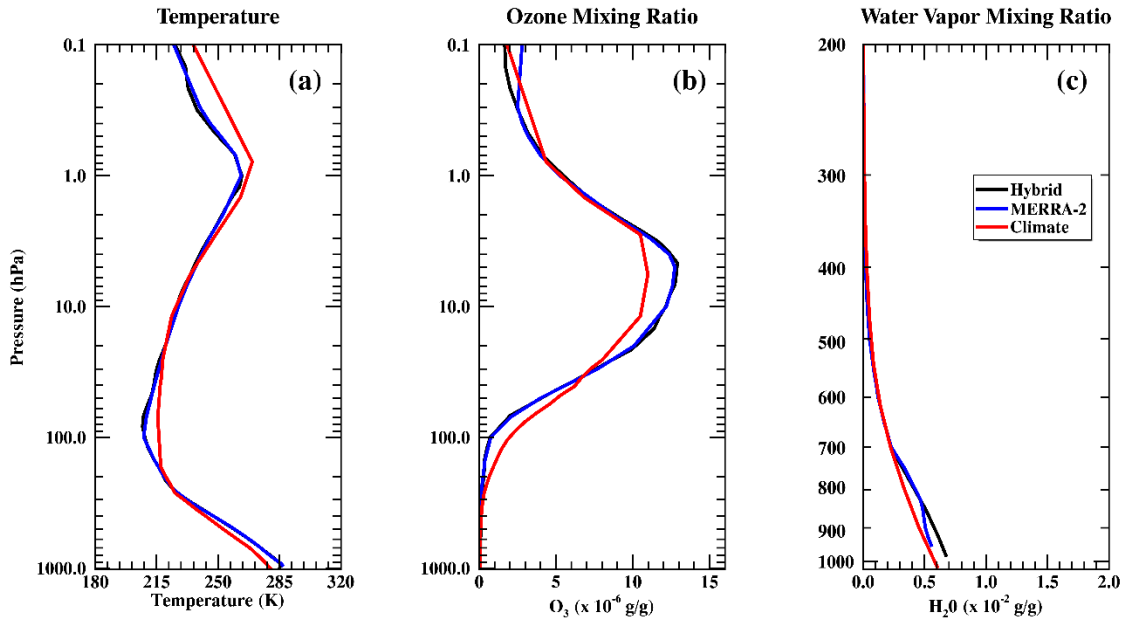

Figure 30: Vertical profiles of (a) temperature (K), (b) ozone mixing ratio (× 10^{-6} g/g), and (c) water vapor mixing ratio (× 10^{-2} g/g) at the ARM SGP site. These profiles represent the clear-sky cases during the August 2004 to December 2013 period (see Appendix #). The blackline represents the hybrid profiles from the ARM-merged soundings (below 100 hPa) and the Microwave Limb Sounder (MLS) for atmospheric temperature and water vapor. The ozone profile (below 260 hPa) is from the Atmospheric Infrared Sounder (AIRS) and MLS. The blue line is from the closest MERRA-2 grid point, and the red line is the mid-latitude climatological mean.

Since stratospheric ozone is directly assimilated into MERRA-2, it is not surprising that the hybrid and MERRA-2 ozone profiles in Fig. 30b match very well. On the other hand, MERRA-2 does not assimilate tropospheric ozone, which causes differences of 200–400% for some cases (not shown). The mid-latitude climate mean ozone mixing ratio is less than the hybrid and MERRA-2 profiles in the middle to upper stratosphere but is slightly larger in the upper troposphere and lower stratosphere.

Lastly, the clear-sky water vapor mixing ratios at the ARM SGP site are shown in Fig. 30c. Since the water vapor mixing ratios are relatively small above the troposphere,

the profiles are presented at ~1000–200 hPa for enhanced clarity. The hybrid and MERRA-2 water vapor mixing ratios match very well above ~850 hPa. However, below 850 hPa, the MERRA-2 water vapor profile diverges from the hybrid profile to the drier side by < 0.25×10^{-2} g/g. On the global scale, a moist bias in MERRA-2 of 75–150% has been reported in the upper troposphere when compared with AIRS and MLS (*Jiang et al.* 2015). The mid-latitude climate mean water vapor mixing ratio is less than both the hybrid and MERRA-2 profiles in the lower troposphere (below 700 hPa).

Similarly, the vertical profiles of temperature, ozone, and water vapor mixing ratio over the ARM NSA site are illustrated in Fig. 31. Note that the solid lines represent the average profile from the five snow-free cases and the dashed lines are for the 12 snow cases identified at this site. The distinction between the snow and snow-free cases is made because of their contrasting atmospheric and surface conditions. The primary source of moisture for this region is restricted when sea ice and snow cover persist in the Arctic Ocean. This will affect not only cloud formation (although not a process we are concerned with in this study) but also heat and atmospheric energy transport (*Hwang et al.* 2011*; Qui et al*. 2018).

The MERRA-2 temperature profiles (Fig. 31a) for both the snow and snow-free cases at the ARM NSA site show an excellent agreement with the hybrid profiles through most of the troposphere and stratosphere. For the snow-free cases, the MERRA-2 temperature is slightly colder just below the stratopause (~ 1–2 hPa) and warmer above 0.3 hPa by ~20 K. Nevertheless, MERRA-2 resolves the low-level temperature inversion for

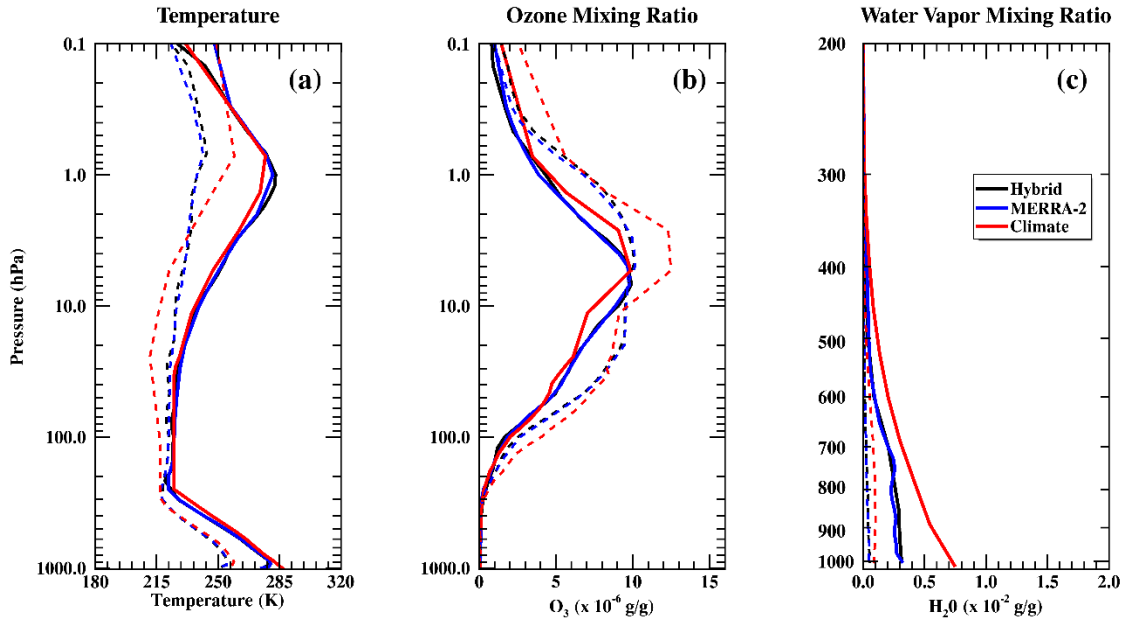

Figure 31: Same as Fig. 30 but showing the vertical profiles of (a) temperature (K), (b) ozone mixing ratio ($\times 10^{-6}$ g/g), and (c) water vapor mixing ratio ($\times 10^{-2}$ g/g) at the ARM NSA site. The solid lines are for snow-free cases (surface albedo, $\alpha < 0.3$), whereas the dashed lines are for snow cases ($\alpha \geq 0.3$). The red line represents the Arctic climatological mean.

both snow and snow-free cases. The Arctic climate mean temperature is warmer in the troposphere and colder in the stratosphere for the snow-free cases and does not capture the low-level inversion. A typical decrease in temperature is observed through the shallow troposphere at the NSA site for a snow-covered surface, whereas in the stratosphere, a slightly isothermal temperature structure is seen in both the hybrid and MERRA-2 profiles. The temperature change through the stratosphere is only ~20 K when the surface albedo is greater than 0.3 (snow cases), as opposed to the 60+ K change in the snow-free cases.

Climatologically, the temperature matches well with the hybrid profile in the troposphere for snow cases but diverges greatly in the upper atmosphere.

Ozone in the Arctic is depleted more efficiently during the northern hemisphere summer months. Therefore, the stratospheric ozone mixing ratios for the snow cases are larger than those of the snow-free cases as shown in Fig. 31b. Similar to the ozone comparison at the SGP site, the MERRA-2 and hybrid profiles match very well through the whole column. As previously stated, water vapor in the Arctic has a strong seasonal dependence due to the variation of sea ice coverage. As expected, the water vapor mixing ratios from the snow-free cases are larger than those from the snow cases. For the snow cases, the water vapor mixing ratios are almost constant ($\sim 0.15\times10^{-2}$ g/g) through the entire troposphere, which is well replicated in MERRA-2. Once the sea ice has begun to retreat (i.e., the snow-free cases), the atmospheric water vapor mixing ratios increase in all three profiles. The climate-mean water vapor mixing ratio is too moist and almost twice as large as the hybrid and MERRA-2 values through the troposphere. However, this result is expected as the climatological mean profiles are for all-sky conditions.

Figure 32 illustrates the temperature, ozone, and water vapor mixing ratio profiles at the TWP-C3 ARM site. Darwin is located directly on the northern coast of Australia; therefore, coastal processes (e.g., land/sea breezes) modify the atmospheric conditions at this site. Temperature (Fig. 32a) is well reproduced inMERRA-2 at the TWP-C3 site through the troposphere; however, a slight discrepancy is seen just above the tropopause and below the stratopause, which could be an artifact of the coarser vertical resolution of

MERRA-2. The tropical climate mean temperature agrees well with the hybrid and MERRA-2 profiles in the troposphere but is slightly warmer in the stratosphere and mesosphere.

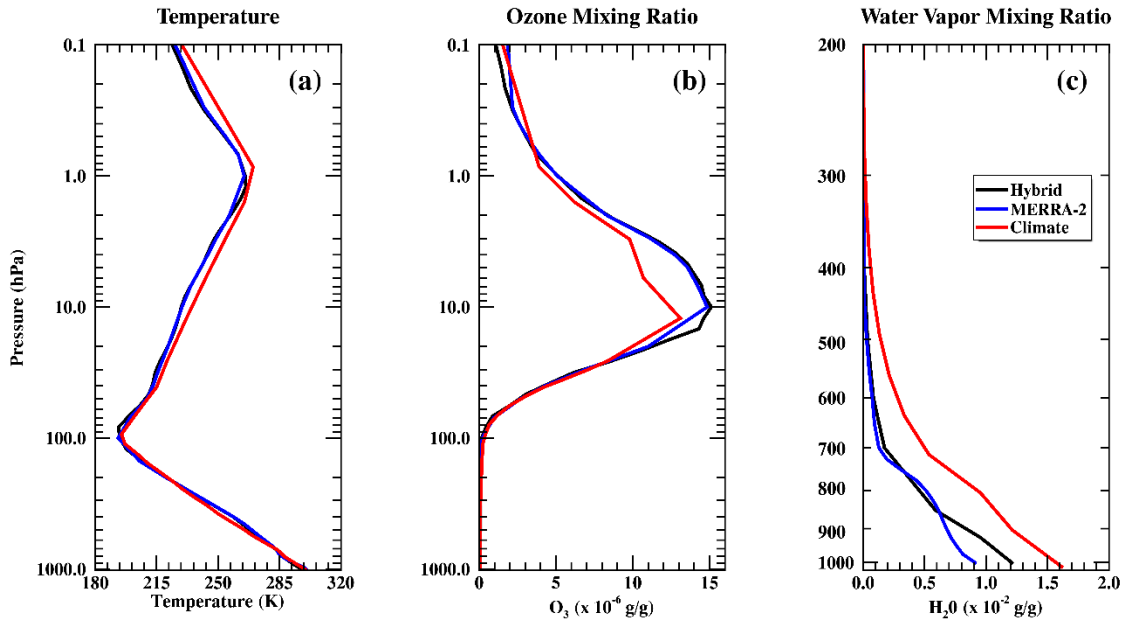

Figure 32: Same as Fig. 30 but showing vertical profiles of (a) temperature (K), (b) ozone mixing ratio ($\times 10^{-6}$ g/g), and (c) water vapor mixing ratio ($\times 10^{-2}$ g/g) at the ARM TWP-C3 site. The red line represents the tropical climatological mean.

The TWP-C3 ozone comparison is similar to the results at the ARM SGP and NSA sites, where the ozone profiles from MERRA-2 and the hybrid data set are very close. Yet still, a noticeable discrepancy between the two datasets can be seen from ~10 to 20 hPa, where MERRA-2 is slightly smaller. Tropospheric water vapor at the ARM TWP-C3 site is modified by the adjacent oceanic environment via transport by mesoscale features (e.g., land/sea breezes) and general circulation patterns. For the 13 selected cases at this site, all three water vapor mixing ratios are much higher than those at the ARM SGP and NSA

sites. Both the hybrid and MERRA-2 water vapor mixing ratios are much drier than the tropical climatological mean through the troposphere by $< 0.6 \times 10^{-2}$ g/g, again likely due, in part, to the fact that the climate mean profile is for all sky conditions. It is expected that the unrepresentativeness between the MERRA-2 grid box and the ARM point location may lead to their relatively large difference (1000–3500% for several cases; not shown), especially since the TWP-C3 site is located directly on the coast.

Based on the comparisons made in three different climatic regimes, we can make the following conclusions. The MERRA-2 atmospheric temperature profiles are nearly identical to the hybrid ones, and the climate mean temperature profiles agree with the hybrid ones within several Kelvin. Since MLS ozone data are directly assimilated into MERRA-2, it is not surprising that the MERRA-2 and hybrid ozone profiles match extremely well at all three ARM sites. Most of the MERRA-2 water vapor mixing ratios agree well with the hybrid ones over three sites except for in the boundary layer at the ARM TWP-C3.

Radiative Closure of the Calculated Clear-sky TOA and Surface Fluxes

The clear-sky surface and TOA radiative fluxes are calculated using the NASA Langley-modified RTM with inputs from three different profile data sets at three ARM sites. For the clear-sky cases selected in this study, only the vertical profiles of temperature, ozone mixing ratio, and water vapor mixing ratio are required as input, along with the solar zenith angle, surface albedo, AOD (including aerosol type), skin temperature, and a sun-Earth distance correction coefficient. In this study, the surface and TOA radiative fluxes

are calculated for each clear-sky case at each site with the same surface characteristics but with different vertical profiles of temperature, ozone, and water vapor from the hybrid, MERRA-2, and climate mean.

Due to the inherent surface inhomogeneity of coastlines, we do not expect the ARM-observed surface characteristics to necessarily represent the large CERES field-of-view (FOV). The is especially true at the NSA site when sea-ice and snow can exist within the satellite FOV while the snow has completely melted at the ground station. Dong et al. (2016) demonstrated that for Arctic stratus clouds at the ARM NSA site, radiative closure can be achieved at the surface and TOA (over a 30 × 30 km^2 domain) by adjusting the ARM-measured surface albedos (63.6% and 80% of the ARM surface albedos for snow-free and snow cases, respectively) to account for the land/sea contrast within the domain.

Table 7 lists the average ARM-measured surface albedos and Aerosol Robotic Network (AERONET) AODs for the identified clear-sky cases at three ARM sites selected for this study. At the ARM SGP and NSA sites, we assume a continental aerosol, while at the TWP-C3 site an urban aerosol is assumed in the RTM calculations (consider these aerosols as type 1). The average ARM-observed surface albedos are 0.209, 0.225 (0.796), and 0.163 at the SGP, NSA for snow-free (snow), and TWP-C3 sites, respectively. The AOD (at 500 nm) values are 0.122, 0.076 (0.067), and 0.137, respectively. Case-specific AOD's come from AERONET observations when they are available; otherwise the climatological mean is used. Both the surface albedo and AOD have a significant impact on the TOA reflected SW flux (SW_up) and SW_down at the surface. The predominant

aerosol types observed at the three locations include nitrates, sulfates, sea salt, smoke, and dust (*Quinn et al.* 2002; *Alexandrov et al*. 2005; *Qin and Mitchell* 2009).

Table 7: The average surface albedos and AODs from the selected clear-sky cases at the three ARM sites[a].

	SGP	NSA		TWP-C3
		Snow ($\alpha \geq 0.3$)	**Snow-free ($\alpha < 0.3$)**	
Surface albedo	0.209	0.796	0.225	0.163
AOD	0.122	0.076	0.067	0.137

[a] For cases without an AOD observation, the AERONET 500 nm mean value was used (0.14, 0.08, and 0.14 for SGP, NSA, and TWP-C3, respectively).

Table 8 provides the mean observed and RTM-calculated SW and LW fluxes at the TOA and surface, respectively, with inputs from the atmospheric profiles over three ARM sites. The calculated fluxes prior to being tuned are relatively close (within ~11 W m^{-2}) to the observations at the ARM SGP site while the largest average flux differences (> 50 W m^{-2}) occur at the TWP-C3. This is not surprising, given that the surface area around the ARM SGP is rather homogenous in comparison to the other two sites; the ARM PSP-measured surface albedos are relatively close to the mean albedo over a 120 × 120 km^2 domain. In contrast, the ARM TWP-C3 and NSA sites are located directly on the coast. The ARM PSP-measured surface albedos at the NSA and TWP-C3 sites cannot effectively represent the domain average albedos as discussed by Dong et al. (2016). Therefore, we must adjust the ARM-measured surface albedos to account for the land/sea contrast within the domain to reach radiative closure at both the surface and TOA.

Table 8: The average TOA and surface radiative fluxes (W m^{-2}) from CERES or ARM observations and un-tuned/tuned RTM calculations with inputs from the three profile types.

	TOA SW up	TOA LW up	Surface SW down	Surface LW down
SGP				
Hybrid	176.67/166.31	273.54/273.49	682.68/674.66	299.76/299.86
MERRA-2	177.37/166.84	273.05/273.00	689.97/681.95	292.86/292.96
Climate	173.49/163.43	259.59/259.54	667.88/660.09	275.17/275.26
Observations	165.31	273.16	672.44	302.55
NSA (snow α > 0.3)				
Hybrid	170.96/143.46	194.12/194.03	168.55/164.80	155.88/156.53
MERRA-2	170.98/143.44	193.20/193.11	168.73/164.93	155.00/155.67
Climate	162.90/136.92	190.42/190.39	160.48/157.01	183.73/184.34
Observations	145.67	195.61	160.48	159.58
NSA (snow-free α < 0.3)				
Hybrid	103.30/116.30	251.59/251.26	351.49/351.26	248.78/249.27
MERRA-2	103.47/116.53	246.85/246.70	352.53/352.27	245.71/246.22
Climate	100.02/112.40	247.92/247.80	337.83/337.69	299.36/299.75
Observations	118.93	247.02	352.38	248.24
TWP-C3				
Hybrid	168.06/121.30	311.37/308.26	789.10/769.13	355.38/358.95
MERRA-2	169.77/122.20	311.75/308.59	797.82/777.70	353.68/358.04
Climate	164.13/118.93	286.67/284.41	765.65/746.44	398.21/400.34
Observations	116.83	312.99	758.04	376.35

Dong et al. (2016) provided a method to calculate the domain average albedo based on the ARM NSA PSP-measured surface albedos and the adjacent ocean albedo (~0.06), based on the percentage of water and land within the domain. For snow-free cases, they found that the domain average albedo accounts for 63.6% of the ARM measurements, which was used in their study to reach radiative closure for both the surface and TOA radiation budgets. For snow cases, they discussed three possible conditions, including an

open ocean, an ocean with sea ice containing open leads, and an ocean that is completely covered by sea ice or snow, with albedos similar to the ARM PSP measurements (~0.8). While the domain-average albedos are different for these three conditions, the ARM PSP-measured surface albedos for snow cases were adjusted by 80% in the work of Dong et al. (2016). In this study, we follow a similar method as in Dong et al. (2016) to tune the ARM PSP-measured surface albedos to account for the water and land components of the domain; this is done to reach radiative closure for clear-skies at the surface and TOA over the ARM NSA and TWP-C3 sites.

Table 9: The applied changes to the observed surface albedo and AOD (by introducing a secondary aerosol) used to match the RTM-calculated fluxes to the observations.

	SGP	**NSA**		**TWP-C3**
		Snow ($\alpha > 0.3$)	**Snow-free ($\alpha < 0.3$)**	
ΔSFC α (%)	–10	–20	+20	–50
AOD_2/AOD_1	0.40	0.20	0.20	0.99

Table 9 offers the adjustments made to match the RTM-calculated radiative fluxes to within ~5 W m^{-2} of the observations when using the hybrid profiles as input. Admittedly, some of these values have been arbitrarily chosen to achieve the closest match between the calculated and observed fluxes (namely, AOD_2/AOD_1). To be clear, the aerosol ratio (AOD_2/AOD_1) is the ratio of the AOD for aerosol type 2 to that of the aerosol type 1. The aerosol type 2 at the ARM SGP is urban, while at the NSA and TWP-C3 sites it is maritime. With the inclusion of a secondary aerosol type, we adjusted the surface and TOA fluxes almost independently. At the SGP site, the ARM PSP-measured surface albedo is reduced

by 10%, which will account for the slight surface inhomogeneity in the CERES FOV centered at the ARM site. A majority of the surface inhomogeneity is attributed to crop type (e.g., wheat, grass, soybean, and alfalfa (*Li et al.* 2002). The aerosol ratio is set to 40% at the ARM SGP site. The surface albedo is also reduced (by 20%) at the ARM NSA site for the snow cases, following the conclusion in Dong et al. (2016), which may account for the different albedos from old and fresh snow surfaces and the nearby open water and leads (*Brandt et al.* 2005). An increase in albedo of 20% is applied for the snow-free cases at the NSA site, which is contrary to the conclusion in Dong et al. (2016). This change accounts for the sea ice observed by the large satellite FOV while the ARM PSP-measured surface albedos are below 0.3. The changes in surface albedo applied in this study are smaller than those used in Dong et al. (2016).

Although the maximum albedo threshold for snow-free cases is 0.3, this number represents the ARM site only. Again, the CERES FOV over the ARM NSA site is much larger than the point observation and may include snow surfaces and sea-ice within a grid box of 120 × 120 km^2, which will increase the albedo of the footprint. By visually investigating MODIS images for the five snow-free cases, we can confirm that sea ice and snow surfaces are partially present within the 120 × 120 km^2 domain centered on the ARM NSA site. The aerosol ratio is set to 20% for both snow-free and snow cases in this study.

To match the calculated SW fluxes to the observed values at TWP-C3, the albedo is reduced (by 50%) to account for the small ocean albedo within the domain. Since the ARM TWP-C3 site is located directly on the coast, there exists a strong albedo contrast

between the land surface (~0.16) and ocean (0.06), which is comparable to the NSA snow-free cases, but the actual percentage is dependent on the land and water coverage within the domain. At the TWP-C3 site, the aerosol ratio is set to 99%.

While adjusting the surface albedo and AODs described above, better agreements between the mean calculated fluxes and the observed values at each site are achieved and illustrated in Figure 33b (compared to the untuned results in Fig. 33a). Note that each point in Fig. 33 depicts the average flux difference (in %, [RTM-calculated minus observed]/observed × 100) from all cases at each site using inputs from the hybrid, MERRA-2, and climate mean profiles. Many of the symbols fall outside of the dashed lines (a bias of > 5 %) in Fig. 33a. However, some of these larger biases disappear after adjustments are made to the surface albedo and AODs (Fig. 33b); most of the calculated radiative fluxes using the hybrid and MERRA-2 input profiles are within 5% of the mean observed values.

For clarifying the results in Fig. 33, Table 8 lists the averaged surface and TOA radiative fluxes from the ARM/CERES observations and untuned/tuned RTM calculations with input from the three profiles at the three ARM sites. For example, the untuned surface and TOA SW and LW fluxes at the SGP site based on the hybrid profiles (red filled and open squares in Fig. 33a) agree with the observed fluxes to within 11 W m^{-2}; however, the difference is reduced to ~3 W m^{-2} after tuning. In general, our tuning parameters (surface albedo and AOD) can reduce the biases in the calculated SW fluxes but not for LW fluxes.

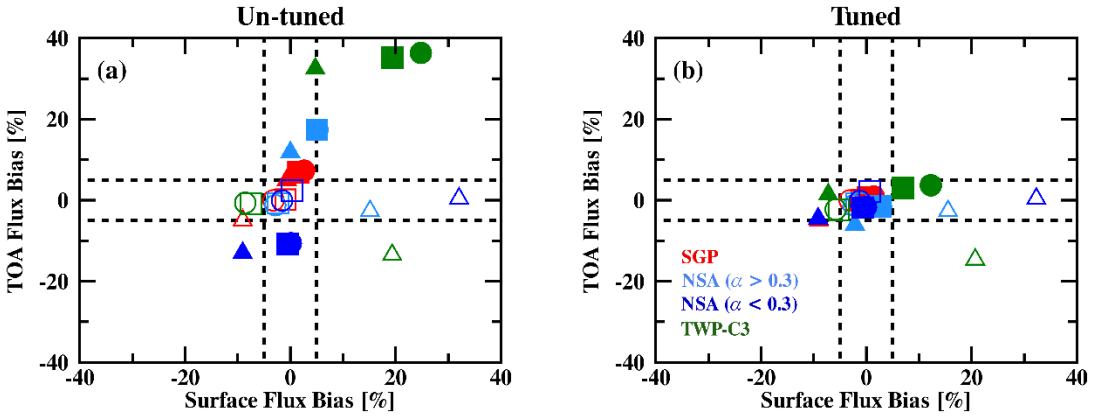

Figure 33: The average flux differences (%, [model – observation]/observation) between the ARM/CERES observations and Fu-Liou radiative transfer model (RTM) calculated (x-axis) surface and (y-axis) TOA fluxes using the hybrid (square), MERRA-2 (circle), and climate mean profiles (triangle). The symbols are color-coded for each site (red: SGP, light blue: NSA snow cases, blue: NSA snow-free cases, and green: TWP-C3). Biases in the (filled symbol) SW and (open symbol) LW fluxes are shown separately (a) prior to tuning and (b) after tuning.

The LW fluxes are mainly determined by atmospheric temperature and water vapor profiles and skin temperature, not by surface albedo and AOD. For example, at SGP, the large negative bias in the climate mean calculated surface LW_dn flux can be attributed to its relatively cold tropospheric temperature and relatively dry tropospheric water vapor mixing ratio as shown in Fig. 30. Nevertheless, the average error in the tuned surface LW_dn flux from the hybrid profiles is less than 3 W m^{-2}, which is consistent with Long and Turner (2008). However, the TOA LW_up flux is also negatively biased despite the warmer stratosphere/mesosphere in the climate mean profile. Therefore, we can state with confidence that other parameters (e.g., skin temperature) affect the TOA LW_up flux, and an additional study is warranted to determine the sensitivity.

For the 12 snow (surface albedo ≥ 0.3) cases at the ARM NSA site, the positive bias in surface LW_dn flux using climate mean profiles can be up to ~25 W m^{-2}. This result is likely due to the relatively large tropospheric water vapor and warmer temperature in the climatological Arctic winter profiles. The average calculated fluxes using the climate mean profile inputs continue to show some problems at the NSA site for the five snow-free cases. For instance, the calculated surface SW_dn and LW_dn fluxes are biased by approximately –15 and +50 W m^{-2}, respectively. Greater absorption of both SW and LW radiation is achieved by the relatively large tropospheric water vapor mixing ratio, a result that could be attributed to the fact that the climate mean profile is for all sky scenes. The large surface LW_dn bias could also be affected by the temperature profile, which is too large in the troposphere and does not resolve the low-level temperature inversion.

The green symbols in Fig. 33 represent the averaged biases at the ARM TWP-C3 site. A bias of greater than –20 W m^{-2} is determined for the surface LW_dn flux using the hybrid and MERRA-2 profiles, a result that is inconsistent with Long and Turner (2008) and is likely due to the skin temperature used in the RTM. In contrast to this large negative bias, the surface LW_dn flux calculated using the tropical climate mean profiles is positively biased by about the same amount. Because the tropospheric temperatures from three data sets at the ARM TWP-C3 site are consistent with each other, the large positive bias in the calculated surface LW_dn flux is most likely due to the moister climate mean tropospheric water vapor as shown in Fig. 32c. This result is consistent with the findings in Dong et al. (2006), where the atmospheric water vapor plays an important role to the

downward LW flux at the surface, but is insignificant to the downward SW flux at the surface.

The opposing biases from the three input profiles suggest that the actual atmospheric water vapor should fall between them. The large negative bias (~ –26 W m^{-2}) in the TOA LW_up flux can also be attributed to the larger climate mean tropospheric water vapor, as the moister atmosphere absorbs more LW radiation emitted by the surface. Also, as previously stated, the skin temperature used in the calculation at TWP-C3 is from the lowest level of the ARM-merged sounding because IR thermometer data are not available at TWP-C3 during the study period. Assuming a typical lapse rate, the skin temperature would be larger than the ones used in this study. As such, if the actual skin temperatures were to be used, we expect a smaller absolute bias in the TOA LW_up flux at TWP-C3. Moreover, Moy et al. (2010) have found that daytime variability in the calculated TOA LW_up flux can be reduced if satellite footprint estimates of skin temperature were used in lieu of point measurements. This finding may help to justify the large error in surface LW_dn flux in this study.

Figure 33 and Table 8 provide an overall summary of the comparisons between the average RTM-calculated and ARM-observed radiative fluxes, which may obscure some detailed information, such as large compensating errors from several cases. Therefore, we generate Fig. 34 to detail the individual clear-sky cases for each parameter at each site. It is apparent that not all the calculated fluxes are biased equally or in the same direction. For

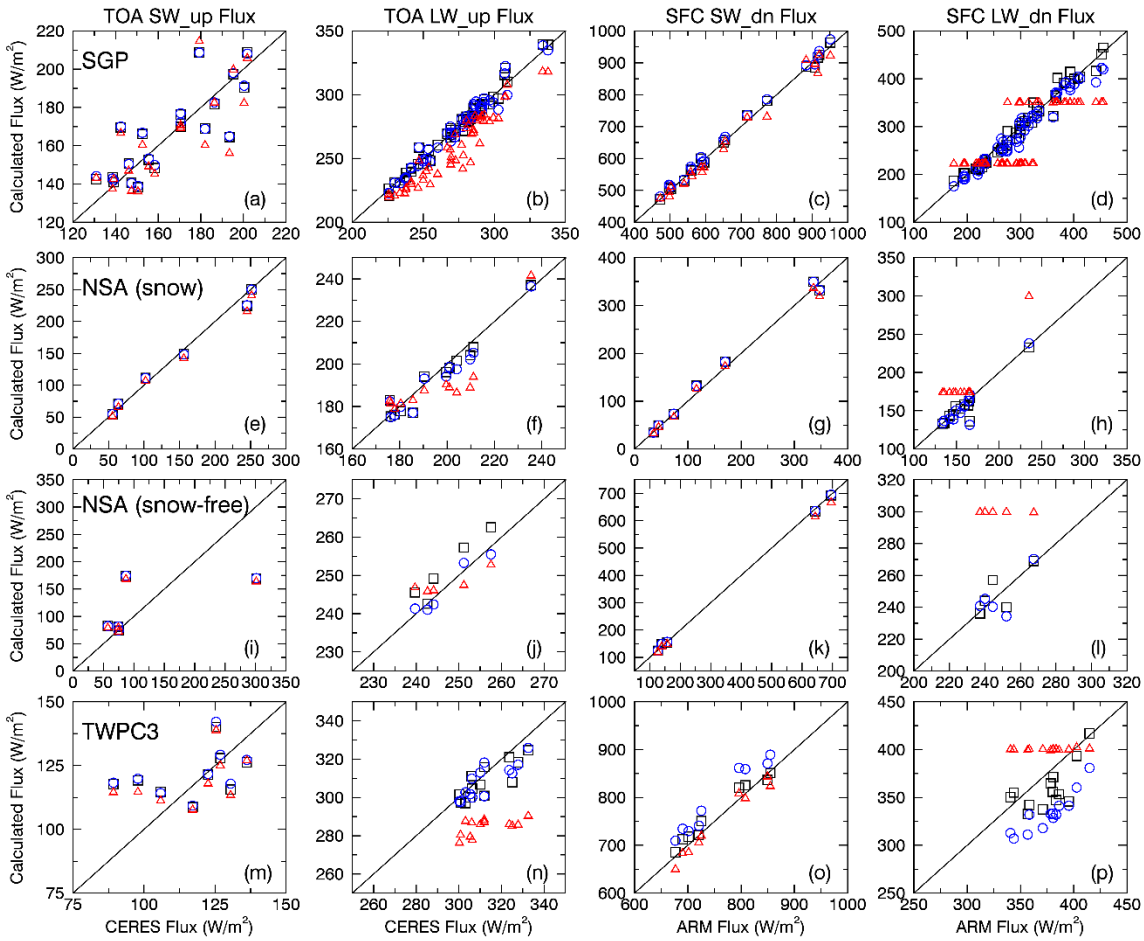

Figure 34: Scatterplots of the ARM/CERES-observed fluxes versus the tuned RTM-calculated fluxes from the three input profiles (black: hybrid; blue: MERRA-2; red: climate mean). Each symbol corresponds to a specific clear-sky case. Results are shown for all three sites (a–d) SGP, (e–h) NSA-snow cases, (i–l) NSA-snow-free cases, and (m–p) TWP-C3. From left to right, the columns represent the TOA SW_up, TOA LW_up, surface SW_dn, and surface LW_dn flux comparisons.

example, in Fig. 34a the calculated clear-sky TOA SW_up fluxes at the ARM SGP site are both positively and negatively biased against the CERES instantaneous fluxes by nearly 30 W m^{-2} for some cases. However, the average bias is only 1–2 W m^{-2}. A similar statement can be made about the calculated TOA SW_up fluxes at NSA (snow-free cases; Fig. 34i)

and TWP-C3 (Fig. 34m) and the surface LW_dn fluxes at SGP (Fig. 34d) and TWP-C3 (Fig. 34p). On the other hand, the fluxes calculated with the climate mean profiles have a tendency of being biased either too high or too low (e.g., Figs. 34b, h, l, and n).

Table 10 summarizes the 90% confidence intervals for the calculated surface and TOA, SW, and LW radiative fluxes. These values are calculated based upon the Student's t distribution as

$$-t < \frac{\bar{X}-\mu^*}{\sigma/\sqrt{n}} < t \tag{11}$$

where $\bar{X}$ is the mean-calculated flux, σ is the standard deviation of the calculated flux for all cases, n is the number of cases, and μ* provides the upper and lower limits of the confidence interval (based on the value of ±t). The relatively small range of this statistic for the LW fluxes suggests high confidence in our calculated radiative fluxes, which is maintained by the small σ of the individual case fluxes. However, the calculated surface SW_dn and TOA SW_up fluxes at the NSA site have a relatively large σ value, which can also be seen clearly seen in Fig. 34k, and small sample number; the combination of these two results in a 90% confidence interval range of more than 130% and 80%, respectively. Depending on the site and flux type (TOA SW/LW_up and surface SW/LW_dn), the 90% confidence intervals contain anywhere between ~10 and 75% of the individual case values. The large standard deviations, which can be caused by a skewed distribution of solar zenith angles (or Julian day), are believed to limit the number of samples within some intervals.

The Student's t distribution is only appropriate for normally distributed data, which is not necessarily valid for all sites/cases here. Based on the flux comparisons in Figs. 33 and 34, as well as in Tables 8 and 10, we can conclude that the input of accurate atmospheric profiles in the RTM plays an important role in calculating the surface and TOA SW and LW fluxes and that some surface characteristics must be adjusted to achieve radiative closure.

Table 10: The 90% confidence intervals for the average tuned RTM-calculated fluxes (W m^{-2}) $[\mu^*_{lower}, \mu^*_{upper}]$[a].

	TOA SW_up		**TOA LW_up**		**Surface SW_dn**		**Surface LW_dn**	
	Interval	**%**	**Interval**	**%**	**Interval**	**%**	**Interval**	**%**
SGP								
Hybrid	[157.2,175.4]	11.0	[267.0,280.0]	4.8	[608.2,714.1]	19.7	[282.3,317.4]	5.2
MERRA-2	[157.8,175.9]	10.9	[266.6,279.4]	4.7	[615.2,748.7]	19.6	[276.4,309.5]	4.9
Climate	[153.9,173.0]	11.7	[253.3,265.8]	4.8	[594.0,726.2]	20.0	[260.3,290.2]	4.5
NSA (snow $\alpha \geq 0.3$)								
Hybrid	[84.5,202.4]	82.1	[184.7,203.4]	9.6	[69.2,260.4]	133.3	**[142.8,170.3]**	16.7
MERRA-2	[84.5,202.4]	82.2	[184.1,202.1]	9.3	[69.0,260.9]	133.8	**[140.7,170.7]**	18.2
Climate	[79.7,194.2]	83.6	**[181.7,199.1]**	9.1	[64.2,249.9]	135.6	**[165.6,203.1]**	23.9
NSA (snow-free $\alpha < 0.3$)								
Hybrid	**[68.0,164.6]**	83.1	**[243.4,259.2]**	6.3	**[78.2,624.4]**	155.5	**[236.3,262.2]**	7.4
MERRA-2	**[68.0,165.0]**	83.2	**[239.7,253.4]**	5.5	**[78.6,262.0]**	155.4	**[232.9,259.6]**	7.6
Climate	**[65.7,159.1]**	83.1	**[245.1,250.5]**	2.2	**[73.0,602.4]**	156.8	**[299.6,299.9]**	0.1
TWP-C3								
Hybrid	**[115.6,127.0]**	9.4	[303.7,231.8]	3.0	[726.1,812.2]	11.2	**[347.4,370.5]**	3.0
MERRA-2	**[116.2,128.2]**	9.8	[304.1,313.1]	2.9	[733.5,821.9]	11.4	[348.0,368.1]	2.6
Climate	[112.9,124.9]	10.1	[282.2,286.6]	1.5	[701.9,791.0]	11.9	**[399.9,400.7]**	0.1

[a] The percent is defined as $[(\mu^*_{upper} - \mu^*_{lower})/] \times 100\%$. The bolded values contain ≥ 50% of the individual cases.

A Global Record of Single-layered Ice Cloud Properties and Associated Radiative Heating Rate Profiles From an A-Train Perspective

In Chapter 3, we revealed that the CF and CWP are overpredicted by GCMs and reanalyses in areas of atmospheric ascent where upper-tropospheric ice clouds typically form through convective processes. Moreover, we show that clouds and their TOA CREs are not well correlated with observations ($r < 0.6$) in these areas. Stanfield et al. (2014) and Li et al. (2012) also confirm that too much cloud ice is predicted in the tropics by CMIP5 GCMs.

Major differences in the vertical distribution of ice and liquid clouds simulated by global models are the product of poorly constrained observations (*Jiang et al.* 2012; *Li et al*. 2012; *Eliasson et al.* 2011). Jiang et al. (2012) reported on some improvements of simulated ice clouds in CMIP5 compared with their earlier versions in CMIP3. Although the mean bias and spread of ice water content (IWC) were reduced in the refined model versions, some notable discrepancies in the simulated ice clouds still exist. Considerable spread and bias remain in the simulated upper tropospheric (~215 and 100 hPa) IWC and water vapor in the tropics (30°N − 30°S) when compared with MLS and CloudSat retrievals (*Jiang et al.* 2010 and 2012; *Li et al.* 2012). Additionally, the simulated diurnal variation of partial ice water path (pIWP) over the tropical upper troposphere shows bias in the mean state, amplitude, and phase lag compared to the Superconducting Submillimeter Limb Emission Sounder (SMILES) on board the International Space Station (ISS); the oceanic

component has a larger discrepancy than over land, suggesting a poorer understanding of their development (*Jiang et al.* 2015).

These results are not to be taken lightly as the radiative heating rate profiles are a function of cloud height, cloud particle distributions, and fractional coverage. Su et al. (2009) have shown how the vertical profile of radiative heating is improved by including MLS observations of IWC. MLS is more sensitive to optically thin cirrus clouds ($0.01 < \tau < 0.2$) that oftentimes go undetected by CloudSat and most certainly by MODIS. Surface and TOA CREs vary in response to different radiative heating rate profiles, which are shown to be variable based upon the amount of cirrus clouds detected in the upper troposphere by satellites (Su et al. 2009).

Therefore, there is promise for reducing the uncertainty in simulated vertical profiles of ice clouds and their heating rate profiles. The problem must be addressed using methods that are consistent with Su et al. 2009; the global radiative impacts of thick and thin ice clouds must be fully resolved. This section accomplishes that by optimizing the synergy of CloudSat and CALISPO measurements of ice clouds.

Background

Since ice clouds can exist in a variety of conditions and form by several different forcing/formation mechanisms (*Sassen et al.* 2008; *Cziczo et al.* 2013), and given that cirrus clouds themselves are the most common cloud type in the atmosphere (*Mace et al.* 2009; *Stubenrauch et al.* 2013), resolving their range of radiative impacts is extremely important. Correctly resolving the radiative impacts of single-layered ice clouds from

globally observed cloud microphysical properties will provide useful data for climate model evaluation. The evolution of deep convective and large-scale cloud systems in global models partially relies on the detrainment of cloud ice (*Del Genio et al.* 2012; *Elsaesser et al.* 2017), which as an extension can be regarded as a driver of the radiative heating of the clouds (or vice versa). Furthermore, profiles of cloud radiative heating can act to modify the stability of the environment and affect vertical motion (*Del Genio et al.* 2012). Vertical radiative heating rates can therefore be used to diagnose errors in simulated cloud fields in global models and perhaps improve detrainment as well as the occurrence and development of ice clouds.

Single-layered ice clouds are sampled for this study due to the relative simplicity in isolating their effects on the Earth's radiation budget. The interaction of radiation with multi-layered clouds and precipitation is a more complex problem. Cloud overlap assumptions used in current modeling frameworks are oftentimes oversimplified or incorrectly represented and can lead to large biases in simulated radiation fields, especially for highly complex cloud systems such as those found in deep convection (*Liang and Wang* 1997; *Barker et al.* 1999; *Hogan and Illingworth* 2000; *Zhang et al.* 2013). Moreover, singling out the radiative impact of ice clouds when they are close in proximity to falling hydrometeors further complicates the matter. While there is certainly a need for better resolving the radiative effects of multi-layer clouds, determining the radiative effects of single-layered ice clouds is also justified; resolving the radiative effects of the ice clouds themselves can help diagnose their modeled errors in climate simulations.

This study reports on the consistency of modeled TOA and surface SW/LW radiative fluxes and the range of radiative heating rate (Q_r) profiles of single-layered ice clouds from an assortment of independently developed datasets. We could have easily sampled only the ice cloud radiative properties derived and reported in 2B-FLXHR-LIDAR (*Henderson et al.* 2013) or CCCM (*Kato et al.* 2011) for this study. However, in calculating these radiative properties in-house, we are adding a degree of uncertainty to the estimates of the radiative effects of single-layer ice clouds. L'Ecuyer et al. (2015) remarked on the advantages of addressing the differences in radiative flux datasets. By analyzing an assortment of datasets developed based on a variety of spatial resolutions, we can offer a reasonable approximation of the "aggregate effects of structural errors" in each product using inputs from specific sensors and unique radiative transfer models (*L'Ecuyer et al.* 2015). Bearing this in mind, these new calculations also infer the impact that cloud retrievals have on estimating cloud radiative properties. This is particularly crucial since the observed vertical structure of radiative heating by ice clouds is not fully constrained (*Cesana et al.* 2017).

Therefore, the purpose of this work is to provide a broad perspective of the impact that single-layered ice clouds have on the Earth's radiation budget through consideration of their heating rate profiles. Our goal is to generate a global record of single-layered ice cloud physical and radiative properties. In addition, we will composite their heating rate profiles based on cloud and environmental properties typically simulated by GCMs. By relating the computed heating rate profiles to radiatively-dependent components of the

cloud or background environment, we facilitate a treatment of bulk ice cloud properties which can be used in future model development and evaluation efforts in a process-oriented framework.

Global Occurrence Frequency and Ice Cloud Micro-/macro-physical Properties

Single-layered ice cloud pixels are first subset based on the 2C-ICE IWC and 2B-CWC-RVOD (*Austin and Stephens* 2001; *Austin et al.* 2009) liquid water content (LWC) profiles. The IWC/R_e profiles are retained assuming they are vertically continuous with no liquid clouds (i.e., LWC) existing in the column. Additionally, profiles with detectable precipitation, as per the 2C-PRECIP-COLUMN product, are also removed. Figure 35 displays an example of the single-layered ice cloud detection using this definition. Notice that 2C-ICE provides an IWC retrieval for the mixed-phase portion of the cloud (i.e., Figs. 35a and 35b at 58−64 °S and 1−5 km; IWC > ~0.3 g m^{-3}), but it is effectively removed from the subset based on consideration of the 2B-CWC-RVOD LWC (Fig. 35c) profile (grey shaded region from ~64 – 66.5 °S in Fig. 35a highlights the single-layered ice cloud based on this definition). The precipitation detection by 2C-PRECIP-COLUMN also indicates that snow or mixed precipitation (flagged as 4–7, the red horizontal lines in Fig. 35a) is present within the cloud.

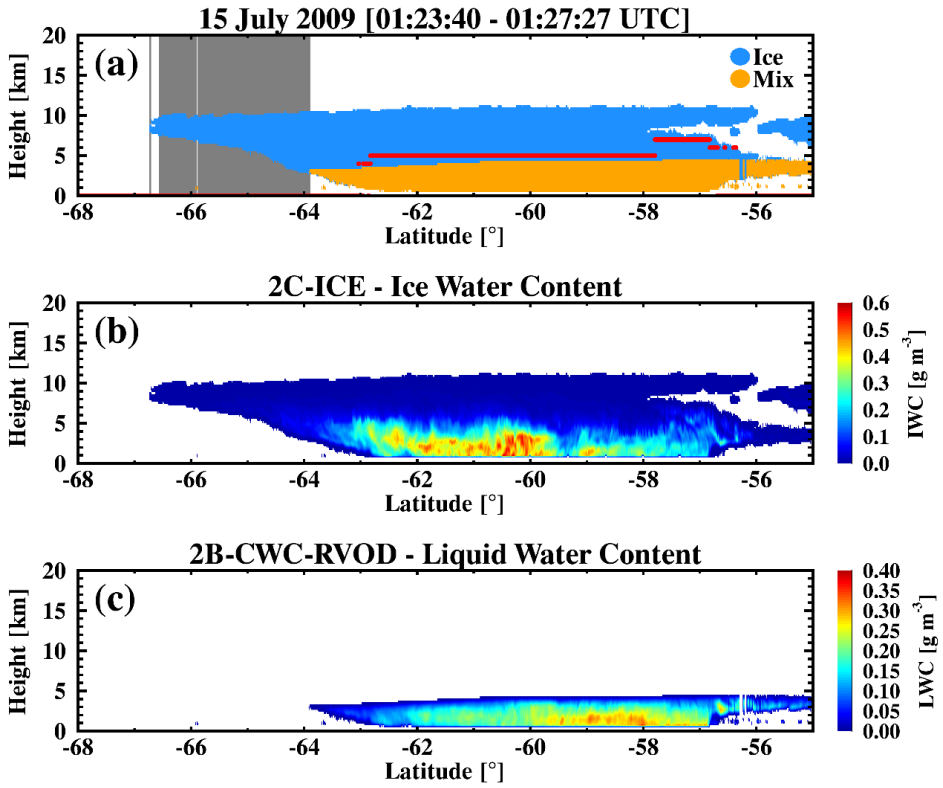

Figure 35: An example of the detection algorithm for single-layered ice clouds on 15 July 2009 over the Southern Ocean. (a) Orange areas correspond to layers of the cloud containing a mix of liquid (from 2B-CWC-RVOD) and ice (from 2C-ICE) while the blue area is ice only. The horizontal red lines correspond to profiles when precipitation is detected by the Cloud Profiling Radar (CPR; 2C-PRECIP-COLUMN). Values indicate what type of precipitation is detected and the certainty of detection [Rain: 1 – possible, 2 – probable, 3 – certain; Snow: 4 – possible, 5 – certain; Mixed: 6 – possible, 7 - certain]. For this cloud system both snow and mixed precipitation were detected (refer to the y-axis). The grey section represents where the algorithm defines single-layered ice clouds used in this study. (b) The 2C-ICE IWC and (c) 2B-CWC-RVOD LWC (g m^{-3}) for the cloud of interest is contoured to showcase that 2C-ICE retrieves not only ice clouds but also the ice of mixed phase clouds.

Based on these simple criteria, the global occurrence frequency of single-layered ice clouds is shown in Fig. 36. Single-layered ice clouds occur most frequently (25– 40%) in the tropical warm pool of the western Pacific, Micronesia, central Africa, and northern

South America, which lines up nicely with the ascent regime defined in Chapter 3. These clouds are relatively infrequent in the Southern Ocean and the oceanic western continental coasts due to the larger frequency of marine (i.e., descent regime). Figure 36b indicates that single-layered ice clouds occur more than ~10% of the time in the tropics at an altitude of 12−16 km. Antarctica also experiences these clouds with considerable frequency near 5 km; polar stratospheric clouds (PSCs) contribute ~15% to the total sample over Antarctica (not shown). The global absolute occurrence frequency is roughly 18% in these data. The occurrence is slightly larger during the nighttime, most notably over Antarctica between 5–10 km and in the tropics above ~15 km (not shown).

The vertical distributions of IWC and R_e effectively determine how solar and infrared radiation interacts with a cloud via scattering and absorption. Before analyzing the radiative properties of single-layered ice clouds, their global micro- and macrophysical properties should first be examined and understood. Since this study bears no restriction on the optical thickness or height of single-layer ice clouds, these properties characterize a variety of ice cloud types (e.g., cirrus, cirrostratus, thick anvil, etc.).

Figures 37a-c depict the global mean averages of 2C-ICE IWP, and vertical profiles of mean IWC and R_e as a function of latitude, respectively. The largest grid box (5° × 5°) average IWPs (65–110 g m^{-2}) occur along mid-latitude storm tracks in the northern and southern Pacific and Atlantic Oceans. The smallest IWPs (< 15 g m^{-2}) are found in regions

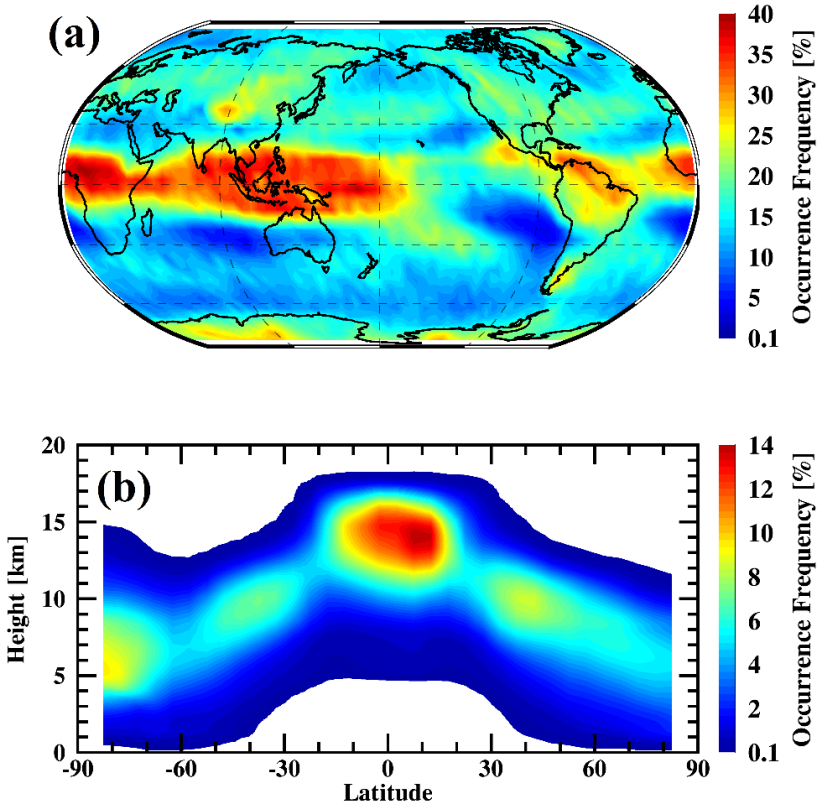

Figure 36: The four-year (2007-2010) global (a) horizontal and (b) vertical occurrence frequency (%) distributions of single-layered ice clouds identified by 2C-ICE. Frequencies are on a 5° × 5° horizontal and 250 m vertical grid. Occurrence Frequency (%) = $(N_{ice\_cld}/N_{total}) \times 100$.

where the occurrence frequency is small, such as the western coasts of Africa, South America, and Australia. The IWP is also quite small in Antarctica despite the relatively large occurrence frequency there (i.e., Fig. 36). The single-layered ice clouds observed in Antarctica are optically thin, enhanced by the contribution of PSCs. The highest IWCs (> ~45 mg m^{-3}) in the mid-latitudes and tropics occur at ~4–8 km. R_e follows a similar pattern to IWC. The largest particles (50–60 μm) occur on average in the tropics and mid-latitudes from ~3–8 km.

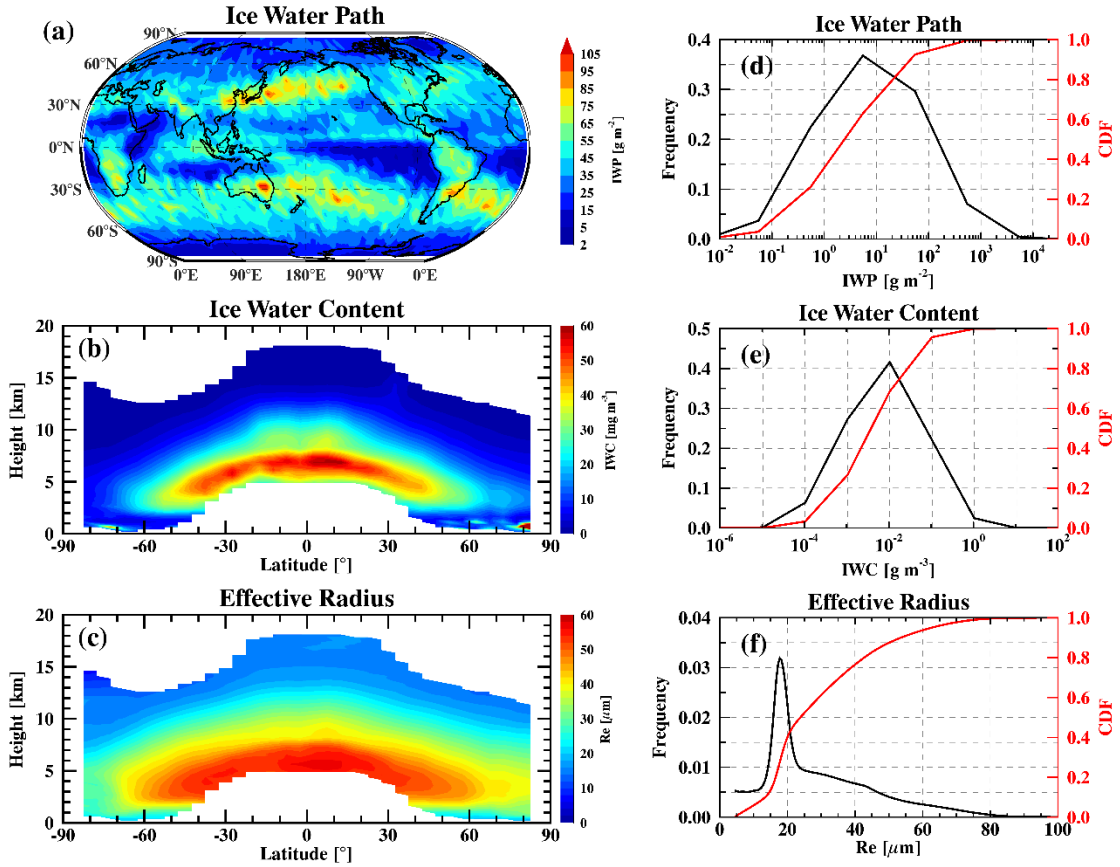

Figure 37: (a) The annual mean global distribution of ice water path (IWP, g m^{-2}) and (b) the latitude-height cross-sections of (b) ice water content (IWC, mg m^{-3}) and (c) effective radius (R_e, μm) for single-layered ice clouds. Vertical cross-sections contain only the cloudy portions of the profile (i.e., IWC > 0.0 g m^{-3} and R_e > 0.0 μm) and when the occurrence frequency is greater than 0.1% (see Fig. 36). The right column shows the frequency and CDFs of pixel-level (d) IWP, (e) IWC, and (f) R_e values. IWC and R_e values are retained only when the R_e > 4.5 μm, which is the lower limit for calculating radiative fluxes for ice clouds in this study.

The IWP/C probability distribution function (PDF) and cumulative distribution function (CDF) are illustrated in Figs. 37d and 37e, based on all available pixel-level ice cloud property retrievals from 2C-ICE. Figure 37d shows that most retrieved IWP fall within a range of 0.1 to 400 gm^{-2} with a mode of 5 g m^{-2}. Approximately 70% of the retrieved IWPs (IWCs) are below 10 g m^{-2} (10^{-2} g m^{-3}) and only ~10% (5%) are above

100 g m^{-2} (10^{-1} g m^{-3}). Therefore, a significant portion of the single-layered ice clouds in this study contains relatively small amounts of ice. The mode of the retrieved ice cloud effective radius is ~18 μm. However, ~10% of the samples are > 50 μm. While the IWC and R_e vertical profiles in Figs. 37b and 37c depict the cloud layer-average values, the PDFs in Figs. 37e and 37f adequately reveal the true ranges of IWC and R_e values.

Figure 38 features the monthly zonal means of cloud-top and cloud-base heights (a – b) and temperatures (d – e) for single-layered ice clouds derived from the 2C-ICE cloud properties and ECMWF-AUX. The highest and coldest cloud-top heights (> 14 km) and temperatures (< 205 K) occur in the tropics during northern hemisphere winter months (DJF) (Figs. 38a and 38d). The ice cloud-top-temperatures (CTTs) over the tropics are just as cold in the Antarctic during local winter, which is consistent with Campbell et al. (2008) and the influence of PSCs. Our results do capture a corresponding increase in ice cloud-top height (~2.75 km) from local summer to winter months in Antarctica. Gridded monthly zonal mean ice cloud-base heights and temperatures can reach as low as ~3.25 km and as high as 253 K.

The ice cloud-top and -base heights over the mid-latitudes appear to have a stronger seasonal dependence compared with the cloud temperatures. For example, the ice cloud-top and -base heights are higher in the northern hemisphere summer months and extend further into the higher latitudes (Figs. 38a and 38b). However, this evolution is not apparent in the cloud temperatures (Figs. 38d and 38e). On average, the tropopause height decreases

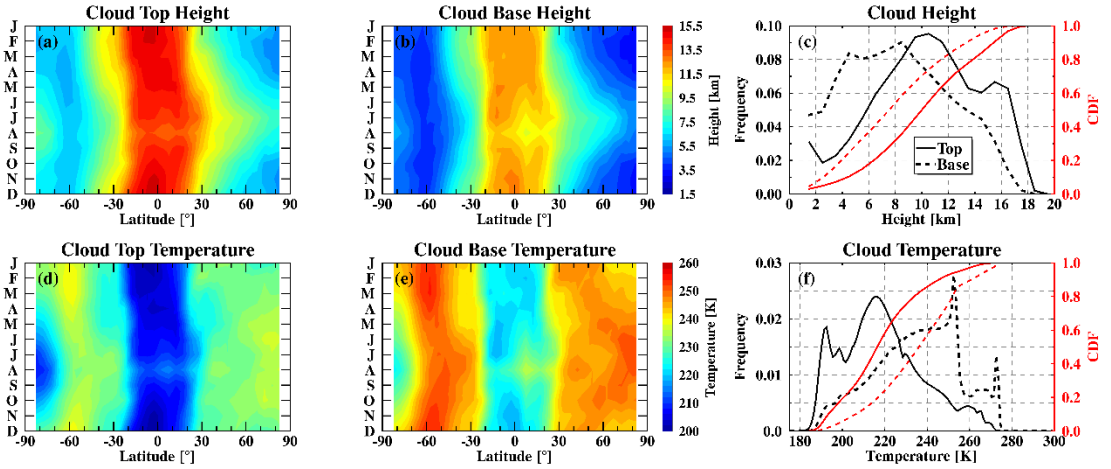

Figure 38: Contoured are the gridded (5° × 5°) monthly zonal means of cloud-top (left) and cloud-base (middle) heights (km, top) and temperature (K, bottom) for single-layered ice clouds. The right column (c,f) shows the frequency (black) and cumulative frequencies (red) of cloud-top (solid) and cloud-base (dashed) heights and temperatures. Height bins are 1 km wide from 1–20 km and the temperature bins are 1 K wide from 175–299 K.

with latitude toward the poles but shifts north/southward with season (i.e., the tropopause height is higher/colder during local summer over the northern mid-latitudes compared to the winter), so it is easy to understand why we do not see a similar change in temperatures (*Nazaryan et al.* 2008).

PDFs of the cloud-top and -base heights and temperatures reveal a multi-modal distribution (Figs. 38c and 38f) for pixel-level ice cloud retrievals. The primary mode of cloud-top height (temperature) at ~11 km likely represents mid-latitude cirrus clouds (~215 K) while the secondary mode at 15 km corresponds to tropical convective outflow or tropical tropopause layer (TTL) ice clouds (~190 K; *Virts and Wallace* 2010). Campbell et al. (2016) reports on the PDFs of daytime single-layered cirrus cloud-top heights observed by the MPL at the Goddard Space Flight Center in Greenbelt, Maryland for one year of

data. Based on their analysis, cloud-top heights range from 6–16 km (for CTT ≤ –37 °C and cloud thickness between 0–5 km) with a peak in the distribution at 11 km. Cloud-tops warmer than 273 K, the approximate upper thermal bound where homogeneous freezing of liquid water dominates and proxy CTT threshold minimum distinguishing cirrus clouds from glaciated clouds in the absence of ancillary evidence aside from lidar measurements (see *Campbell et al*. 2015), represent the impact of glaciated clouds within the bulk cloud sample.

Computed TOA and Surface Radiative Fluxes Compared with Observed Results

Four years (2007-2010) of radiative flux profiles are calculated from the surface to the TOA for every CCCM pixel (with collocated 2C-ICE data) using the input data introduced in Table 11. The radiative flux/heating rate product developed for this study is referred to as D18 (*Dolinar et al.* 2018). The fluxes from two other products, 2B-FLXHR-LIDAR and CCCM_CC, and CERES SSF instantaneous observations are also sampled/collocated for the single-layered ice clouds in this study. Table 11 lists the various input parameters and their source products for the three calculated flux datasets examined in this study.

D18 provides a more robust estimation of the radiative properties of ice clouds when compared to the other two products investigated here. Below is a list of the perceived benefits of the new product. 1) The atmospheric profiles of temperature, ozone, and water vapor, which are required to run the RTM, are extended to higher altitudes (~0.01 hPa as opposed to ~50 hPa), 2) the methods used to develop this product are optimized for ice

clouds, 3) sampling errors are reduced by calculating fluxes and heating rates at finer spatial resolutions, as opposed to the CERES footprint in CCCM_CC, and 4) the parameterized ice cloud properties (R_e and IWC) in 2C-ICE are superior.

Table 11: A summary of the computed radiative flux products assessed in this study. The new fluxes produced for this study are deemed "D18". a – *Henderson et al.* 2013; b – *Kato et al.* 2010 and 2011.

	D18	2B-FLXHR-LIDAR[a]	CCCM_CC[b]
RTM	FLCKKR	BugsRad	FLCKKR
IWC/R_e	2C-ICE	2B-CWC-RO, 2B-TAU, CAL_LID_L2_05km CLay	CloudSat CPR (Revision 4), CALIPSO (V3), MODIS
Meteorology (T, H_2O, O_3)	ECMWF-AUX and MLS	ECMWF-AUX	GEOS-5
Surface Albedo	CERES/MODIS	IGBP	MODIS
AOD	CALIPSO or MERRA-2	CALIPSO Level 2 vertical feature mask	CALIPSO, MOD04, MATCH
Aerosol Type	MATCH	CALIPSO Level 2 vertical feature mask	MATCH
Skin Temperature	ECMWF-AUX	ECMWF-AUX	GEOS-4/-5

Before assessing the differences in heating rate profiles from the three calculated-flux products listed above, we first evaluate the consistency of these calculated fluxes at the TOA and surface with the observed fluxes from CERES and ARM, respectively. Only daytime pixels (solar zenith angle, SZA, less than 90°) are sampled for this analysis.

Four years of instantaneous TOA-reflected SW and outgoing LW radiative fluxes for ice cloudy pixels are shown in Figs. 39 and 41, respectively. The CERES-derived and CCCM_CC calculated SW fluxes at the TOA are very similar in terms of their global means (241.52 and 242.20 Wm^{-2}, respectively, with a RMSD of 12.18 Wm^{-2}; see Table 12) and geographic distribution. Compared with CERES, the calculated TOA reflected SW fluxes from 2B-FXHR-LIDAR and D18 are, on average, too small by 47.07 (19%) and 31.33 W m^{-2} (13%), respectively, with even larger RMSDs and relatively small coefficients of determination (R^2). According to Fig. 39h, the largest discrepancy between the CERES observed and calculated TOA SW fluxes occur in the mid-latitudes (25–35%). By inspection of their globally distributed differences (Figs. 39e and 39f), the large mid-latitude differences seem to be limited to the oceans and Southeast Asia but also over South America, Central Africa, Greenland, and Antarctica in 2B-FLXHR-LIDAR.

Due to the relatively large footprint of CERES (20 km at nadir) and a nearly nadir view (~ 1.4 km) of CloudSat and CALIPSO, it is inappropriate to assume that, based on the methods used here, single-layered ice clouds are the only type found within the CERES footprint. It is well known that low-level marine boundary layer stratocumulus clouds frequently reside in the Southern Ocean and along the western continental coasts. Contamination of highly reflective clouds far removed from the CloudSat and CALIPSO swaths but still within the CERES footprint (and detected by MODIS) are plausibly causing some of the discrepancy in the TOA reflected SW fluxes as shown in Fig. 39e and 39f. In

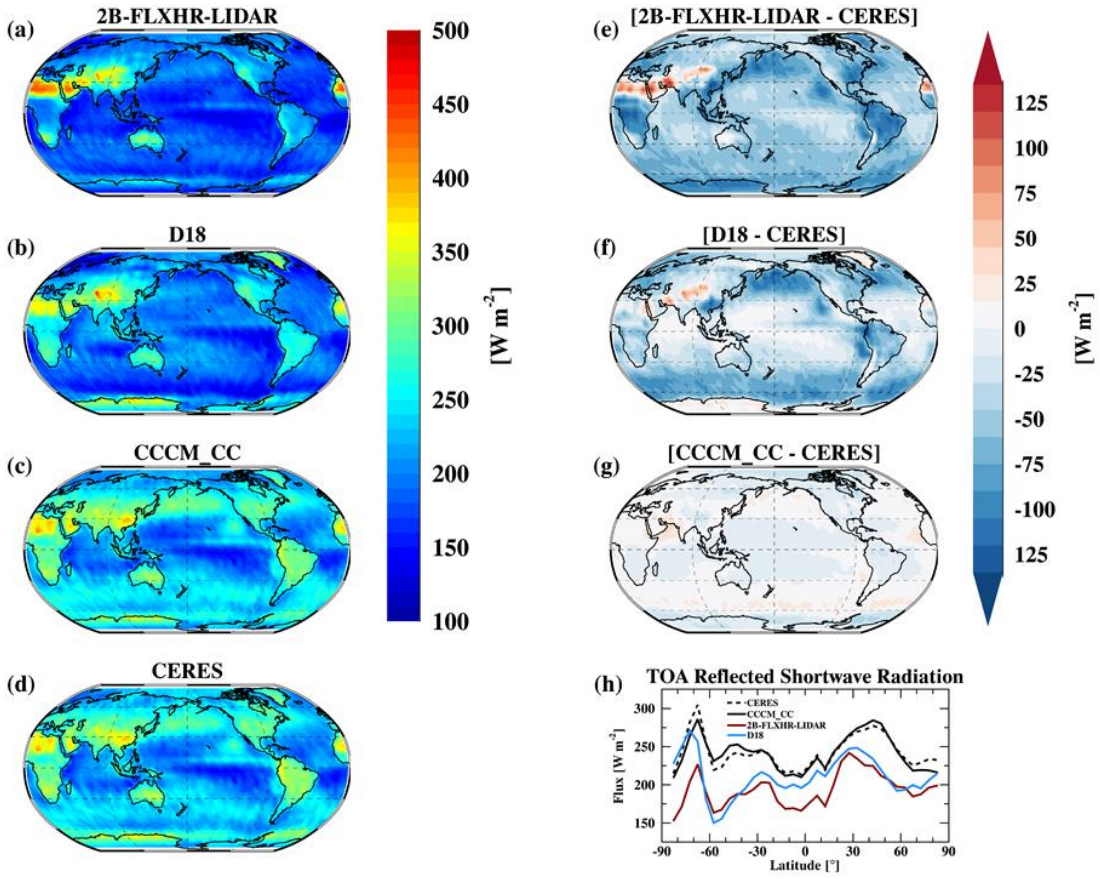

Figure 39: Global maps of the mean TOA reflected SW flux (W m^{-2}) for single-layered ice clouds from (a) 2B-FLXHR-LIDAR, (b) D18), (c) CCCM_CC, and (d) CERES. Corresponding maps of their differences are depicted in (e-g). The zonal means are shown in (h) where the black dashed, black solid, red, and blue lines represent the variations from CERES, CCCM_CC, 2B-FLXHR-LIDAR, and D18, respectively.

fact, the cloud optical depth is larger for the CCCM_CC pixels, especially in the mid-latitudes where the zonal mean is larger by about 2, due to the utilization of MODIS radiances in their algorithm, when compared with the collocated 2C-ICE optical depths (not shown). The distributions of optical depths from 2C-ICE and CCCM show a disparity at the more optically tenuous cloud frequency, where 2C-ICE has ~18% more cloud

samples with an optical depth of < 0.1. Furthermore, based on its algorithm design, 2C-ICE is missing some high-level, reflective thin cirrus clouds (see *Berry and Mace* 2014).

Sensitivity studies, such as the one depicted in Fig. 40, reveal the dependence of TOA reflected SW flux to the mean cloud R_e and SZA. The TOA reflected SW flux relies almost independently of Re at large SZAs. For example, the flux is within 10 W m^{-2} at

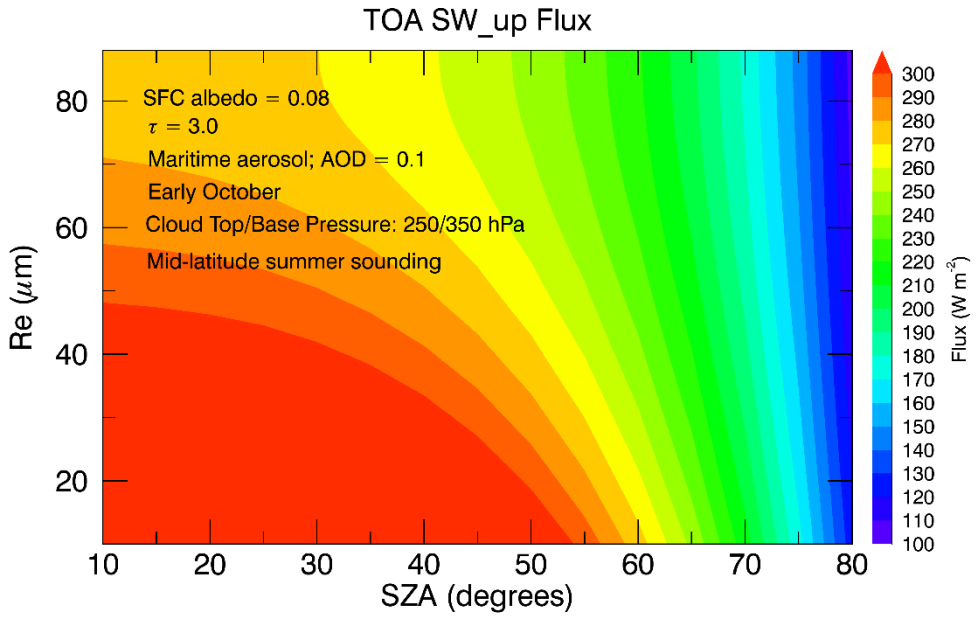

Figure 40: Contours represent the sensitivity of TOA reflected SW flux to solar zenith angle (SZA, x-axis) and the mean ice cloud effective radius (R_e, y-axis). The cloud top- and -base pressures are 250 and 350 hPa, respectively, and the optical depth is 3.0. A marine aerosol is assumed with an aerosol optical depth (AOD) of 0.1 and the surface albedo is 0.08. A typical mid-latitude summer sounding is used in the calculations.

SZA = 80° for R_e ranging from 10–90 μm. The largest gradient in TOA reflected SW flux is when the SZA = 45–55°. Therefore, the most uncertain estimate of TOA reflected SW radiation, caused by the errors or uncertainty in retrieved R_e is when the sun is located

almost directly in the middle of the sky (i.e., between directly overhead and the horizon). For sun-synchronous satellite orbits, instantaneous SZAs in this range occur in the mid-latitudes.

Table 12: Four year (2007 – 2010) weighted global means of the globally gridded (5° × 5°) instantaneous daytime TOA fluxes for single-layer ice clouds calculated by D18, 2B-FLXHR-LIDAR, and CCCM_CC, as well as, the observed fluxes from CERES. Root mean squared differences (RMSD) in W m^{-2}, R^2, and slopes of the linear regression between the calculated fluxes and CERES (all-sky; CCCM_CC for clear-sky).

	TOA SW_up		**TOA LW_up**	
	All-sky	**Clear-sky**	**All-sky**	**Clear-sky**
D18				
Mean	210.19	135.04	222.27	265.00
RMSD	44.64	21.49	7.58	2.09
R^2	0.59	0.94	0.96	1.00
Slope	0.85	1.02	0.88	0.99
2B-FLXHR-LIDAR				
Mean	194.45	115.92	224.98	263.95
RMSD	56.12	26.87	5.64	2.41
R^2	0.64	0.78	0.97	1.00
Slope	0.83	0.82	0.98	0.98
CCCM_CC				
Mean	242.20	118.86	214.57	265.20
RMSD	12.18	-----	14.13	-----
R^2		-----	0.95	-----
Slope	0.92	-----	0.86	-----
CERES				
Mean	241.52	-----	228.73	-----

Global and zonal mean comparisons of the TOA outgoing LW flux are more closely constrained than their SW counterparts. The calculated global mean TOA LW fluxes from 2B-FLXHR-LIDAR and D18 (Figures 41a & 41e and 41b & 41f, respectively) are within

2% of the mean from CERES (Figure 41d) with RMSDs less than 8.0 Wm^{-2} and $R^2 = 0.96$. While CCCM_CC has an even larger, albeit still relatively small, bias (RMSD = 14.13 W m^{-2}), it can be easily explained. Due to an enhanced cloud masking algorithm in CCCM_CC, cloud-top heights (and consequently their infrared emission temperature) are better retrieved and ultimately used in their computations (*Kato et al.* 2011). Therefore, CERES and CCCM_CC provide the upper and lower bounds of the observed TOA outgoing LW flux.

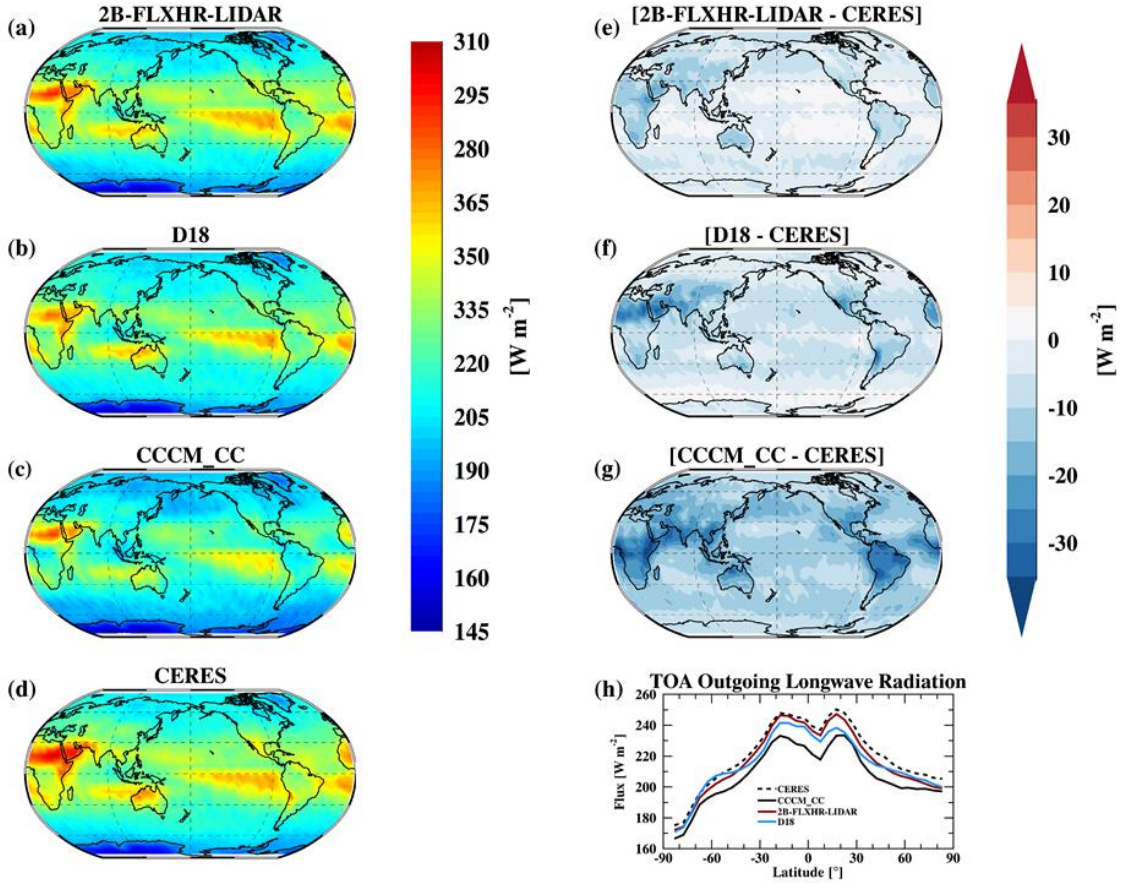

Figure 41: Same as Fig. 39 but for the TOA outgoing LW flux (W m^{-2}).

Passive sensors (i.e., MODIS) operate at an inherent disadvantage in detecting optically thin, relatively cold-topped clouds (*Ackerman et al.* 2008; *Holz et al.* 2016; *Marquis et al.* 2017). As a result, any algorithm using only passive cloud retrievals to study the effects of ice clouds on the TOA radiation may not be adequately represented, especially at the resolution of CloudSat and CALIPSO. In the study by Kato et al. (2011), the TOA LW irradiances for one month of data are examined for CCCM_CC and an algorithm using only MODIS-retrieved cloud properties. They conclude that the TOA outgoing LW flux from CCCM_CC is closer to CERES than the MODIS only product due to the detection limitations of MODIS. Furthermore, the impacts of multi-layered cloud systems on the computed TOA fluxes are also investigated. In a scenario where an optically thin ice cloud overlays a liquid cloud, the difference in OLR can amount to more than 100 W m^{-2} depending on the phase, height, and optical properties of the overlapping cloud system (*Kato et al.* 2011; *Yi et al*. 2017a). This result also supports the point we made in the previous section about how the large CERES footprint may not well represent the CloudSat/CALIPSO swath. In this case, the proximity of lower-level liquid clouds (or the clear-sky) would increase the TOA OLR for individual pixels, and most certainly for a grid box at 5°.

The globally averaged theoretical clear-sky fluxes computed in each product are also provided in Table 12. The clear-sky fluxes are considered theoretical because they are the fluxes computed by the RTM assuming no clouds are present for the sample assembled

in this Section (non-precipitating single-layered ice clouds). Which is also why there are no CERES observed clear-sky fluxes. Any differences in the clear-sky fluxes are assumed to be a result of the different surface and aerosol properties and meteorology profiles used in each product (Table 11), as described in Chapter 4 Section 1. The global means in the clear-sky TOA outgoing LW flux are within 1.25 W m^{-2} between the three products, the RMSDs are less than 2.5 W m^{-2}, and they are well correlated (R^2 = 1.0). Based on the zonal mean TOA clear-sky outgoing LW fluxes in Fig. 42b, there is no discernable difference between the products and regional differences are less than ~15 W m^{-2} (not shown).

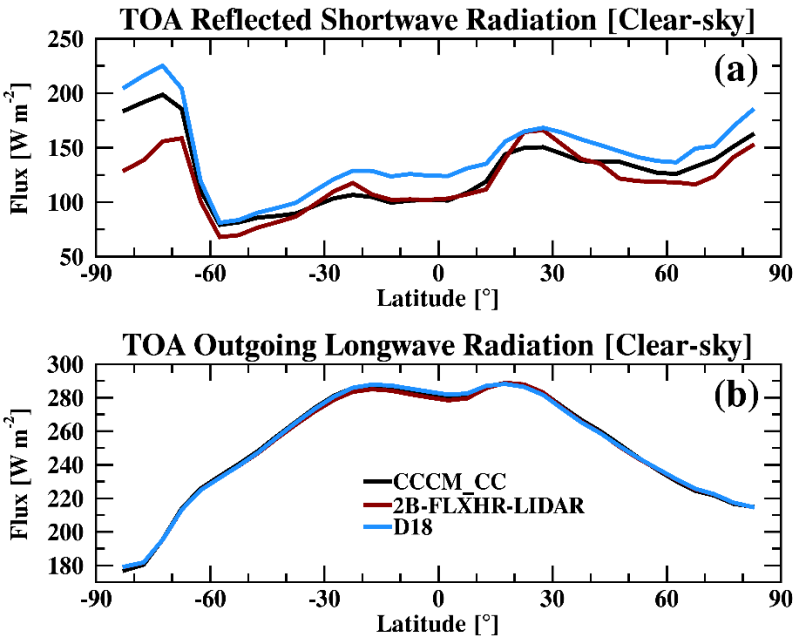

Figure 42: The zonal mean RTM-calculated TOA clear-sky (a) reflected SW and (b) outgoing LW fluxes for four years of data from 2007–2010. Clear-sky fluxes are computed for the corresponding sample of single-layered ice clouds. CCCM_CC, 2B-FLXHR-LIDAR, and D18 results are in black, red, and blue, respectively.

The RTM-calculated TOA clear-sky reflected SW fluxes are not as consistent in these three products. While the global means from CCCM_CC and 2B-FLXHR-LIDAR are within 3 W m^{-2} and the D18 global mean is larger than CCCM_CC by ~17 W m^{-2}, the RSMD of the flux in D18 is actually smaller than 2B-FLXHR-LIDAR by ~5 W m^{-2} and the correlation to CCCM_CC is higher (R^2 = 0.94 vs 0.78). Zonally, the TOA clear-sky SW flux from D18 is larger than CCCM_CC in the tropics (high-latitudes) by nearly 30% (10–15%). The TOA clear-sky SW flux from 2B-FLXHR-LIDAR is too small (10–30%) when compared with CCCM_CC pole-ward of ~30° in both hemispheres. Regional differences in the RTM-calculated TOA clear-sky fluxes can amount to more than 100 W m^{-2} (namely in desert regions and in the Himalayas; not shown).

Computed surface downward SW and LW fluxes are evaluated based on the observed fluxes at three DOE ARM Climate research facilities. Comparing the calculated surface fluxes with the observed ones adds further robustness to the calculated radiative flux profiles investigated further below. If the TOA and surface fluxes agree well with observations, we will have higher confidence in the calculated fluxes within the atmosphere and, more importantly for the in-cloud heating rate profiles. Surface fluxes are based on the observed 10-minute averaged measurements from upward and downward facing Eppley precision spectral pyranometers and infrared pyrgeometers. The calculated instantaneous fluxes are selected for each ARM site assuming they are within a 20 × 20 km^2 box centered at the site.

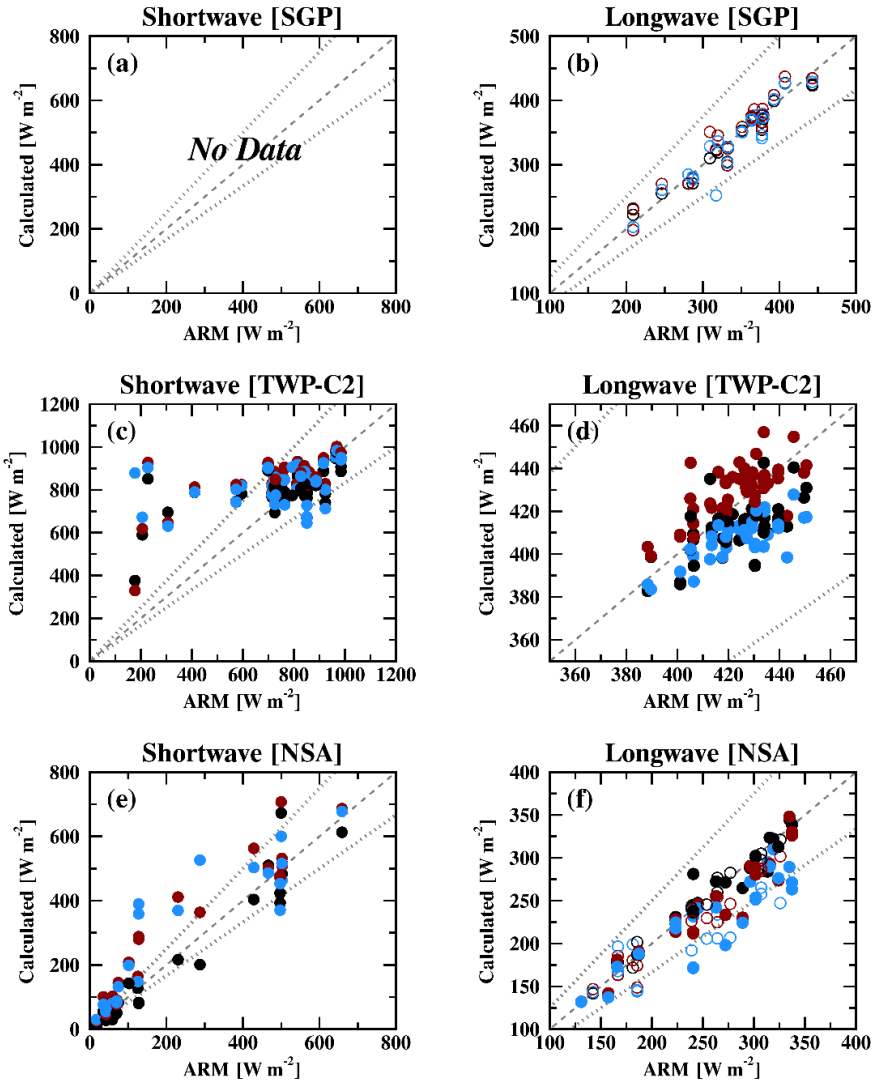

Figure 43: Scatterplots of the calculated downward SW (left) and LW (right) fluxes at the ARM Southern Great Plains (SGP; top), Tropical Western Pacific, Nauru (TWP-C2, middle), and North Slope of Alaska (NSA, bottom) sites. Black, red, and blue symbols correspond to the instantaneous fluxes calculated by CCCM_CC, 2B-FLXHR-LIDAR, and D18, respectively. Open and filled symbols represent fluxes calculated and observed during the nighttime and daytime, respectively. Calculated fluxes are selected when pixels are within 20 km of the ARM site. Each point represents a pixel collocated to ARM. Grey dotted lines represent a ±20% bound to the ARM observed fluxes.

The SGP site has the fewest number of collocated cases with 19, all of which occur during the nighttime. As a result, only the LW fluxes are analyzed. Based on the scatterplot in Fig. 43b, all three data sets show skill in calculating the surface downward LW flux. In fact, their sample means are all within 1% of the ARM mean and with similar standard deviations (see Table 13).

The TWP-C2 site located on Nauru Island yielded 32 cases, all of which occur during the day due to the A-Train overpass configuration (1:30 pm equator transect). Scatterplots of the downward SW flux (Fig. 43c) suggest some persistent errors in the calculated fluxes. On average, the calculated fluxes from D18, 2B-FLXHR-LIDAR, and CCCM_CC are 15%, 17%, and 9%, respectively, greater than the ARM observations (although with very large RMSDs), and their standard deviations are much too small. When the ARM-observed downward SW fluxes are less than ~500 W m^{-2}, the corresponding calculated pixels are significantly too high (up to 700 W m^{-2} too large). The large standard deviation in the downward SW flux in the ARM data also suggests a wide range of cloud optical properties (2C-ICE IWP = 0.05–225 g m^{-2}, although 75% of these IWPs are < 5.0 g m^{-2}). The calculated downward LW fluxes match better with the ARM observed fluxes at TWP-C2; fractional differences are less than 4%.

Finally, a total of 30 pixels (20 daytime, 10 nighttime) were collocated with the NSA site in Barrow, Alaska. The scatterplot in Fig. 43e suggests that the calculated fluxes for optically-thicker single-layer ice clouds, and hence a small surface SW transmission,

are well matched to ARM observations. However, when the downward SW flux from ARM is larger, there is a larger discrepancy. On average, the calculated surface downward SW fluxes from D18 and 2B-FLXHR-LIDAR are more than 50 Wm^{-2} (~20%) greater than the ARM data. The cause of this discrepancy is plausibly due to an improper representation of cloud optical (i.e., too thin or particle size too large) or aerosol properties (i.e., Chapter 4 Section 1). However, assumptions related to ice particle habit and ice particle size distribution in the respective RTMs could also contribute to the bias. The calculated surface downward LW fluxes are underestimated by ~30 (12%) and ~16 (5%) W m^{-2} by D18 and 2B-FLXHR-LIDAR, respectively, with no discernable difference in modeled errors between day and night.

Table 13: The average (σ) surface SW and LW downward fluxes observed at three ARM sites (Southern Great Plains, SGP; Tropical Western Pacific, TWP Nauru, -C2; North Slope Alaska, NSA) and calculated by D18, 2B-FLXHR-LIDAR, and CCCM_CC for non-precipitating single-layered ice clouds from 2007 – 2010.

	D18	**2B-FLXHR-LIDAR**	**CCCM_CC**	**ARM**
Shortwave				
SGP	-----	-----	-----	-----
TWP-C2	830.5 (87.4)	848.0 (117.40)	785.56 (109.06)	734.29 (253.08)
NSA	286.0 (213.4)	294.3 (221.96)	237.27 (216.18)	239.84 (208.27)
Longwave				
SGP	340.60 (61.58)	349.13 (59.78)	342.54 (57.08)	343.39 (57.01)
TWP-C2	407.24 (10.48)	429.39 (13.21)	413.97 (13.33)	423.51 (15.54)
NSA	219.89 (49.71)	235.01 (56.09)	246.54 (62.14)	246.13 (62.34)

Single-layer Ice Cloud Radiative Heating Rate Profiles

The radiative heating rate (Q_r) is a concept of flux divergence with positive (negative) values representing heating (cooling) within a layer. Radiative heating rate profiles are determined from calculated flux profiles as:

$$Qr\ (K\ day^{-1}) = \frac{\partial T}{\partial t} = -\frac{1}{\rho c_p}\frac{dF_{net}}{dz} = \frac{g}{c_p}\frac{dF_{net}}{dp}, \tag{12}$$

where

$$\Delta F_{net} = F_{net}(z + \Delta z) - F_{net}(z) \tag{12a}$$

or

$$\Delta F_{net} = F_{net}(p - \Delta p) - F_{net}(p) \tag{12b}$$

and

$$F_{net}(z) = F^{\uparrow}(z) - F^{\downarrow}(z) \tag{12c}$$

c_p is the specific heat at constant pressure (1004 J kg^{-1} K^{-1}), ρ is the density of dry air (1.225 kg m^{-3}), and g is the gravitational constant (9.80665 m s^{-2}). Since the RTM provides in-cloud fluxes, the in-cloud radiative heating rates can therefore be calculated and resolved.

For example, Fig. 44 shows the retrieved IWC and R_e profiles from 2C-ICE for a single cloud. The IWC and R_e profiles have maximum values of 0.06 g m^{-3} and 60 μm, respectively, near the cloud-base. The resulting LW radiative heating rate profile of this cloud suggests warming (up to ~3.5 K day^{-1}) near the cloud-base and LW cooling near the cloud-top (up to ~ –7.5 K day^{-1}). The dipole of cloud-base warming and cloud-top cooling is generated by the absorption of LW radiation near the cloud-base, enhanced by the surface

LW emission, and LW emission near the cloud-top caused by the warmer CTT than atmospheric temperature above. SW heating rates are positive (up to ~7.0 K day^{-1}) within the cloud due to the absorption of SW radiation reflected from the surface and the direct SW flux from above. The uncertainty in the computed heating rates for individual pixels is estimated and provided in *Dolinar et al*. 2018.

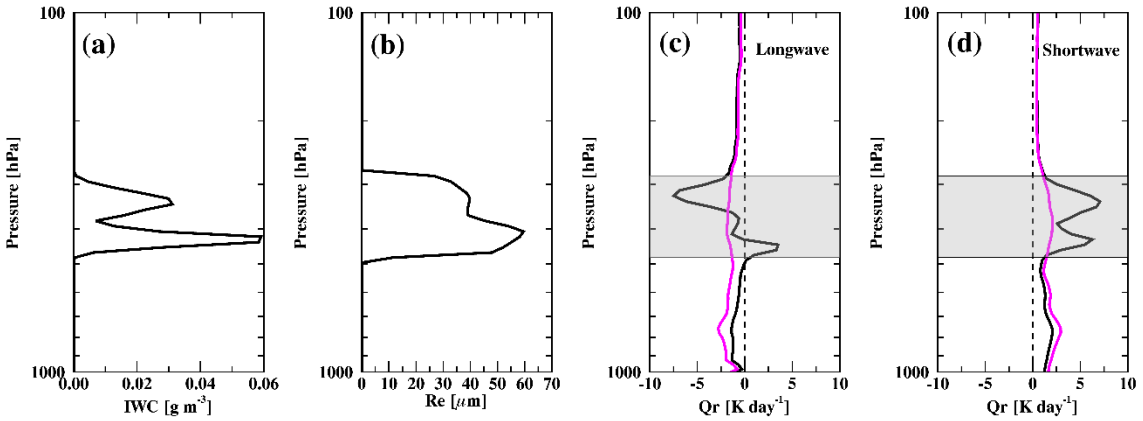

Figure 44: An example of vertical profiles of (a) ice water content (IWC), (b) effective radius (R_e) and their associated (c) LW and (d) SW radiative heating rate (Q_r, K day^{-1}) profiles. Black lines in (c-d) are for the cloudy profile while the pink lines are for the clear-sky. The shaded area in (c) and (d) represent the cloud. This ice cloud profile is taken from 2C-ICE on 4 December 2007 off the western coast of Chile (latitude = –44.3°; longitude = 269.1°; SZA = 36.88°; IWP = 80.9 g m^{-2}; τ = 2.8).

Global Zonally Averaged Radiative Heating Rates

Single-layered ice cloud radiative heating rate profiles are calculated based on retrieved cloud properties (i.e., IWC and R_e) from 2C-ICE at the pixel level over the entire globe and are presented as a function of latitude in Fig. 45. The heating rate profiles based on collocated 2B-FLXHR-LIDAR (Fig. 45 a-c) and CCCM_CC (Fig. 45 g-i) fluxes are also shown. Zonally averaged SW radiative heating rates are positive in all three products with the strongest heating (Q_r > 2.5 K day^{-1}) occurring in the tropics and mid-latitudes.

D18 and CCCM_CC also indicate that the strongest SW warming occurs within the cloud. Enhanced warming of up to 1.5 K day^{-1} is produced above 100 hPa, which is caused by ozone absorption. Figure 45a indicates that the largest inconsistencies in SW radiative heating, as determined by the standard deviation of the three products, lies within the tropical single-layered ice clouds (σ = 0.6–1.1 K day^{-1}).

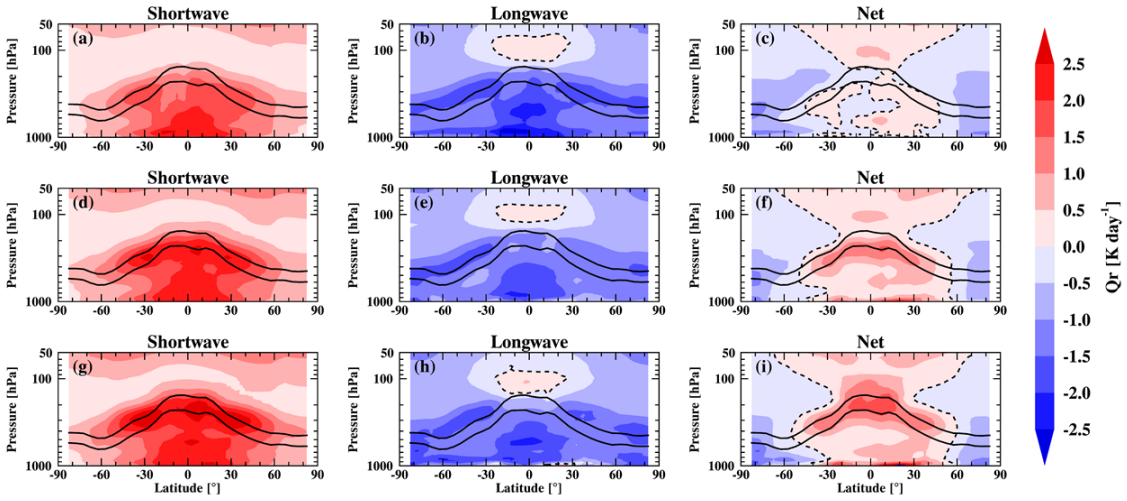

Figure 45: The zonally averaged SW (left), LW (middle), and Net (right) daytime radiative heating rate (Qr, K day^{-1}) profiles for the selected single-layered ice clouds from (top, a-c) 2B-FLXHR-LIDAR, (middle, d-f) D18, and (bottom, g-i) CCCM_CC. The 0 K day^{-1} heating is highlighted with the dashed line and the solid lines represent the zonally averaged cloud-top and -base pressures.

The zonal mean LW heating rates are all negative (i.e., cooling) except for in the tropical upper troposphere. The tropical LW warming (Q_r < 0.5 K day^{-1}) signal is characteristic of cirrus cloud radiative properties (*Ackerman et al.* 1988; *McFarquhar et al*. 2000; *Comstock et al.* 2002; *Mather et al.* 2007). All three products have demonstrated that strong LW cooling of 1.5–2.0 K day^{-1} occurs in the tropical mid- to low-troposphere, as well as, in the mid- to high-latitudes near the cloud-top. Tropical boundary layer LW

heating rates are rather inconsistent among the three products, as the standard deviation amounts to more than ~ 1.0 K day^{-1} (Fig. 46b), which is likely due to differences in land surface temperatures or emissivities used in their respective RTMs.

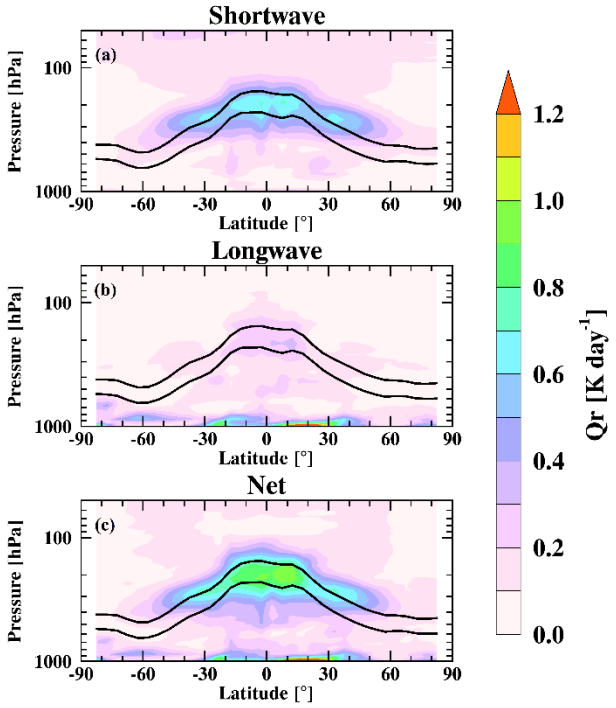

Figure 46: Standard deviations (K day^{-1}) of the zonal mean (a) SW, (b), LW, and (c) net radiative heating rate profiles from the three products (D18, 2B-FLXHR-LIDAR, and CCCM_CC, as in Fig. 45). Black lines are the zonal mean cloud boundaries.

The resulting net radiative heating rates are shown in Fig. 45 (c, f, and i). Tropical net heating rates are generally positive, and strongest within the cloud, due to the relatively strong SW heating that cannot be compensated by the LW cooling generated there. However, the tropical heating rates in 2B-FLXHR-LIDAR are weaker than the other two products, and even suggests weak cooling ($-0.5 < Q_r < 0.0$ K day^{-1}). Nevertheless, a consensus of net radiative cooling is determined for the depth of the troposphere for latitudes poleward of 60°.

Radiative Heating Rates as a Function of IWP

Changes in the cloud radiative heating rate profiles as determined by their IWPs are presented in Fig. 47. On average, the single-layered ice cloud thicknesses range from ~10–420 hPa from the smallest to largest IWPs (black lines in Figure 47). Cloud-top and -base

pressures increase over the range 0.1 < IWP < 5.0 g m^{-2}, while the clouds deepen for IWP > ~50 g m^{-2}. Typically, the magnitudes of the SW/LW/net radiative heating rates near cloud-top are primarily determined by cloud geometric and/or optical thickness (*Ackerman et al.* 1988), as the SW heating and LW cooling rates increase with increased cloud IWP and cloud thickness as demonstrated in Fig. 47.

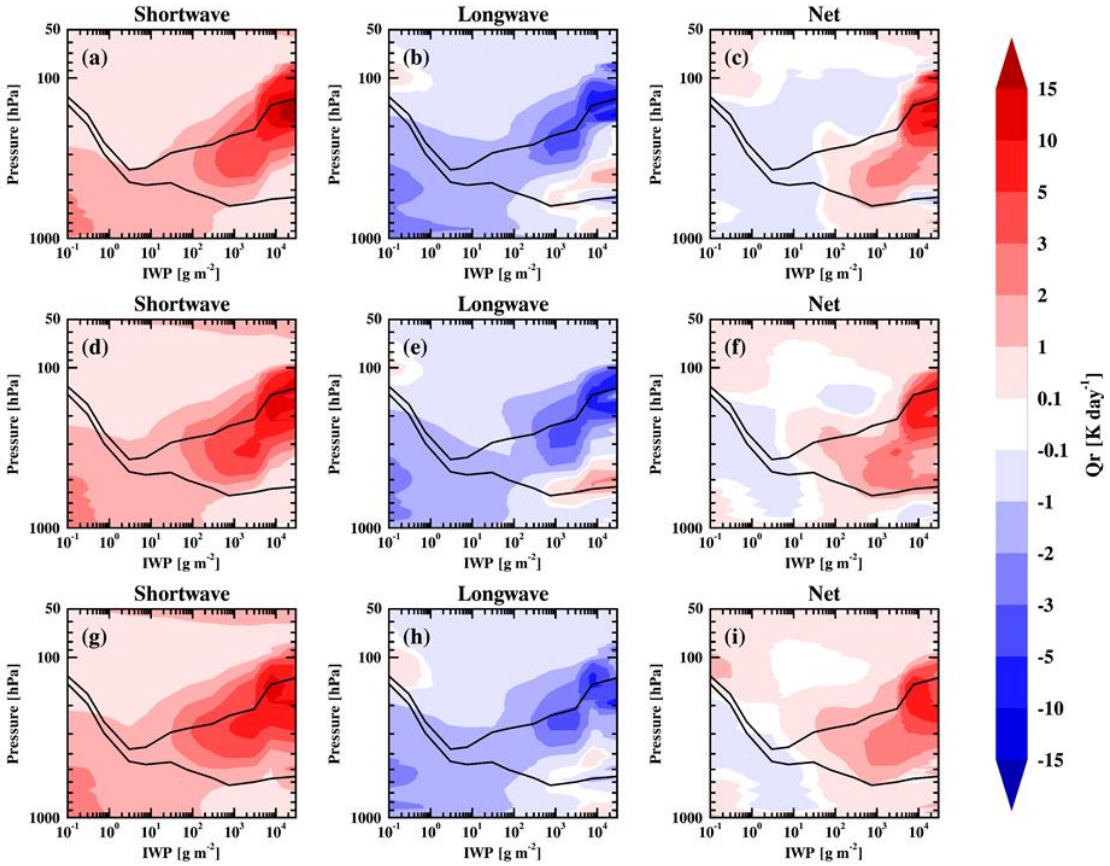

Figure 47: Composites of the SW (left), LW (middle), and net (right) daytime radiative heating rate (Qr, K day^{-1}) profiles for the selected single-layered ice clouds with respect to the 2C-ICE ice water path (IWP, g m^{-2}) distribution for 2B-FLXHR-LIDAR (top, a-c), D18 (middle, d-f), and CCCM_CC (bottom, g-i). Black lines correspond to the average cloud-top and -base pressures. There are seven IWP bins from 0.001 to 10000 g m^{-2}, each increasing by an order of magnitude.

The relatively strong SW heating rates near the cloud-top (due to more absorption of SW radiation) overwhelm the relatively strong LW cooling rates (due to the much colder atmospheric temperature above the cloud-top) effectively inducing net heating rates of more than +5.0 K day^{-1} for the thickest of single-layered ice clouds (IWP > 5000 g m^{-2}), as determined by the 2C-ICE cloud properties, although IWPs greater 5000 g m^{-2} are infrequent < 0.001% (see Fig. 27d). For the thinnest clouds (IWP < 10 g m^{-2}), which are most frequent, LW heating is more significant.

On average, for IWPs > 100 g m^{-2}, the strongest SW heating rates are located at the cloud-top where most of the SW absorption occurs (which is also where the largest discrepancy occurs between the three products, see Fig. 48, σ = 2.5–5.0 K day^{-1}), and then decrease toward the cloud center. Near the cloud-base, the SW heating rates are weak due to the reduction of solar photon penetration. A region of relatively strong SW heating (up to 3.0 K day^{-1}) is seen below ~500 hPa for IWPs < 1.0 g m^{-2} whereas the in-cloud SW warming is < 1.0 K day^{-1}. The enhanced SW heating in the low-levels for small IWPs are likely caused by water vapor absorption.

According to the D18 heating rate profiles in Fig. 47e, a dipole of cloud-top LW cooling and cloud-base LW warming occurs for ice clouds with IWPs > ~600 g m^{-2}. Otherwise the cloud is primarily losing heat/energy through its depth. It is consistent to induce positive LW heating rates at the cloud-base since the cloud absorbs more surface LW emission than it emits. For the same large IWPs, the 2B-FLXHR-LIDAR and CCCM_CC LW heating rates show LW cooling at the cloud-base, but warming just above

and below the cloud-base. The difference between D18 and the other two datasets (σ up to ~2.0 K day^{-1}; Fig. 48b) suggests a variation in vertical cloud structure or differences in parameterized ice cloud properties used in their products. The positive tropical upper level LW heating rates seen in Fig. 45 are associated with IWPs less than 1.0 g m^{-2}. The low-level LW cooling seen in Figs. 45b and 45h are also somewhat depicted in Figs. 47b and 47h (i.e., the enhanced LW cooling rates for 2B-FLXHR-LIDAR and CCCM_CC, respectively). By decomposing the heating rates based on cloud IWP, it becomes clear that these low-level LW cooling rates (up to –3.0 K day^{-1}) are produced by clouds with an IWP of < 10 g m^{-2} according to 2C-ICE, which account for ~70% of the pixels (Fig. 37d).

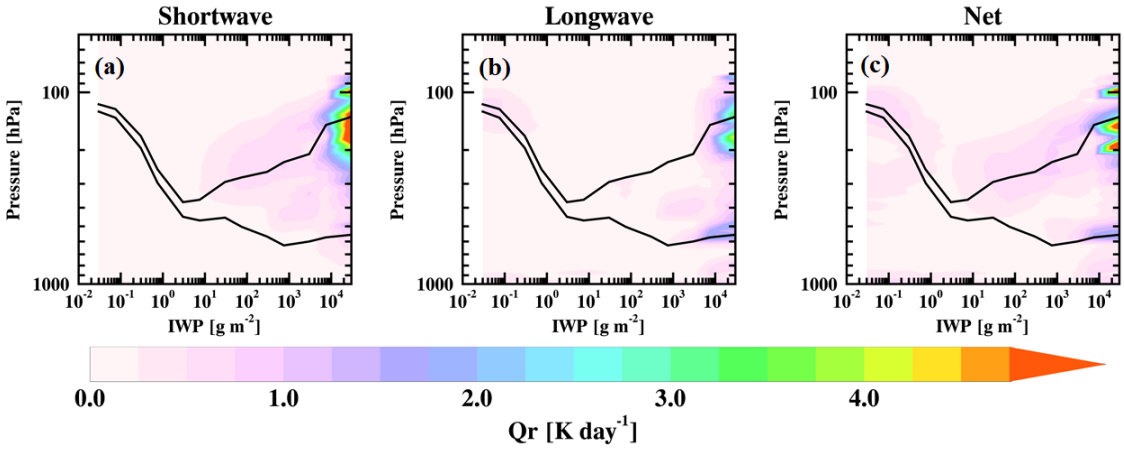

Figure 48: Same as Fig. 46 but showing the standard deviation of the heating rate profiles as a function of the 2C-ICE IWP (g m^{-2}) distribution.

Radiative Heating Rates as a Function of Total Column Water Vapor (TCWV)

Diagnosing cloud radiative heating rate profiles based on water vapor provides a more deterministic view into how ice clouds can be better simulated using convective cloud parameterizations in GCMs. The radiative heating rate profiles are presented as a function

of total column water vapor (TCWV) mixing ratio (g/g) in Fig. 49. The TCWV comes from summing the water vapor mixing ratio profile from the combined ECMWF-AUX/MLS profiles used for computing the D18 heating rate profiles.

Cloud geometric thickness is rather invariant of TCWV, despite the vertical ascent of these clouds as water vapor increases. The coupling of ascending single-layered ice clouds with increasing water vapor increases the efficiency of in- and below-cloud SW absorption and LW emission. Based on these three products, the vertical structure and magnitude of these competing absorption and emission properties makes for unique net heating rate profiles, especially at larger TCWV.

Figures 49c, 49f, and 49i show that the three products agree that there is net cooling through much of the atmosphere for TCWV < ~0.1 g/g and is maximized within or below the cloud. However, the vertical structure of net heating rates for TCWV > 0.1 g/g is significantly different between D18 and CCCM_CC. The heating rate profiles in D18 (Fig. 49f) suggest net cooling within the cloud due to the strong LW cooling (up to 5.0 K day^{-1}) and relatively weak SW warming. Furthermore, the net radiative heating rates in D18 above and below the cloud layer result from the relatively strong SW heating below the cloud layer and slight LW warming (due to tropical cirrus) above the cloud layer. While CCCM_CC does generate the positive above- and below-cloud net heating for TCWV > 0.1 g/g, it depicts appreciable positive net heating (> 5.0 K day^{-1}) within the cloud as well.

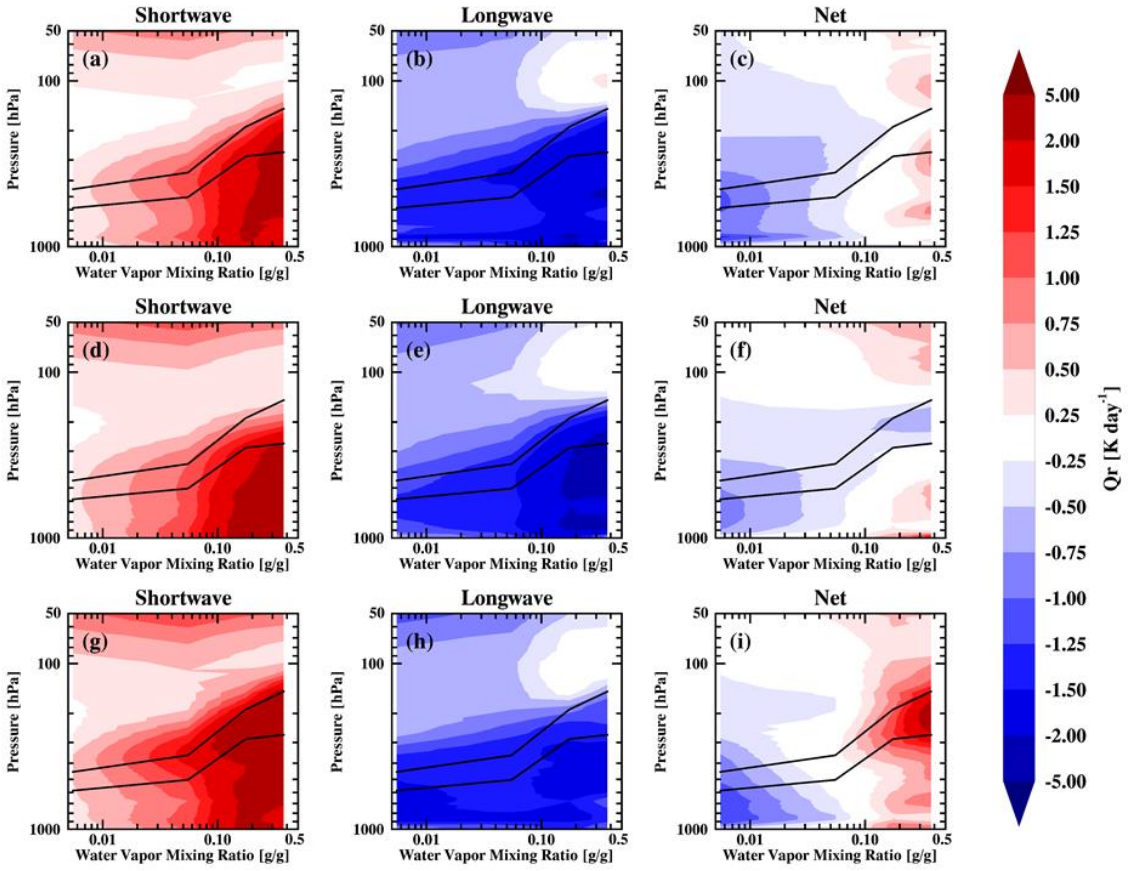

Figure 49: Same as Fig. 47 but the heating rate profiles are a function of the total column water vapor (TCWV) mixing ratio (g/g) from the ECMWF/MLS profiles used in calculating the D18 fluxes. The water vapor bins are irregular at [0.001,0.01,0.1,0.25, and 0.5] g/g.

While there are some inconsistencies between the three products in their estimation of in-cloud LW heating rates at large TCWV ($\sigma < 0.25$ K day^{-1}, Fig. 50), the discrepancies in SW heating are more alarming. At this time, the exact cause of this discrepancy is unknown. However, we can speculate that the retrieved cloud properties used in CCCM_CC are vastly different than in 2C-ICE; the clouds at higher TCWV, as per

ECMWF/MLS, must be optically thicker in CCCM_CC to induce such a positive net warming.

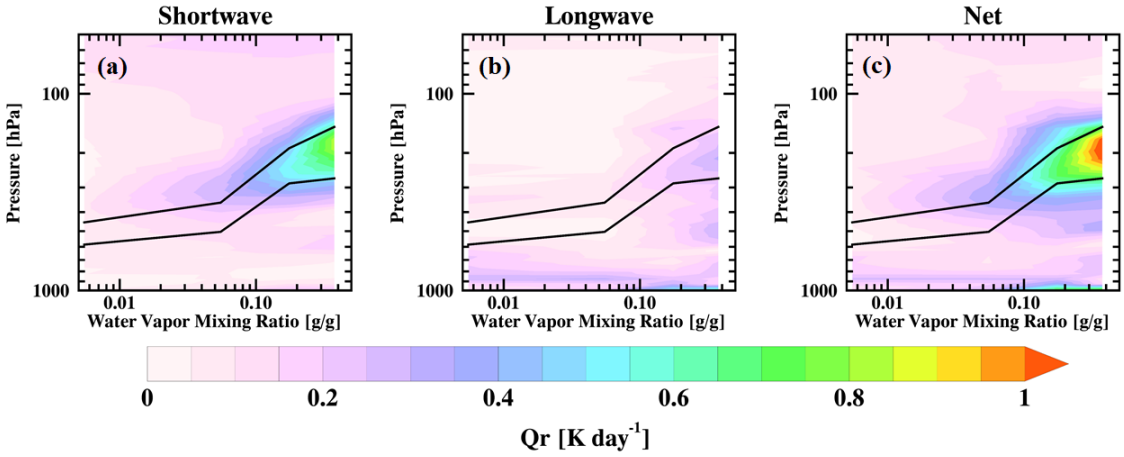

Figure 50: Same as Fig. 46 but showing the standard deviation of the heating rate profiles as a function of the ECMWF-AUX/MLS total column water vapor (TCWV, g/g) distribution.

Radiative Heating Rates as a Function of Solar Zenith Angle (SZA)

To further assess the differences in heating rate profiles from the three data sets, we present the SW, LW, and net cloud heating rate profiles as a function of the instantaneous solar zenith angle (SZA) encountered with the sample throughout the experiment. Figure 51 highlights that the cloud geometric thickness is invariant of SZA and that single-layered ice clouds descend to higher pressure from small to large SZA, which corresponds with the transition from tropical to high latitude data points in the sample and consistent with Fig. 45. Figure 51 also shows that the strongest SW warming (> 5.0 K day^{-1}) occurs when the sun is most directly overhead (SZA < 30°).

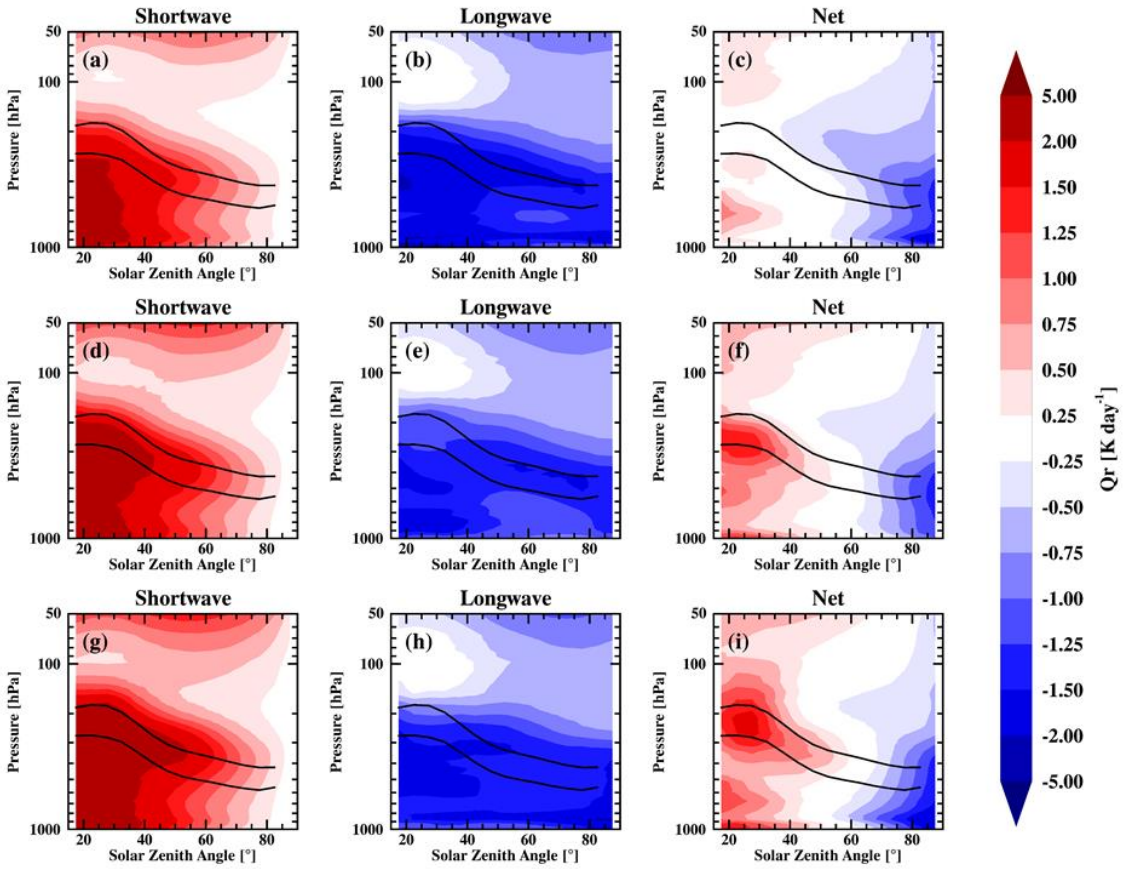

Figure 51: Same as Fig. 47 but the heating rate profiles are a function of solar zenith angle (SZA, degrees). SZA bins are five degrees wide from 15 – 90 degrees.

All three data sets have demonstrated that the magnitude of SW radiative heating rates decreases with increased SZA. Since the A-Train follows a sun synchronous orbit with an equator overpass at ~1:30 pm, the previously mentioned tropical upper-level LW warming feature is seen for low SZAs (< 30°). LW cooling is maximized below the cloud for SZAs < 40° and within the cloud for larger SZAs. The LW cooling rates in 2B-FLXHR-LIDAR (Figure 51b) and CCCM_CC (Figure 51h) also suggest the contamination of low-level clouds in their products. The net heating rates in Figs. 51c, 51f, and 51i show a

consensus that radiative warming is maximized within the cloud when the sun is most directly overhead and comparatively strong cooling occurs within and below the cloud for larger SZAs (> 50°). Based on their standard deviations, the heating rates as a function of SZA are within < 1.0 K day^{-1} (not shown) from the three products.

Summary of Chapter IV

This Chapter focused on running the Fu-Liou RTM for clear-sky scenes at specific locations (ARM SGP, NSA, and TWP-C3 sites) and globally for single-layered ice clouds. In Section 1, MERRA-2 clear-sky vertical profiles of temperature, ozone mixing ratio, and water vapor mixing ratio are evaluated at three ARM sites from August 2004 to December 2013. These meteorological profiles are used as input to the RTM to perform a clear-sky radiation closure study at the surface and TOA. Based on the results presented in Section 1, the following conclusions can be made.

1) Vertical profiles of temperature at the three sites are well replicated in MERRA-2 when compared with the newly generated satellite/surface-based (hybrid) data set. Even the characteristic low-level temperature inversion of the Arctic is captured in the reanalysis. Since MLS ozone is directly assimilated, the MERRA-2 ozone mixing ratios are very close to the hybrid profiles at all three ARM sites. Finally, the MERRA-2 tropospheric water vapor mixing ratios are, on average, on the drier side of the hybrid data at the ARM SGP and NSA sites for snow-free conditions. However, the relatively small and constant tropospheric water vapor profile at the ARM NSA site for the snow cases is well replicated in MERRA-2. At TWP-C3, the MERRA-2 water vapor profile is drier than the ARM-merged sounding by ~10–30%, on average, except between ~850 and 750 hPa.
2) The clear-sky surface and TOA radiative fluxes are calculated using the NASA Langley-modified RTM (with the same surface characteristics) with inputs from

hybrid, MERRA-2, and climate mean profiles at the three ARM sites. In this radiative closure study, the calculated SW fluxes are tuned by adjusting the surface albedo, and by including a secondary aerosol, to reduce the differences between the averaged calculated and observed fluxes. As expected, the surface and TOA LW fluxes show little sensitivity to the change in surface albedo and aerosol characteristics; therefore, a different method of adjustment is necessary for achieving radiative closure for LW fluxes. We recommend tuning the surface skin temperature as a means for reducing the difference between the calculated and observed LW fluxes. The averaged flux differences (calculated minus observations) using the hybrid and MERRA-2 profiles at three ARM sites are generally < 5 W m^{-2}, while the calculated fluxes from climate mean profiles are typically larger biased. Although the averaged tuned calculated fluxes are relatively close to the observed means, large compensating errors are evident. Therefore, we can conclude that the input of accurate atmospheric profiles and surface characteristics in the RTM plays an important role in calculating the surface and TOA clear-sky SW and LW fluxes.

3) Errors in the clear-sky surface and TOA fluxes can as large as 30–40 % if the correct surface characteristics are not used in the RTM. Therefore, errors in the calculated fluxes when clouds are present could be just as large (or larger) if improper surface properties are used and barring and errors in the retrieved cloud properties.

The active sensors on CloudSat and CALIPSO provide global measures of the vertical structure of ice clouds and have proven to be invaluable for studying and subsequently

providing better constraints of their radiative effects. In Section 2, vertically-derived cloud properties are used to calculate the radiative heating rate profiles of single-layered ice clouds. Using the cloud properties derived from 2C-ICE, we generate an independent product of SW and LW heating rate profiles and compare them to the ones from the 2B-FLXHR-LIDAR and CCCM_CC products. Based on this study, the following conclusions can be made:

4) The global occurrence frequency of non-precipitating single-layered ice clouds (with no underlying liquid clouds present) is roughly 18% with considerable occurrence (> 25%) in the tropical western Pacific warm pool and central Africa above 12 km. The largest IWP/C and R_e occur over the tropics and mid-latitudes along oceanic storm tracks. Single-layered ice clouds are relatively high in altitude and cold, as 50% of the cloud samples have cloud-top heights above 10 km and cloud-top temperatures below 215 K. Based on the PDFs of CTT, it is evident that different types of cloud ice exist the in subset and should be uniquely handled in the radiative transfer model (i.e., cirrus [CTT ~210 K] and glaciated ice [CTT ~260 K]).
5) Computed TOA and surface fluxes from three independent products are compared with satellite and ground-based equivalents to assess consistency and uncertainty. We generate our own radiative flux profiles (D18) using the retrieved single-layered ice cloud microphysical properties from 2C-ICE, while 2B-FLXHR-LIDAR and CCCM_CC use retrieved cloud information from a merged CloudSat,

CALIPSO, and MODIS product. According to their global means, the D18 and 2B-FLXHR-LIDAR TOA reflected SW fluxes for daytime single-layered ice clouds are too small by 13–20% compared to CERES and an appreciable large negative bias (25–35%) is found in the mid- and high-latitude oceans. However, the calculated TOA outgoing LW fluxes are mostly consistent (global means are within 8.0 W m^{-2}) with CERES satellite observations. Instantaneous calculated surface fluxes are collocated with observed radiative fluxes at three ARM Program sites (SGP, NSA, and TWP–C2). Computed surface downward LW fluxes at the three ARM sites are generally well matched with the observed fluxes given the relatively small sample size (a total of 81 samples). The downward SW fluxes at the surface, on the other hand, show a considerable positive bias (e.g., > 100 [50] W m^{-2} for D18 at the TWP-C2 [NSA] site).

6) Daytime cloud radiative heating rate profiles are calculated with the inputs of 2C-ICE ice cloud microphysical properties. Based on their zonal means, the strongest SW heating rates occur within the cloud in the tropics and mid-latitudes in all three data sets where IWC and R_e are largest on average. However, considerable SW warming also extends to the surface in the tropics. Relatively strong LW cooling rates also occur in the tropics below the single-layered ice cloud and mid-latitudes just above the cloud. In general, the patterns of SW heating and LW cooling rate profiles from three datasets are similar to each other with slight differences in magnitude. High-latitude net radiative cooling is determined due to the high SZAs,

lower and warmer cloud-bases, and small IWPs. 2B-FLXHR-LIDAR is unique in that it produces much weaker net warming and/or net cooling rates in the tropics.

7) Daytime cloud radiative heating rate profiles are composited based on the 2C-ICE IWP, ECMWF-AUX/MLS TCWV mixing ratio, and SZA. Decomposing the heating rate profiles in this way provides more detail about how heating rates vary with retrieved cloud and environmental properties, but can also serve as a process-oriented diagnostic tool used for evaluating and improving convective parameterizations. Cloud-top SW (LW) warming (cooling) is coupled with cloud-base LW warming for the largest IWPs (> 300 g m^{-2}). In general, the magnitudes of SW/LW/net radiative heating rates near the cloud-top are primarily determined by cloud geometric and/or optical thickness (i.e., IWP), as the SW heating and LW cooling rates increase with increased cloud IWP and cloud thickness. Considerable cloud net warming is determined for the largest IWPs and TCWV, and smallest SZAs within the cloud. An upper level LW warming feature is consistently produced for tropical cirrus clouds where IWPs are smaller (< 1.0 g m^{-2}), TCWV mixing ratios are large (> 0.1 g/g), and SZAs are small (< 30°).

CHAPTER V

DISCUSSION, CONCLUSIONS, AND FUTURE WORK

The simulated cloud properties (cloud fraction, CF and cloud water path, CWP) and radiation budgets from 28 global climate models (GCMs) and five contemporary reanalyses are evaluated against consistently observed properties from satellites and ground-based sensors for multiple years of data. Based on the comparison with passive satellite sensors, such as the Moderate Resolution Imaging Spectroradiometer (MODIS), the simulated global CF is too small, on average, by 7%. The estimated bias in CF from the 33-member model mean is even larger (16%), when compared with the active sensors on CloudSat and the Cloud-Aerosol Lidar Infrared Pathfinder Satellite Observation (CALIPSO). The bias is larger when compared to active sensors because they are more sensitive to optically thin clouds ($\tau < 0.3$), which suggests a consistent model deficiency in simulating optically thin clouds. While some studies suggest a complementary bias in the optical thickness of clouds, where the lack of clouds in model simulations is compensated by generating clouds that are too optically thick (e.g., *Kay et al.* 2012), this evaluation study uncovers that the cloud water path (CWP), which is used as a proxy for optical depth, is also underpredicted by the multimodel mean by roughly 17 g m^{-2} when compared with MODIS observations.

Based on the 33-member ensemble of GCMs and reanalyses analyzed here, the simulated TOA radiation budgets and CREs match well with satellite estimates from the Clouds and Earth Radiant Energy System (CERES) Energy Balanced and Filled (EBAF).

Biases in the global mean all-sky and clear-sky TOA shortwave (SW) and longwave (LW) fluxes are less than 2 W m^{-2}, which is within the uncertainty of the satellite measurements and the standard deviation of the simulated results. The resulting simulated global mean TOA CREs are within 3 W m^{-2} when compared with CERES and suggests a stronger net cooling effect. Our analysis further confirms that radiation fields are tuned in global models to better match observations.

The cloud and radiation fields are then analyzed for two regimes, defined by the vertical velocity at 500 hPa (ω500). While the CFs in both regimes are similar (69 vs 66%), the CWP is larger in the ascent regime (ω500 < –25 hPa day^{-1}) due to the existence of deep convection in these regions. The corresponding radiation fields are consistent with their regime-averaged cloud properties. For example, the net CRE is stronger in the descent regime (ω500 > 25 hPa day^{-1}) due to the relatively weak LW warming effect induced by the marine boundary layer clouds that exists there. In general, the multimodel mean produces too many (few) clouds with too much (little) cloud water in the ascent (descent) regime, resulting in a stronger (weaker) net CRE. While the biases in the ascent regime are smaller than in the descent regime (e.g., CF bias = 1.1 vs. 18%), they are not as well correlated to the satellite observations (CF correlation, r = 0.35 vs. 0.50).

While the CMIP5 GCM simulated cloud and radiation fields have been evaluated in other studies, Chapter 3 provides a more comprehensive assessment of the CMIP5 and reanalysis simulations using multiple satellite observations. More importantly, we have

investigated the impact of CF and CWP on the TOA radiation fluxes and CREs, quantitatively estimated the sensitivities of SW/LW CREs on CF and CWP in strong atmospheric ascent and descent regimes, and have performed a detailed error analysis. For example, the sensitivities (determined by linear regression) of the LW CRE to CF in the ascent and descent regimes are different. The ascent regime is more sensitive (0.82 vs 0.23 W m^{-2} $\%^{-1}$) due to the wider range of cloud-top temperatures (CTT) of cumulus and deep convective clouds. Based on the analysis of error, we conclude that the amount clouds (i.e., CF), or the sensitivity of CREs to CF, has a larger impact on the errors in simulated CREs, in comparison to CWP. These results will provide a better means of representing the true physical interactions between clouds and TOA radiation budgets and will help modelers to better predict future climate scenarios. It is our hope that these comparisons and the statistical results from this study may aid in the advancement of the GCM simulations of clouds and TOA radiation budgets in future versions of CMIP.

Since the CREs are defined as the impact of clouds on the Earth radiation budget in reference to the clear-sky, it is critical to correctly observe and simulate the clear-sky radiation budget. Studies have shown that computing clear-sky radiative fluxes are strongly dependent on atmospheric state variables, such as temperature and water vapor profiles, and surface properties (e.g., albedo). In Chapter 4 Section 1, we evaluate the Modern-Era Retrospective Analysis for Research and Applications version 2 (MERRA-2) reanalyzed clear-sky temperature and water vapor profiles with newly generated atmospheric profiles from Department of Energy Atmospheric Radiation Measurement (ARM)-merged

soundings and Aura Microwave Limb Sounder (MLS) retrievals at three ARM sites. The temperature profiles are well replicated in MERRA-2 at all three sites, whereas tropospheric water vapor is slightly dry below ~700 hPa.

These profiles are then used to calculate clear-sky surface and TOA radiative fluxes from the Langley-modified Fu-Liou radiative transfer model (RTM). To achieve radiative closure at both the surface and TOA, the ARM-measured surface albedo and the aerosol optical depths (AODs) are adjusted to account for surface inhomogeneity (120×120 km^2 centered at the ARM sites). The surface and TOA LW fluxes show little-to-no influence on the surface albedo and aerosol characteristics; therefore, some other method of adjustment is necessary for achieving radiative closure for LW fluxes. We suggest tuning the surface skin temperature as a means for reducing the difference between the calculated and observed LW fluxes. In general, most of the averaged RTM-calculated surface downward and TOA upward SW and LW fluxes agree within ~5 W m^{-2} of the observations, which is within the uncertainties of the ARM and CERES measurements. Yet still, further efforts are required to reduce the bias in calculated fluxes in coastal regions.

Chapter 4 Section 2 provides a global database of single-layered ice clouds (from CloudSat and CALIPSO) and useful metrics for diagnosing errors in simulated ice clouds in the form of radiative heating rate profiles as a function of different cloud and environmental states from three independently produced products. For example, the strongest net heating rates ($Q_r > 2$ K day^{-1}) occur for tropical upper-tropospheric single-layered ice clouds where the ice water path (IWP) is largest (IWP > 100 g m^{-2}). The range

of TOA and surface radiative fluxes and heating rate profiles of single-layered ice clouds are assumed to be the result of different RTMs used (and their subsequent parameterization assumptions regarding ice particle habit and particle size distribution, PSD), input data (which includes different methods for retrieving cloud microphysical properties, IWC and R_e), and the difference in sampling area (*L'Ecuyer et al.* 2015). Furthermore, the uncertainties in computed radiative flux profiles resulting in different ice models used in parameterizing cloud optical properties and in the cloud retrievals themselves should be acknowledged. Since this study does not match the parameterized ice models used in cloud retrievals and in the RTM, some large differences in the computed radiative fluxes can occur (~16 W m^{-2} in the TOA SW ice CRE; *Yi et al.* 2017).

Chapter 3 clearly demonstrates that systematic biases occur in global models when simulating clouds and their impact on the radiation budget. While there are a number of reasons for the discrepancy between simulations and observations, one of them lies within the observations themselves. Satellite observations have limitations. For example, passive sensors are unable to detect optically thin clouds ($\tau < 0.3$) while active sensors can. If cloud parameterization schemes are developed using only passive data, they will show difficultly in simulating optically thin clouds, which is a daunting thought, as cirrus clouds (often optically thin) are estimated to cover ~40% of the Earth (*Mace et al.* 2009).

Figures 4 and 5 show that the simulated CF is too high in the tropics (which is where single-layered ice clouds occur most frequently, Fig. 36) when compared with CERES MODIS but too low compared with CloudSat/CALIPSO. Furthermore, based on

the correlation and standard deviation statistics in Fig. 20, convective-type (including ice) clouds are more problematically simulated in global models in comparison to marine boundary-layer stratocumulus. Therefore, a better treatment of these types of clouds is needed in global models. Chapter 4 provides the optimal data, from a combination of CloudSat and CALIPSO retrievals, required to develop better parameterizations for clouds that typically form due to convection.

There is at least one avenue of future work that one could pursue in reference to the studies completed here. Since GCMs produce simulations of cloud and environmental properties for large areas (grid size of > 3° in some models, see Table 1), the sub-grid scale variability is not resolved. This is a limiting feature of GCMs, as cloud and environmental properties are non-homogeneous, especially at large spatial and temporal scales. The radiative properties of clouds are computed based on inferred cloud-overlap assumptions, as well as, grid-mean microphysical properties. However, in Figs. 46 and 48, we demonstrate that ice cloud radiative heating rates vary based on distributions of IWP and TCWV, respectively. Therefore, GCMs are not appropriately resolving radiation for large grid-boxes, especially when the environment is not homogenous or normally distributed. We recommend that an experiment be developed to test the impact of using a distribution of cloud and environmental parameters for the calculation of radiation in GCMs.

Lastly, as I transition to my post-Doc appointment at the U.S. Naval Research Laboratory (NRL), we will address the issues related to inconsistent ice models used in the parameterization of cirrus cloud microphysical and optical properties. I, along with other

NRL scientists, will be developing a consistent model for cirrus clouds based on MODIS and CALIPSO using parameterizations from Dr. Ping Yang. This new parameterization will be applied to global models, such as the Navy Global Environmental Model (NAVGEM), and for studies related to estimating the TOA CREs of cirrus clouds (i.e., *Campbell et al.* 2016).

APPENDIX

APPENDIX A

A list of the clear-sky cases in Chapter 4 Section 1

SGP			NSA		
Year	**Julian Day**	**Time (UTC)**	**Year**	**Julian Day**	**Time (UTC)**
2004	269	08:37	2005	078	22:23
2004	249	08:36	2005	146	13:52
2005	015	08:35	2005	206	22:22
2005	022	19:45	2006	168	22:31
2005	102	19:44	2006	190	13:49
2005	134	19:44	2007	036	22:27
2005	159	08:35	2007	040	13:57
2005	175	08:34	2007	043	22:33
2005	191	08:34	2007	059	22:33
2005	287	08:35	2007	161	13:50
2005	335	08:35	2007	168	13:56
2005	342	19:45	2008	007	22:24
2006	057	19:45	2008	039	22:23
2006	178	08:37	2008	059	13:52
2006	201	19:48	2008	347	13:51
2006	242	08:39	2009	020	13:59
2006	290	08:39	2009	080	22:30
2006	338	08:38			
2006	345	19:48			
2007	028	19:48	**TWP-C3**		
2007	220	19:48	**Year**	**Julian Day**	**Time (UTC)**
2007	293	08:38	2006	244	16:55
2007	300	19:48	2006	245	05:10
2007	364	19:46	2007	200	05:09
2008	015	19:46	2007	248	05:09
2008	040	08:35	2007	264	05:09
2008	159	08:37	2007	280	05:09

2008	207	08:38	2008	194	05:09
2008	303	08:40	2008	209	16:54
2009	001	08:40	2008	210	05:09
2009	008	19:50	2009	163	16:57
2009	033	08:41	2009	164	05:12
2009	040	19:51	2009	195	16:57
2009	049	08:42	2009	196	05:12
2010	212	08:38			
2011	007	08:37			
2011	199	08:37			
2011	263	08:36			
2011	327	08:37			
2011	359	08:37			
2012	017	19:46			
2012	065	19:47			
2012	074	08:37			
2012	138	08:37			
2012	170	08:37			
2012	177	19:47			
2012	186	08:37			
2012	202	08:37			
2012	289	19:46			
2013	019	19:47			
2013	028	08:37			

REFERENCES

Ackerman, T.P., K. Liou, F.P. Valero, and L. Pfister (1988), Heating Rates in Tropical Anvils, *J. Atmos. Sci.*, **45**, 1606–1623, https://doi.org/10.1175/1520-0469(1988)045<1606:HRITA>2.0.CO;2.

Ackerman, S.A., R.E. Holz, R. Frey, E.W. Eloranta, B.C. Maddux, and M. McGill (2008), Cloud Detection with MODIS. Part II: Validation. *J. Atmos. Oceanic Technol.*, **25**,1073–1086, https://doi.org/10.1175/2007JTECHA1053.1.

Adler, R.F., et al. (2003), The Version 2 Global Precipitation Climatology Project (GPCP) Monthly Precipitation Analysis (1979 - Present), *J. Hydrometeor*., **4**(6), 1147-1167.

AghaKouchak A., N. Nasrollahi, and E. Habib (2009), Accounting for uncertainties of the TRMM satellite estimates, *Remote Sens*., **1**, 606–619, doi:10.3390/rs1030606.

Alexandrov, M., B. Cairns, B.E. Carlson, and A.A. Lacis (2005), Fine and coarse mode aerosols in Southern Great Plains multi-filter rotating shadowband radiometer datasets Fifteenth ARM Science Team Meeting Proceedings, Daytona Beach, Fla., March 14–18.

Arakawa A., and W.H. Schubert (1974), Interaction of a cumulus cloud ensemble with the large-scale environment, Part I, *J. Atmos. Sci*., **31**:674–701.

Austin, R.T. and G.L. Stephens (2001), Retrieval of stratus cloud microphysical parameters using millimeter-wave radar and visible optical depth in preparation for CloudSat, *J. of Geophys. Res*., **106**, D22, 28233-28242.

Austin, R.T., A.J. Heymsfield, and G.L. Stephens (2009), Retrieval of ice cloud microphysical parameters using the CloudSat millimeter-wave radar and temperature, *J. Geophys. Res.*, **114**, D00A23, doi:10.1029/2008JD010049.

Bacmeister, J.T., M.J. Suarez, and F.R. Robertson (2006), Rain re-evaporation boundary layer–convection interactions and Pacific rainfall patterns in an AGCM, *J. Atmos. Sci*., **63**, 3383–3403.

Barker, H.W., G.L. Stephens, and Q. Fu (1999), The sensitivity of domain-averaged solar fluxes to assumptions about cloud geometry, *Q. J. R. Meteorol. Soc.*, **125**, 2127-2152.

Barkstrom, B.R, E.F. Harrison, G.L. Smith, and R.D. Cess (1989), Results from the Earth Radiation Budget Experiment (ERBE), *Adv. in Space Res*., **9**(7), 75-82.

Berry, E., and G.G. Mace (2014), Cloud properties and radiative effects of the Asian summer monsoon derived from A-Train data, *J. Geophys. Res. Atmos*., **119**, doi:10.1002/2014JD021458.

Bloom, S., L. Takacs, A. DaSilva, and D. Ledvina (1996), Data assimilation using incremental analysis updates, *Mon. Weather Rev*., **124**, 1256–1271.

Bloom, S., et al. (2005), Documentation and validation of the Goddard Earth Observing System (GEOS) data assimilation system–version 4, NASA Technical Report Series on Global Modeling and Data Assimilation, NASA/TM-2005-104606, vol. 26, 165 pp. [Available at http://ntrs. nasa.gov/archive/nasa/casi.ntrs.nasa.gov/20050175690_2005173043.pdf.]

Bosilovich, M., et al. (2015), MERRA-2: Initial evaluation of the climate Technical Report Series on Global Modeling and Data Assimilation, NASA/TM–2015-104606, **43**.

Campbell, J.R., K. Sassen, and E.J. Welton (2008), Elevated cloud and aerosol layer retrievals from micropulse lidar signal profiles, *J. Atmos. Oceanic Technol.*, **25**, 685–700, doi:https://doi.org/10.1175/2007JTECHA1034.1.

Campbell, J.R., M.A. Vaughan, M. Oo, R.E. Holz, J.R. Lewis, and E.J. Welton (2015), Distinguishing cirrus cloud presence in autonomous lidar measurements, *Atmos. Meas. Tech.*, **8**, 435-449, doi:10.5194/amt-8-435-2015.

Campbell, J.R., S. Lolli, J.R. Lewis, Y. Gu, and E.J. Welton (2016), Daytime Cirrus Cloud Top-of-the-Atmosphere Radiative Forcing Properties at a Midlatitude Site and Their Global Consequences. *J. Appl. Meteor. Climatol.*, **55**, 1667–1679, https://doi.org/10.1175/JAMC-D-15-0217.1.

Ceppi, P., F. Brient, M.D. Zelinka, and D.L. Hartmann (2017), Cloud feedback mechanisms and their representation is global climate models, *Wiley Interdiscip. Rev.: Climate Change*, 8, e465, https://doinorg/10.1002/wvv.465.

CERES EBAF_Ed2.8 data quality summary, http://ceres.larc.nasa.gov/ products.php?product=EBAF-TOA.

Cesana, G., D.E. Waliser, T. L'Ecuyer, X. Jiang, and J-L. F. Li (2017), Evaluation of radiative heating rate profiles in eight GCMs using A-train satellite observations, *PAIP Conf. Proc.*, **1810**, 070001, doi:10.1063/1.4975522.

Charlock, T.P., and T.L. Alberta (1996), The CERES/ARM/GEWEX Experiment (CAGEX) for the retrieval of radiative fluxes with satellite data, *Bull. Am. Meteorol. Soc*., **77**(11), 2673–2683.

Chen, X., X. Huang, X. Dong, B. Xi, E.K. Dolinar, N.G. Loeb, S. Kato, P. Stackhouse, and M.G. Bosilovish (2018), Using AIRS and ARM SGP clear-sky observations to evaluate meteorological reanalyses: a hyperspectral radiance closure approach, *Submitted to J. Geophys. Res.*

Chiriaco, M., et al. (2007), Comparison of CALIPSO-like, LaRC, and MODIS retrievals of ice- cloud properties over SIRTA in France and Florida during CRYSTAL-FACE, *J. Appl. Meteo. Clim*., **46**, 249–272. doi:10.1175/JAM2435.1.

Chou, M.D., and M.J Suarez (1999), A solar radiation parameterization for atmospheric studies, NASA technical report series on global modeling and data assimilation, NASA/TM-1999-104606, **15**, 40 pp.

Chou, M.D., M.J. Suarez, X.Z. Liang, and M.M.-H. Yan (2001), A thermal infrared radiation parameterization for atmospheric studies, NASA technical report series on global modeling and data assimilation, NASA/TM-2001-104606, **19**, 56 pp.

Clothiaux, E.E., T.P. Ackerman, G.G. Mace, K.P. Moran, R.T. Marchand, M.A. Miller, and B.E. Martner (2000), Objective determination of cloud heights and radar reflectivities using a combination of active remote sensors at the Atmospheric Radiation Measurement Program Cloud and Radiation Test Bed (ARM CART) sites, *J. Appl. Meteorol*., **39**, 645–665.

Coakley, J.A., R.D. Cess, and F.B. Yurevich (1983), The effect of tropospheric aerosols on the earth's radiation budget: a parameterization for climate models, *J. Atmos. Sci*., **40**, 116–138.

Collins, W.D, et al. (2001), Parameterization of generalized cloud overlap for radiative calculations in general circulation models, *J. Clim*., **58**, 3224–3242.

Compo, G.P., et al. (2011), The twentieth century reanalysis project, Q. J. R. Meteorol. Soc., **137**, 1–28, doi:10.1002/qj.776.

Comstock, J.M., T.P. Ackerman, and G.G. Mace (2002), Ground-based lidar and radar remote sensing of tropical cirrus clouds and Nauru Island: Cloud statistics and radiative impacts, *J. Geosphys. Res. Atmos*., **107**, doi:10.1029/2002JD002203.

Cziczo, D.J., K.D. Froyd, C. Hoose, E.J. Jensen, M. Diao, M.A. Zondlo, J.B. Smith, C.H. Twohy, and D.M. Murphy (2013), Clarifying the dominant sources and mechanisms of cirrus cloud formation, *Science*, **340**, 1320–1324, doi:10.1126/science.1234145.

Dee, D.P., et al. (2011), The ERA-Interim reanalysis: configuration and performance of the data assimilation system, *Q. J. R. Meteorol. Soc.*, **137**, 553–597, doi:10.1002/qj.828.

Del Genio, A.D., J. Wu, and Y. Chen (2012), Characteristics of Mesoscale Organization in WRF simulations of convection during TWP-ICE, *J. Clim.,* **25**, 5666-5688, doi: 10.1175/JCLI-D-11-00422.1.

Deng M., G.G. Mace, Z. Wang, and H. Okamoto (2010), Tropical Composition, Cloud and Climate Coupling Experiment validation for cirrus cloud profiling retrieval using CloudSat radar and CALIPSO lidar, *J. Geophys. Res*., **115**, D00J15, doi:10.1029/2009JD013104.

Deng M., G.G. Mace, Z. Wang, and R.P. Lawson (2013), Evaluation of several A-Train ice cloud retrieval products with in situ measurements collected during the SPARTICUS campaign, *J. Appl. Meteorol. Climatol*., **52**, 1014–1030.

Deng, M., G.G. Mace, Z. Wang, and E. Berry (2015), CloudSat 2C-ICE product update with a new Ze parameterization in lidar-only region, *J. Geophys. Res. Atmos.*, **120**, 198–12,208, doi:10.1002/2015JD023600.

Divakarla, M., et al. (2008), Evaluation of Atmospheric Infrared Sounder ozone profiles and total ozone retrievals with matched ozonesonde measurements, ECMWF ozone data, and Ozone Monitoring Instrument retrievals, *J. Geophys. Res*., **113**, D15308, doi:10.1029/2007JD009317.

Doelling, D.R., N.G. Loeb, D.F. Keyes, M.L. Nordeen, D. Morstad, C. Nguyen, B.A. Wielicki, D.F. Young, and M. Sun (2013), Geostationary enhanced temporal interpolation for CERES flux products, *J. Atmos. Ocean Technol.,* **30**, 1072–1090.

Dolinar E.K., X. Dong, B. Xi, J.H. Jiang, and H. Su (2015), Evaluation of CMIP5 simulated clouds and TOA radiation budgets using NASA satellite observations, *Clim. Dyn*., **4**, 2229-2247, doi:10/1007/s00382-014-2158-9.

Dolinar E.K., X. Dong, and B. Xi (2016a), Evaluation and Intercomparison of Clouds, Precipitation, and Radiation Budgets in Recent Reanalyses using Satellite-Surface Observations, *Clim. Dyn.*, doi: 10.1007/s00382-015-2693-z.

Dolinar, E.K., X. Dong, B. Xi, J.H. Jiang, and N.G. Loeb (2016b), A clear-sky radiation closure study using a one-dimensional radiative transfer model and collocated satellite-surface-reanalysis data sets, *J. Geophys. Res. Atmos.*, **121**, 13, 698–13,714, doi:10.1002/2016JD025823.

Dolinar, E.K., X. Dong, B. Xi, J.H. Jiang, N.G. Loeb, J.R. Campbell, and H. Su (2018), A global record of single-layer ice cloud properties and associated radiative heating rate profiles from an A-Train perspective, *submitted to Clim. Dyn.*

Dong, X., B. Xi, and P. Minnis (2006), A climatology of midlatitude continental clouds from the ARM SGP central facility. Part II: Cloud Fraction and surface radiative forcing, *J. Clim.*, **19**, 1765–1783.

Dong, X., P. Minnis, B. Xi, S. Sun-Mack, and Y. Chen (2008a), Comparison of CERES-MODIS stratus cloud properties with ground-based measurements at the DOE ARM Southern Great Plains site, *J. Geophys. Res.*, **113**, D03204, doi:10.1029/2007JD008438.

Dong, X., B.A. Wielicki, B. Xi, Y. Hu, G.G. Mace, S. Benson, F. Rose, S. Kato, T. Charlock, and P. Minnis (2008b), Using observations of deep convective systems to constrain atmospheric column absorption of solar radiation in the optically thick limit, *J. Geophys. Res.*, **113**, D10206, doi:10.1029/2007JD009769.

Dong, X., B. Xi, K. Crosby, C.N. Long, R.S. Stone, and M.D. Shupe (2010), A 10-year climatology of Arctic cloud fraction and radiative forcing at Barrow, Alaska, *J. Geophys. Res.*, **115**, D17212, doi:10.1029/2009JD013489.

Dong, X., B. Xi, A.D. Kennedy, P. Minnis, and R. Wood (2014), A 19-month record of marine aerosol–cloud–radiation properties derived from DOE arm mobile facility deployment at the Azores. Part I: cloud fraction and single-layered MBL cloud properties, *J. Clim.*, **27**, 3665–3682. doi:10.1175/JCLI-D-13-00553.1.

Dong, X., B. Xi, S. Qiu, P. Minnis, S. Sun-Mack, and F. Rose (2016), A radiation closure study of Arctic cloud microphysical properties using the collocated satellite-surface data and Fu-Liou radiative transfer model, *J. Geophys. Res. Atmos.*, **121**, 10175–10198, doi:10.1002/2016JD025255.

Eliasson, S., S.A. Buehler, M. Milz, P. Eriksson, and V.O. John (2011), Assessing observed and modelled spatial distributions of ice water path using satellite data, *Atmos. Chem. Phys*., **11**, 375–391, doi:10.5194/acp-11-375-2011.

Elsaesser, G.S., A.D. Del Genio, J.H. Jiang, and M. van Lier-Walqui (2017), An improved convective ice parameterization for the NASA GISS Global Climate Model and impacts on cloud ice simulation. *J. Clim.*, **30**, no. 1, 317-336, doi:10.1175/JCLI-D-16-0346.1.

Froidevaux, L., et al. (2008), Validation of Aura Microwave Limb Sounder stratospheric ozone measurements, *J. Geophys. Res*., **113**, D15S20, doi:10.1029/2007JD008771.

Fu, Q., and K.N. Liou (1993), Parameterization or the radiative properties of cirrus clouds, *J. of the Atmos. Sci*., **50**, 2008-2025.

Fu, Q., K. Liou, M. Cribb, T. Charlock, and A. Grossman (1997), On multiple scattering in thermal infrared radiative transfer, *J. Atmos. Sci.*, **54**, 2799–2812, doi:10.1175/1520-0469(1997)054<2799:MSPITI>2.0.CO;2.

Geier, E.B., R.N. Green, D.P. Kratz, P. Minnis, W.F. Miller, S.K. Nolan, and C.B. Franklin (2001), Single Satellite Footprint TOA/Surface Fluxes and Clouds (SSF) Collection Document, NASA Langley Res. Cent., Hampton, VA [Available at http://asd-www.larc.nasa.gov/ceres/collect_guide/SSF_CG.pdf.]

Habib E., and W.F. Krajewski (2002), Uncertainty of the TRMM ground-validation radar-rainfall products: application of the TEFLUN-B field campaign, *J. Appl. Meteorol*., **41**, 558–572.

Hartmann, D.L., B-M. E. Ockert, and M.L. Michelsen (1992), The effect of cloud type on earth's energy balance: Global analysis, *J. Climate*, **5,** 1281–1304.

Haynes, J.M., T.S., L'Ecuyer, G.L. Stephens, S.D. Miller, C. Mitrescu, N.B. Wood, and S. Tanelli (2009), Rainfall retrieval over the ocean with spaceborne W-band radar, *J. Geophys. Res*., **114**, D00A22, doi:10.1029/2008JD009973.

Henderson, D.S., T. L'Ecuyer, G. Stephens, P. Partain, and M. Sekiguchi (2013), A multi-sensor perspective on the radiative impacts of clouds and aerosols, *J. Appl. Meteo. And Clim.*, **52**, 853-871, doi: 10.1175/JAMC-D-12-025.1.

Hogan, R.J and A.J. Illingworth (2000), Deriving cloud overlap statistics from radar, *Q. J. R. Meteorol. Soc.*, **126**, 2903-2909.

Holz, R. E., and Coauthors (2016), Resolving ice cloud optical thickness biases between CALIOP and MODIS using infrared retrievals. *Atmos. Chem. Phys.*, **16**, 5075–5090, doi:https://doi.org/10.5194/acp-16-5075-2016.

Hou, Y., S. Moorthi, and K. Compana (2002), Parameterization of solar radiation transfer in NCEP models, Office note 441, NCEP, Washington, DC.

Huffman, G.J. (1997), Estimates of root mean-square random error for finite samples of estimated precipitation, *J. Appl. Meteorol*., **36**, 1191–1201.

Huffman G.J., D. Bolvin, E.J. Nelkin, D.B. Wolff, R.F. Adler, G. Gu, Y. Hong, K.P. Bowman, and E.F. Stocker (2007), The TRMM multi-satellite precipitation analysis (TMPA): quasi-global, multiyear, combined-sensor precipitation estimates at fine scales. *J. Hydrometeo*., **8**, 38–55. doi:10.1175/JHM560.1.

Hwang, Y.-. T., D.M.W. Frierson, and J.E. Kay (2011), Coupling between Arctic feedbacks and changes in poleward energy transport, *Geophys. Res. Lett*., **38**, L17704, doi:10.1029/2011GL048546.

IPCC AR5 (2013) Chapter 9: evaluation of Climate Models. http://.climatechange2013.org/images/report/WG1AR5_Chapter09_FINAL.pdf

Jakob, C. (1998), Cloud cover in the ECMWF reanalysis, *J. Clim*., **12**, 947–959.

Jiang, J.H., et al. (2010), Five-year (2004-2009) observations of upper tropospheric water vapor and cloud ice from MLS and comparisons with GEOS-5 analyses, *J. Geophys. Res*. **115**, D15103, doi:10.1029/2009JD013256.

Jiang, J.H., et al. (2012), Evaluation of cloud and water vapor simulations in CMIP5 climate models using NASA 'A-Train' satellite observations, *J. Geophys. Res*., **117**, D14105, doi:10.1029/2011JD017237.

Jiang, J.H., H. Su, C. Zhai, L. Wu, K. Minschwaner, A.M. Molod, and A.M. Tompkins (2015), An assessment of upper-troposphere and lower stratosphere water vapor in MERRA, MERRA2 and ECMWF reanalyses using Aura MLS observations, *J. Geophys. Res. Atmos*., **120**, 11468–11485, doi:10.1002/2015JD023752.

Jiang, J.H., et al. (2017), A Simulation of Ice Cloud Particle Size, Humidity and Temperature Measurements from the TWICE CubeSat, *Earth and Space Science*.

Joseph, J.H., W.J. Wiscombe, and J.A Weinman (1976), The delta-Eddington approximation for radiative flux transfer, *J. Atmos. Sci*., **33**, 2452–2459.

Kato, S., T.P. Ackerman, J.H. Mather, and E.E. Clothiaux (1999), The k-distribution method and correlated-k approximation for a shortwave radiative transfer model, *J. Quant. Spectrosc. Radiat. Transf.*, **62**, 109–121, doi:10.1016/S0022-4073(98)00075-2.

Kato, S., F.G. Rose, and T.P. Charlock (2005), Computation of domain averaged irradiance using satellite-derived cloud properties, *J. Atmos. Oceanic Technol*., **22**, 146–164.

Kato, S., S. Sun-Mack, W.F. Miller, F.G. Rose, Y. Chen, P. Minnis, and B.A. Wielicki (2010), Relationships among cloud occurrence frequency, overlap, and effective thickness derived from CALIPSO and CloudSat merged cloud vertical profiles, *J. Geophys. Res.*, **115**, D00H28, doi:10.1029/2009JD012277.

Kato, S., et al. (2011), Improvements of top-of-atmosphere and surface irradiance computations with CALIPSO-, CloudSat-, and MODIS-derived cloud and aerosol properties, *J. Geophys. Res*., **116**, D19209, doi:10.1029/2011JD016050.

Kato, S., N.G. Loeb, F.G. Rose, D.R. Doelling, D.A. Rutan, T.E. Caldwell, L. Yu, and R.A. Weller (2013), Surface irradiances consistent with CERES-derived top-of-atmosphere shortwave and longwave irradiances, *J. Clim*., **26**, 2719–2740. doi:10.1175/JCLI-D-12-00436.1.

Kato, S. N.G. Loeb, D.A. Rutan, and F.G. Rose (2015), Clouds and the Earth's Radiant Energy System (CERES) Data products for climate research, *J. of the Meteo. Soc. of Japan*, **93,** 597-612, doi: 10.2151/jmsj.2015-048.

Kawai, H., and T. Inoue (2006), A simple parameterization scheme for subtropical marine stratocumulus, *SOLA*, **2**, 17–20.

Kay, J.E., B.R. Hillman, S.A. Klein, Y. Zhang, B. Medeiros, R. Pincus, A. Gettelman, B. Eaton, J. Boyle, R. Marchand, and T.P. Ackerman (2012), Exposing Global Cloud Biases in the Community Atmosphere Model (CAM) Using Satellite Observations and Their Corresponding Instrument Simulators, *J. Climate*, **25**, 5190–5207, https://doi.org/10.1175/JCLI-D-11-00469.1.

Kennedy, A.D., X. Dong, B. Xi, P. Minnis, A. Del Genio, M.M. Khaiyer, and A. Wolf (2010), Evaluation of NASA GISS Single Column Model Simulated Clouds Using Combined Surface and Satellite Observation, *J. Clim*., doi:10.1175/2010JCLI3353.1.

Kennedy, A.D., X. Dong, B. Xi, S. Xie, Y. Zhang, and J. Chen (2011), A comparison of MERRA and NARR reanalysis datasets with the DOE ARM SGP continuous forcing data, *J. Clim.*, **24**, 4541–4557.

King, A., and A.D. Kennedy (2018), Severe weather environments in atmospheric reanalyses, *Accepted to J. of Appl. Meteor. and Clim.*

Köhler, M., M. Ahlgrimm, and A.C.M Beljaars (2011), Unified treatment of dry convective and stratocumulus-topped boundary layers in the ECMWF model, *Q. J. R. Meteorol. Soc.*, **137**, 43–57.

Kox, S., L. Bugliaro, and A. Ostler (2014), Retrieval of cirrus cloud optical thickness and top altitude from geostationary remote sensing, *Atmos. Meas. Tech.*, **7**, 3233–3246, doi:10.5194/amt-7-3233-2014.

Larson, K., and D.L. Hartmann (2003), Interactions among Cloud, Water Vapor, Radiation, and Large-Scale Circulation in the Tropical Climate. Part I: Sensitivity to Uniform Sea Surface Temperature Changes, *J. of Clim.*, **16**, 1425-1440.

Lauer, A., and K. Hamilton (2012), Simulating clouds with global climate models: a comparison on CMIP5 results with CMIP3 and satellite data, *J. Clim.*, doi:10.1175/JCLI-D-12-0451.1.

L'Ecuyer, T.S., N.B. Wood, T. Haladay, G.L. Stephens, and P.W. Stackhouse Jr. (2008), Impact of clouds on atmospheric heating based on the R04 CloudSat fluxes and heating rates data set, *J. Geophys. Res.*, **113**, D00A15, doi:10.1029/2008JD009951.

L'Ecuyer, T.S., and J.H. Jiang (2010), Touring the atmosphere aboard the A-Train, *Physics Today*, **63**, 7, 36-41, doi:10.1063/1.3463626.

L'Ecuyer, T.S., et al. (2015), The observed state of the energy budget in the early twenty-first century, *J. of Clim.*, **28**, 8319-8346, doi:10.1175/JCLI-D-14-00556.1.

Li, Z., M.C. Cribb, and A.P. Trishchenko (2002), Impact of surface inhomogeneity on solar radiative transfer under overcast conditions, *J. Geophys. Res.*, **107**(D16), 4294, doi:10.1029/2001JD000976.

Li, J.-L. F., et al. (2012), An observationally based evaluation of cloud ice water in CMIP3 and CMIP5 GCMs and contemporary reanalyses using contemporary satellite data, *J. Geophys. Res.*, **117**, D16105, doi:10.1029/2012JD017640.

Liang, X.Z. and W.C. Wang (1997), Cloud overlap effects on general circulation model climate simulations, *J. Geophys. Res*., **102**, 11039-11047.

Lock, A.P., A.R. Brown, M.R. Bush, G.M. Martin, and R.N.B. Smith (2000), A new boundary layer mixing scheme. Part I: scheme description and single-column model tests, *Mon. Weather Rev*., **138**, 3187–3199.

Loeb, N.G., S. Kato, N. Manalo-Smith, S.K. Gupta, W.F. Miller, P. Minnis, and B.A. Wielicki (2003), Angular distribution models for top-of atmosphere radiative flux estimation from the Clouds and the Earth's Radiant Energy System instrument on the Tropical Rainfall Measuring Mission satellite. Part I: Methodology, *J. Appl. Meteorol*., **42**, 240–26.

Loeb, N.G., S. Kato, K. Loukachine, and N. Manalo-Smith (2005), Angular Distribution Models for Top-of-Atmosphere Radiative Flux Estimation from the Clouds and the Earth's Radiant Energy System Instrument on the Terra Satellite. Part I: Methodology, *J. Atmos. Oceanic Technol.*, **22**, 338–351, https://doi.org/10.1175/JTECH1712.1.

Loeb, N.G., W. Sun, W.F. Miller, K. Loukachine, and R. Davies (2006), Fusion of CERES, MISR, and MODIS measurements for top-of-atmosphere radiative flux validation, *J. Geophys. Res*., **11**, D18209, doi:10.1029/2006JD007146.

Loeb, N.G, B.A. Wielicki, F.G. Rose, and D.R. Doelling (2007), Variability in global top-of-atmosphere shortwave radiation between 2000 and 2005, *Geophys. Res. Lett.*, **34**, L03704, doi: .1029/2006GL028196.

Loeb, N.G., B.A. Wielicki, D.R. Doelling, G.L. Smith, D.F. Keyes, S. Kato, N. Manalo-Smith, T. Wong (2009), Toward optimal closure of the Earth's top-of-atmosphere radiation budget, *J. Clim.*, **22**, 748–766, doi:10.1175/2008JCLI2637.1.

Loeb, N.G., J.M. Lyman, G.C. Johnson, R.P. Allan, D.R. Doelling, T. Wong, B.J. Soden, and G.L Stephens (2012), Observed changes in top-of-the atmosphere radiation and upper-ocean heating consistent within uncertainty, *Nat. Geosci*., **5**, 110–113. doi:10.1038/NGEO1375.

Long, C.N., and Y. Shi (2008), An automated quality assessment and control algorithm for surface radiation measurements, *J. Open Atmos*. Sci., **2**, 23–37.

Long, C.N., and D.D. Turner (2008), A method for continuous estimation of clear-sky downwelling longwave radiative flux developed using ARM surface measurements, *J. Geophys. Res*., **113**, D18206, doi:10.1029/2008JD009936.

Louis, J., M. Tiedtke, J. and Geleyn (1982), A short history of the PBL parameterization at ECMWF, In: Proceedings ECMWF workshop on planetary boundary layer parameterization, Reading, United Kingdom, ECMWF, 59–80.

Mace, G.G., et al. (2005), Evaluation of cirrus cloud properties derived from MODIS data using cloud properties derived from ground-based observations collected at the ARM SGP site, *J. Appl. Meteorol*., **44**, 221–240.

Mace, G.G., Q. Zhang, M. Vaughan, R. Marchand, G. Stephens, C. Trepte, and D. Winker (2009), A description of hydrometeor layer occurrence statistics derived from the first year of merged Cloudsat and CALIPSO data, *J. Geophys. Res*., **114**, D00A26, doi:10.1029/2007JD009755.

Marquis, J.W., A.S. Bogdanoff, J.R. Campbell, J.A. Cummings, D.L. Westphal, N.J. Smith, and J. Zhang (2017), Estimating Infrared Radiometric Satellite Sea Surface Temperature Retrieval Cold Biases in the Tropics due to Unscreened Optically Thin Cirrus Clouds, *J. Atmos. Oceanic Technol.*, **34**, 355–373, https://doi.org/10.1175/JTECH-D-15-0226.1.

Mather, J.H., S.A. McFarlane, M.A. Miller, and K.L. Johnson (2007), Cloud properties and associated radiative heating rates in the tropical western Pacific, *J. Geophys. Res. Atmos*., **12**, doi:10.1029/2006JD007555.

McFarlane, S.A., J.H. Mather, and E.J. Mlawer (2016), ARM's Progress on Improving Atmospheric Broadband Radiative Fluxes and Heating Rates, *Meteorological Monographs*, **57**, 20.1–20.24, https://doi.org/10.1175/AMSMONOGRAPHS-D-15-0046.1.

McFarquhar, G.M., A.J. Heymsfield, J. Spinhirne, and B. Hart (2000), Thin and subvisual tropopause tropical cirrus: Observations and radiative impacts, *J. Atmos. Sci.*, **57**, 1841–1853.

Minnis, P., D.F. Young, B.A. Wielicki, P.W. Heck, X. Dong, L.L. Stowe, and R.M. Welch (1999), CERES cloud properties derived from multispectral VIRS data. In: Proceedings of SPIE 3867, satellite remote sensing of clouds and the atmosphere IV, 91, December 8, 1999. doi:10.1117/12.373047.

Minnis, P., D.F. Young, B.A. Wielicki, S. Sun-Mack, Q.Z. Trepte, Y. Chen, P.W. Heck, and X. Dong (2002), A global cloud database from VIRS and MODIS for CERES. In: Proceedings of SPIE 4891, optical remote sensing of the atmosphere and clouds III 115, April 9, 2003. doi:10.1117/12.467317.

Minnis, P., C.R. Yost, S. Sun-Mack, and Y. Chen (2008), Estimating the top altitude of optically thick ice clouds from thermal infrared satellite observations using CALIPSO data, *Geophys. Res. Lett*., **35**, L12801, doi:10.1029/2008GL033947.

Minnis, P., et al. (2011), CERES Edition-2 cloud property retrievals using TRMM VIRS and Terra and Aqua MODIS data. Part II: examples of average results and comparisons with other data, *IEEE Trans. Geosci. Remote Sens*., **49**, 4401–4430.

Mlawer, E.J., S.J. Taubman, P.D. Brown, M.J. Iacono, and S.A. Clough (1997), Radiative transfer for inhomogeneous atmospheres: RRTM, a validated correlated-k model for the longwave, *J. Geophys. Res.,* **102D**, 16663–16682.

Molod, A., L. Takacs, M. Suarez, and J. Bacmeister (2015), Development of the GEOS-5 atmospheric general circulation model: Evolution from MERRA to MERRA2, *Geosci. Model Dev*., **8**, 1339–1356, doi:10.5194/gmd-8-1339-2015.

Moorthi, S., H.-L. Pan, and P. Caplan (2001), Changes to the 2001 NCEP operational MRF/AVN global analysis/forecast system, *NWS Tech. Procedures Bulletin*, **484**, 14 pp http://www.nws.noaa.gov/om/tpb/484.htm.

Moorthi, S., and M.J. Suarez (1992), Relaxed Arakawa-Schubert: a parameterization of moist convection for general circulation models, Mon. Weather Rev., 120, 978–1002.

Moran, K.P., B.E. Martner, M.J. Post, R.A. Kropfli, D.C. Welsh, and K.B. Widener (1998), An unattended cloud-profiling radar for use in climate research, *Bull. Am. Meteorol. Soc*., **79**, 443–455.

Morcrette, J.J., and C. Jakob (2000), The response of the ECMWF model to changes in the cloud overlap assumption, *Mon. Weather Rev*., **128**,1707–1732.

Morris, V.R. (2006), Infrared thermometer (IRT) handbook DOE/SC-ARM TR-015.

Moy, L.A., R.O. Knuteson, D.C. Tobin, H.E. Revercomb, L.A. Borg, and J. Susskind (2010), Comparison of measured and modeled outgoing longwave radiation for

clear-sky ocean and land scenes using coincident CERES and AIRS observations, *J. Geophys. Res*., **115**, D15110, doi:10.1029/2009JD012758.

Nazaryan, H., M.P. McCormick, and W.P. Menzel (2008), Global characterization of cirrus clouds using CALIPSO data, *J. Geophys. Res*., **113**, D16211, doi:10.1029/2007JD009481.

Onogi, K., J. Tsutsui, H. Koide, M. Sakamoto, S. Kobayashi, H. Hatsushika, T. Matsumoto, N. Yamazaki, H. Kamahori, K. Takahashi, S. Kadukora, K. Wada, K. Kato, R. Oyama, T. Ose, N. Mannoji, and R. Taira (2007), The JRA-25 Reanalysis, *J. Meteorol. Soc. Jap*., **85(**3), 369–432.

Painemal, D. and P. Zuidema (2011), Assessment of MODIS cloud effective radius and optical depth over the Southeast Pacific with VOCALS-REx in situ *measurements, J. Geophys. Res*., **116**, D24206, doi:10.1029/2011JD016155.

Pincus, R., C.P. Batstone, R.J.P. Hofmann, K.E. Taylor, and P.J. Glecker (2009), Evaluating the present-day simulation of clouds, precipitation, and radiation in climate models, *J. Geophys. Res*., **113**, D14209, doi:10.1029/2007JD009334.

Qin, Y., and R.M. Mitchell (2009), Characterisation of episodic aerosol types over the Australian continent, *Atmos. Chem. Phys*., **9**, 1943–1956.

Qiu, S., B. Xi, and X. Dong (2018), Influence of wind directions on thermodynamic properties and Arctic mixed-phase clouds at Barrow, Alaska, *Accepted to J. of Geophys. Res.*

Quinn, P.K., T.L. Miller, T.S. Bates, J.A. Ogren, E. Andrews, and G.E. Shaw (2002), A 3-year record of simultaneously measured aerosol chemical and optical properties at Barrow, Alaska, *J. Geophys. Res*., **107**(D11), 4130, doi:10.1029/2001JD001248.

Ramanathan, V., R.D Cess, E.F. Harrison, P. Minnis, B.R. Barkstrom, E. Ahmad, and D. Hartmann (1989), Cloud-radiative forcing and climate: results from the earth radiation budget experiment, *Science*, **243**, 57–63.

Randall, D., and D.-M. Pan (1993), Implementation of the Arakawa-Schubert cumulus parameterization with prognostic closure. Meteorological monograph/the representation of cumulus convection in numerical models, *J. Amos. Sci*., **46**, 137–144.

Randall, D.A., R.A. Wood, S. Bony, R. Colman, T. Fichefet, J. Fyfe, V. Kattsov, A. Pitman, J. Shukla, J. Srinivasan, R.J. Stouffer, A. Sumi and K.E. Taylor (2007), Climate Models and Their Evaluation. In: Climate Change (2007), The Physical Science Basis. Contribution of Working Group I to the Fourth Assessment Report of the Intergovernmental Panel on Climate Change [Solomon, S., D. Qin, M. Manning, Z. Chen, M. Marquis, K.B. Averyt, M.Tignor and H.L. Miller (eds.)]. Cambridge University Press, Cambridge, United Kingdom and New York, NY, USA.

Read, W.G., et al. (2007), Aura Microwave Limb Sounder upper tropospheric and lower stratospheric H_2O and RH_i validation, *J. Geophys. Res*., doi:10.1029/2007JD008752.

Reichle, R. H., and Q. Liu (2014), Observation-corrected precipitation estimates in GEOS-5, NASA/TM–2014-104606, vol. 35. [Available at http://gmao.gsfc.nasa.gov/pubs/tm/docs/Reichle734.pdf.]

Rienecker, M.M., et al. (2011), MERRA: NASA's modern-era retrospective analysis for research and applications. J Clim 24:3624–3648, doi:10.1175/JCLI-D-11-00015.1.

Rossow, W.B., and R.A. Schiffer (1999), Advances in Understanding Clouds from ISCCP, *Bull. Amer. Meteor. Soc.*, **80**, 2261–2288, https://doi.org/10.1175/1520-0477(1999)080<2261:AIUCFI>2.0.CO;2.

Ruzmaikin, A., H.H. Aumann, and J.H. Jiang (2015), Interhemispheric variability of the Earth's radiation, *J. Atmos. Sci.*, **72**(12), 4615–4628, doi:10.1175/JAS-D-15-0106.1.

Saha, S., S. Nadiga, C. Thiaw, J. Wang, W. Wang, Q. Zhang, H.M. Van den Dool, H.-L. Pan, S. Moorthi, D. Behringer, S. Stokes, M. Peña, S. Lord, G. White, W. Ebisuzaki, P. Peng, and P. Xie (2006), The NCEP climate forecast system, *J. Clim.*, **19**, 3483–3517, doi:10.1175/JCLI3812.1.

Sassen, K., and B.S. Cho (1992), Subvisual-Thin Cirrus Lidar Dataset for Satellite Verification and Climatological Research, *J. of Appl. Meteo*., **31**, 1275-1285.

Sassen, K., Z. Wang, and D. Liu (2008), Global distribution of cirrus clouds from CloudSat/Cloud-Aerosol lidar and infrared pathfinder satellite observations (CALIPSO) measurements, *J. Geophys. Res.*, **113**, D00A12, doi: 10.1029/2008JD009972.

Schwartz, M.J., et al. (2008), Validation of the Aura Microwave Limb Sounder temperature and geopotential height measurements, *J. Geophys. Res*., **113**, D15S11, doi:10.1029/2007JD008783.

Stackhouse, P.W., Jr., S.K. Gupta, S.J. Cox, T. Zhang, J. C. Mikovitz, and L.M. Hinkelman (2011), The NASA/GEWEX surface radiation budget release 3.0: 24.5-year dataset, *GEWEX News*, **21**(1), 10–12.

Stanfield, R., X. Dong, B. Xi, A.D. Kennedy, A.D. Del Genio, P. Minnis, and J.H. Jiang (2014), Assessment of NASA GISS CMIP5 and post-CMIP5 simulated clouds and TOA radiation budgets using satellite observations: part I: cloud fraction and properties, *J. Clim*., doi:10.1175/JCLI-D-13-00588.1.

Stanfield, R., J.H. Jiang, X. Dong, B. Xi, and H. Su (2016), A Quantitative Assessment of Precipitation Associated with the ITCZ in the CMIP5 GCM Simulations, *Clim. Dyn*., **47**, 1863-1880, doi:10.1007/s00382-015-2937-y.

Stephens, G.L., and P.J. Webster (1981), Clouds and climate: Sensitivity of simple systems, *J. Atmos. Sci*., **38**, 235–247, doi:10.1175/1520-0469(1981)038,0235:CACSOS.2.0.CO;2.

Stephens, G.L., et al. (2002), The CloudSat mission and the A-Train: A New Dimension of Space-Based Observations of Clouds and Precipitation, *Bull. of the Amer. Meteo. Soc*., **83**, doi:10.1175/BAMS-83-12-1771.

Stubenrauch, C.J., et al. (2013), Assessment of global cloud datasets from satellites. *Bull. Amer. Meteor. Soc*., **94**, 1031–1049, doi:10.1175/BAMS-D-12-00117.1.

Su, H., J.H. Jiang, G.L. Stephens, D.G. Vane, and N.J. Livesey (2009), Radiative effects of upper tropospheric clouds observed by Aura MLS and CloudSat, *Geophys. Res. Lett.*, **36**, L09815, doi:10.1029/2009GL037173.

Su, W., J. Corbett, Z. Eitzen, and L. Liang (2015a), Next-generation angular distribution models for top-of-atmosphere radiative flux calculation from CERES instruments: Methodology, *Atmos. Meas. Tech*., **8**(2), 611–632, doi:10.5194/amt-8-611-2015.

Su, W., J. Corbett, Z. Eitzen, and L. Liang (2015b), Next-generation angular distribution models for top-of-atmosphere radiative flux calculation from CERES instruments: Validation, *Atmos. Meas. Tech.,* **8**(8), 3297–3313, doi:10.5194/amt-8-3297-2015.

Sugi, M., K. Kuma, K. Tada, K. Tamiya, N. Hasegawa, T. Iwasaki, S. Yamada, and T. Kitade (1990), Description and performance of the JMA operational global spectral model (JMA GSM88), *Geophys. Mag*., **43**, 105–130.

Sundqvist, H., E. Berge, and J.E. Kristjansson (1989), Condensation and cloud studies with a mesoscale numerical weather prediction model, *Mon. Weather Rev*., **117**, 1641–1657.

Susskind, J., G. Molnar, L. Iredell, and N.G. Loeb (2012), Interannual variability of outgoing longwave radiation as observed by AIRS and CERES, *J. Geophys. Res*., **117**, D23107, doi:10.1029/2012JD017997.

Takacs, L.L., M.J. Suárez, and R. Todling (2016), Maintaining atmospheric mass and water balance in reanalyses, *Q. J. R. Meteorol. Soc*., **142**, 1565–1573, doi:10.1002/qj.2763.

Taylor, K.E. (2001), Summarizing multiple aspects of model performance in a single diagram, *J. Geophys. Res*., **106**(D7), 7183–7192.

Taylor, K.E., R.J. Stouffer, and G.A. Meehl (2012), An Overview of CMIP5 and the Experiment Design, *Bull. Amer. Meteor. Soc*., **93**, 485–498.

Tegtmeier, S., et al. (2013), SPARC data initiative: A comparison of ozone climatologies from international satellite limb sounders, *J. Geophys. Res. Atmos*., **118**, 12229–12247, doi:10.1002/2013JD019877.

Tian, B., E. Manning, E. Fetzer, E. Olsen, and S. Wong (2014), AIRS version 6 L3 user guide AIRS/AMSU/HSB Version 6 Level 3 Product User Guide, Pasadena, Calif.

Troyan, D. (2012), Merged sounding value-added product technical report U.S. Department of Energy. DOE/SC-ARM-TR-087.

Virts, K.S., and J.M. Wallace (2010), Annual, interannual, and intraseasonal variability of tropical tropopause transition layer cirrus, *J. Atmos. Sci*., **67**, 3097–3112, doi:10.1175/2010JAS3413.1.

Wagner, T.M., and H.-F. Graf (2010), An ensemble cumulus convection parameterization with explicit cloud treatment, *J. Atmos. Sci*., **67**, 3854–3869, doi:10.1175/2010JAS3485.1.

Waters, J., et al. (2006), The Earth Observing System Microwave Limb Sounder (EOS MLS) on the Aura satellite, *IEEE Trans. Geosci. Remote Sens*., **44**(5), 1075–1092, doi:10.1109/TGRS.2006.873771.

Wang, H., and W. Su (2013), Evaluating and understanding top of the atmosphere cloud radiative effects in International Panel on Climate Change (IPCC) AR5 CMIP5 models using satellite observations, *J. Geophys. Res*., **118**, 683–699, doi:10.1029/2012JD018619.

Whitaker, J.S., and T.M. Hamill (2002), Ensemble data assimilation without perturbed observations, *Mon. Weather Rev*., **130**, 1913–1924.

Wielicki, B.A., B.R. Barkstrom, E.F. Harrison, R.B. Lee III, G.L. Smith, and J.E. Cooper (1996), Clouds and the Earth's Radiant Energy System (CERES): An Earth observing system experiment, *Bull. Am. Meteorol. Soc*., **77**, 853–868.

Wild, M., A. Ohmura, H. Gilgen, and D. Rosenfeld (2004), On the consistency of trends in radiation and temperature records and implications for the global hydrological cycle, *Geophys. Res. Lett*., **31**, L11201, doi:10.1029/ 2003GL019188.

Wild, M., C.N. Long, and A. Uhmura (2006), Evaluation of clear-sky solar fluxes in GCMs participating in AMIP and IPCC-AR4 from a surface perspective, *J. Geophys. Res*., **11**, D01104, doi:10.1029/2005JD006118.

Wild, M., D. Folini, M.Z. Hakuba, C. Schär, S. I. Seneviratne, S. Kato, D. Rutan, C. Ammann, E.F. Wood, and G. König-Langlo (2015), The energy balance over land and oceans: An assessment based on direct observations and CMIP5 climate models, *Clim. Dyn*., **44**(11-12), 3393–3429, doi:10.1007/s00382-014-2430-z.

Xi, B., X. Dong, P. Minnis, and M. Khaiyer (2010), A 10-yr climatology of cloud cover and vertical distribution from both surface and GOES observations over DOE ARM SGP site, *J. Geophys. Res*., **115**, D12124. doi:10.1029/2009JD012800.

Xi, B., X. Dong, P. Minnis, and S. Sun-Mack (2014), Validation of CERES-MODIS Edition 4 marine boundary layer cloud properties with using DOE ARM AMF measurements at the Azores, *J. Geophys. Res*., **119**, doi:10.1002/2014JD021813.

Xie, S., R.T. Cederwall, and M.H. Zhang (2004), Developing long-term single-column model/cloud system-resolving model forcing using numerical weather prediction products constrained by surface and top of the atmosphere observations, *J. Geophys. Res*., **109**, D01104, doi:10.1029/2003JD004045.

Yi, B., A.D. Rapp, P. Yang, B.A. Baum, and M.D. King (2017a), A comparison of Aqua MODIS ice and liquid water cloud physical and optical properties between

collection 6 and collection 5.1: Pixel-to-pixel comparisons, *J. Geophys. Res. Atmos*., **122**, doi:10.1002/2016JD025586.

Zhang, Y.-C., W.B. Rossow, A.A. Lacis, M.I. Mishchenko, and V. Oinas (2004), Calculation of radiative fluxes from the surface to top-of atmosphere based on ISCCP and other global datasets: Refinements of the radiative transfer model and the input data, *J. Geophys. Res*., **109**, D19105, doi:10.1029/2003JD004457.

Zhang H., J. Peng, X. Jing, and J.N. Li (2013), The features of cloud overlapping in Eastern Asia and their effect on cloud radiative forcing, *Sci. China Earth Sci*., **56**, 737-747.

Zelinka, M.D., C. Zhou, and S.A. Klein (2016), Insights from a refined decomposition of cloud feedbacks, *Geophys. Res. Lett*., **43**(17), doi:10.1002/2016GL069917.

Zhao, Q.Y., and F.H. Carr (1997), A prognostic cloud scheme for operational NWP models, *Mon. Weather Rev*., **125**, 1931–1953.

Zhou, C., M.D. Zelinka, and S.A. Klein (2017), Analyzing the dependence of global cloud feedback on the spatial pattern of sea surface temperature change with a Green's function approach, *J. Adv. Model. Earth Syst*., **9**, 2174–2189, doi:10.1002/ 2017MS001096.

Zib, B.J., X. Dong, B. Xi, and A. Kennedy (2012), Evaluation and intercomparison of cloud fraction and radiative fluxes in recent reanalyses over the Arctic using BSRN surface observations, *J. Clim*., **25**, 2291–2305, doi:10.1175/JCLI-D-11-00147.1.